PHYSIOLOGICAL TELEMETRIC SENSING SYSTEMS FOR MEDICAL APPLICATIONS

by

LUN-CHEN HSU

Presented to the Faculty of the Graduate School of

The University of Texas at Arlington in Partial Fulfillment

of the Requirements

for the Degree of

DOCTOR OF PHILOSOPHY

THE UNIVERSITY OF TEXAS AT ARLINGTON

December 2009

ACKNOWLEDGEMENTS

My deepest gratitude goes to my supervising professor Dr. J.-C. Chiao, who gave me opportunities to work on interdisciplinary research projects and always motivated me to explore my capabilities to do research. Without his support and guidance, I couldn't have completed my dissertation and couldn't have chance to get into MEMS and biomedical research fields.

I would like to thank Dr. Shou-Jiang Tang and Ms. Deborah Hogg for their help on the animal experiments. I also thank my dissertation committee: Dr. H.F. Tibbals, Dr. W. Alan Davis, Dr. Samir Iqbal and Dr. Weidong Zhou for their interest in my research and for taking time to serve in my dissertation committee.

I wish to thank all of my friends at UTA and colleagues in iMEMS group. Your friendship and support are my valuable assets. I would also like to thank the staff and researchers in UTA NanoFab, and Automation Robotic Research Institute (ARRI) for enriching my experience during my Ph.D. training. I would also like to express my sincere appreciation to Texas Instruments for financial support on the research project.

Finally, I would like to express my appreciation and thanks to my family for their unceasing support and encouragement throughout my career.

November 2, 2009

ABSTRACT

PHYSIOLOGICAL TELEMETRIC SENSING SYSTEMS FOR MEDICAL APPLICATION

Lun-Chen Hsu, PhD

The University of Texas at Arlington, 2009

Supervising Professor: Jung-Chih Chiao

A batteryless, wireless, sensing system, suitable for biomedical applications, was studied in this dissertation. The sensing system contains a reader and a transponder and the working principle is based on passive RFID systems. The transponder harvests the RF energy from the reader to power up the frequency generator circuit which is modulated by sensor signals. Sensor signals are encoded into frequency shifts to provide the immunity to motion artifacts and the robust performances of sensing system are demonstrated. The sensing platform can also be used for multiple sensor integration for different medical applications. In this dissertation, the physiological measurements are categorized into two groups - external and internal ones - depending on the deployment of the sensing devices. Two physiological sensing systems were studied to demonstrate the system architecture. An external application of pressure sensing for

pressure sore monitoring and an internal application for gastroesophageal reflux diagnosis were investigated.

For external physiological sensing application, a wireless batteryless piezoresistive pressure sensing system was presented for applications of monitoring pressure sore development in paralyzed patients who might be in beds or in wheelchairs. The transponder device included an energy harvesting circuit, a force sensing resistor, a resistance-to-frequency converter, and an antenna. The reader provided power to the device remotely and measures the sensor values in terms of frequency shift simultaneously. The experimental results showed good linearity, sensitivity, and resolution in the pressure range form 0 to 10 psi while the corresponding frequency shift detected by the reader was between 7.35 and 8.55 kHz depending on different testing scenarios. Stability tests of the sensor were carried out for long-term monitoring. The experimental results indicated that the drifting of reading was smaller than the readings of high-pressure indications so the sensors can be used for a long period of time. A pressure sensor array was arranged to detect pressure distribution in a certain area for sensing wound condition applications. The sensors were able to identify high pressure points dynamically.

For internal physiological sensing applications, an integration of impedance and pH sensors was presented for diagnosis of gastroesophageal reflux disease that affects approximately 15% of adult population in the United States. Our system included an implantable transponder that had impedance- and pH- sensing electrodes, and a wearable, external reader that wirelessly powered the transponder and recorded the

radio-frequency signals transmitted by the transponder. We tested our system by placing the sensor on the wall of the tube flushing with different liquids with known pH values, and by attaching the sensor to the esophagus wall of a live pig, after which those same liquids were flushed through the esophagus. In both cases, the external reader was positioned properly to record the impedance/pH data continuously from implanted capsule. The data were compared with those recorded discretely by an adjacently-placed Bravo capsule.

The experiment results showed that the impedance sensor picked up every simulated reflux episode and the pH sensor indicated the pH value of each episode. Our dual sensors responded to the stimulated reflux episodes immediately while Bravo pH sensor remained the same reading during the short simulated reflux episodes. Our impedance sensor was able to pick up the episodes with the pH value of 7 and the Bravo pH sensor failed to detect those events. The Bravo pH sensor malfunctioned when pH values were greater than 10, and our pH sensor still can detect those episodes. Our implantable, batteryless, wireless sensing system can detect acid and nonacid reflux episodes providing both impedance and pH information simultaneously for GERD monitoring. The *in vivo* statistical data of our dual sensors also showed good reliability and repeatability, with the standard deviation less than 0.16 kHz for impedance sensor, and the pH values of 0.33 for pH sensor in most of the cases.

In this dissertation, two medical sensing systems were designed, fabricated, and tested. The robustness of the sensing system were characterized and demonstrated with

both *in vitro* and *in vivo* experiments. The capability of the sensing platform to integrate with multiple sensors was also demonstrated.

TABLE OF CONTENTS

LIST OF ILLUSTRATIONS

LIST OF TABLES

CHAPTER 1

INTRODUCTION

1.1 Motivations and Objectives

Physiological signals contain vital information about the physiological activities in organs that can provide useful information for diagnosis and treatment in healthcare [1.1]. Therefore, using a scientific method to measure those physiological signals correctly and effectively is important. Sensing transducers can be used to detect those physiological signals and transduce into electrical signals for analysis [1.2-1.4]. However, the corresponding sensor interfacing circuits need to be designed properly so that the sensor signals can be processed correctly. A wireless transceiver offers a beneficial method to carry out the measured *in vivo* information by implanted transducers or the measured *in vitro* data by wearable transducers in many healthcare applications. Furthermore, for continuous healthcare monitoring and biomedical applications, a batteryless wireless sensing transceiver opens new opportunities for long-term physiological monitoring uses.

Sensor technology has been applied in various fields and played an important role to provide researchers meaningful measurement data [1.5, 1.6]. In physiological measurement applications, it provides us a scientific tool to characterize the physiological parameters to better understand the conditions of our bodies [1.1]. On the

other hand, Radio Frequency Identification (RFID) technology has brought great impacts to several different fields, including medical care applications [1.7-1.9]. It provides an effective and useful way to track and monitor various information with its identification ability and the data are transmitted wirelessly via radio frequency. While operated in its passive mode, the transponder can even work without a battery in it. Therefore, to integrate the sensor technology with the RFID technology for medical applications is the main interest of this study.

1.2 Enabling Technologies

1.2.1 Sensing Transducers

A sensing transducer is defined as a functional element that detects and converts one form of energy to another [1.2]. Transducers in a different way can be categorized into two broad classes depending on how they interact with the environment: passive and active transducers [1.3]. Passive transducers do not need energy added from external sources as part of the measurement process but may consume energy during their operation. Active transducers require energy to be added in the measurement environment as part of the measurement process.

Sensing transducers are based on various principles: electromagnetic, electrochemical, and electromechanical are the most common ones used in physiological instruments [1.2, 1.3]. Electromechanical transducers convert mechanical changes such as deformations into electrical signals. For example, pressure sensing transducers consist of a deformable membrane which converts a pressure difference into a movement or strain of the membrane, which in turn transforms into a varying

resistance by a strain gauge or a varying capacitance by parallel plate/interdigitated finger capacitor. The resultant varying resistance or impedance can then be incorporated in a circuit to enable electrical measurements of the pressure. Electrochemical transducers convert chemical energy changes such as redox potentials to electrical signals. A pH probe measuring pH values during the activity of hydrogen ions at its tip of a thin-wall glass bulb is an example. The probe produces a small potential produced from ion exchanges. The pH probe combined with electrical amplifiers transduces the potentials to measureable currents.

The future of physiological sensing would be on miniaturization and integration [1.5]. MEMS stands for MicroElectroMechanical Systems that consists of sensors, actuators, and systems. With MEMS technology, sensors are designed and fabricated using microfabrication and micromachining technologies that enable miniaturization and integrated solutions to advanced sensor problems [1.4-1.6]. MEMS applied to medical care is often called BioMEMS [1.10, 1.11]. Typical applications of BioMEMS are a variety of lab-on-a-chip methods that analyze biological or physiological parameters [1.10]. With the advancement of MEMS and BioMEMS technologies, the sensing transducers can be designed more effectively to meet the requirements of the medical applications.

1.2.2 Wireless Technologies

The deployment of sensing transducers and electronics in healthcare plays a significant role to overcome many problems in disease treatment and diagnosis [1.5]. For advanced applications like implantable devices, wireless solutions are preferred.

The wireless technologies offer a competitive method for therapy or diagnosis, when wires are often bulky, unsafe, uncomfortable or even impossible to be deployed in some circumstances [1.12]. Wireless monitoring and communication allows patient mobility and efficient response in emergency situations.

The wireless communication methods can be categorized into active and passive groups, depending on the power sources required to operate electronics [1.13]. The active devices draw power directly from a battery, while the passive devices harvest power from external or internal sources. This is often called energy harvesting or scavenging. Usually, the active ones have longer communication ranges since the power uses are more efficient while the passive ones need to harvest energy indirectly from environments having in return a shorter communication range due to power limitation.

IEEE has initiated a new working group for wireless personal area networks (WPANs) or Wireless Body Area Network (WBAN), mainly targeted at medical applications [1.14]. It consists of a set of sensing devices, either wearable or implanted into the human body, with a protocol that can communicate to each other to monitor vital body parameters and activities [1.15, 1.16]. It is a short range communication protocol and it has low power consumption requirements. There are several technologies, like Bluetooth, ZigBee, etc. proposed in this working group; however, passive RFID technology would also be a competitive candidate since it does not need a battery in the transponder to operate. Therefore, passive RFID technology has advantages for long-term monitoring compared to other battery based technologies.

1.3 Importance of Batteryless Wireless Sensing Systems for Medical Applications

Wireless communication technologies that use radio frequency to communicate between sensing transducers, measurement instruments, and base stations, etc. provide a better way than the one with wire connections between them. The physical wire connections will limit the mobility of the devices and sometimes cause hazards. This is especially important in such environment like an intensive care unit (ICU) or an operating room (OR) where space is limited. Wireless communication technologies not only solve the cumbersome wire connection problem for external wearable devices but also provide a feasible and comfortable way for implant applications. In addition, some physiological activities require long-term monitoring for proper diagnosis of the diseases, so the low power consumption requirement of the devices is critically important. A wireless sensing transducer that can be operated without a battery in it can definitely prolong the monitoring duration. Overall, a batteryless, wireless sensing system brings significant impacts for medical applications especially for implant applications.

1.4 Dissertation Architecture

Based on different positions of physiological sensing device deployment, it can be divided into either an external or implantable one. For external deployment applications, the physiological devices are attached to the body to read the biological signals. A batteryless wireless pressure monitoring system for sensing wound conditions was demonstrated for this type of applications. For implant deployment applications, the physiological sensing devices are placed inside the body without a

tethered wire to bring the signals outside. An implantable batteryless wireless impedance and pH sensing system for gastroesophageal reflux diagnosis was demonstrated for this type of applications.

In the first part of this dissertation, a batteryless, wireless sensing platform based on passive RFID working principles is presented. Based on this platform, two medical applications are targeted. In the second part of this dissertation, a wireless pressure sensor array is made to monitor the pressure distribution in a certain area without the need of a battery. This pressure sensor array is suitable for long term monitoring of pressure sore development. In the third part of this dissertation, a wireless implantable sensing device is made to monitor reflux episodes in esophagus. This single device consisted of two sensors and presents an accurate way for *in vivo* GERD diagnosis. The passive wireless communication mechanism was demonstrated for multiple transducers integrated in a single transponder device. Finally, a systematic approach on the optimization of the system powering efficiency is attempted and the results are discussed in the Appendix.

CHAPTER 2

A BATTERYLESS, WIRELESS SENSING PLATFORM OVER A PASSIVE RFID COMMUNICATION SYSTEM FOR BIOMEDICAL APPLICATIONS

2.1 Introduction

A telemetry sensing system based on passive RFID technologies has brought great attentions, especially in biomedical applications, due to its sensing capability, wireless communication ability, and without the need of battery for operation in the transponder [2.1-2.8]. It provides a better way to deploy the sensing transponder devices since there is no wire connection between the transponder and the remote reader system. It also provides a feasible way for long term monitoring since the transponder does not need a battery for operation. The sensing systems based on passive RFID technologies can be categorized into two types: by detecting either the resonant frequency changes or the modulated frequency changes [2.9-2.16]. In both cases, the frequency changes of the transponder are modulated by the variations of sensors when sensor characteristics are modified by external conditions. In the first type of sensing system that detects resonant frequency changes, a reference circuit of the remote sensing transponder needs to be configured to produce a reference signal for usage in conjunction with the sensor signal [2.17]. It requires very precise measurements on resonant frequency changes to distinguish different target objects of interest. The second type of sensing system is based on the detection of the modulated frequency changes from the transponder. While

the sensor signals are encoded into frequency variation data, this type of sensing system is more reliable and robust for practical medical applications [2.18-2.20].

Furthermore, the RFID circuit used in the transponder that integrates with the sensors can be realized either in transistor level integrated circuit design or board level circuit design. To demonstrate the capability of our sensing platform that can be used in different medical applications, studied in this dissertation, the approach of using board level circuit design to interface with the sensor is used.

2.2 Proposed Sensing System

2.2.1 System Overview

The proposed sensing system design is based on passive RFID working principles [2.21]. The sensing system includes a transponder and a reader in which the communication is based on inductive link between two coil antennas. Figure 2.1 shows the system block diagram of our sensing system. The working principle of the system consists of two parts, which are RF powering and data transmission. From the reader side, the interrogator frequency source is fed into the power amplifier and radiates the RF energy coupled into the transponder through the resonant circuits. This RF energy is then harvested by the energy harvest circuit of the transponder and builds up the required DC voltage to power up the rest of the circuits on the transponder, such as the frequency generator. The output from the frequency generator has a rectangular waveform with high and low amplitude levels, as shown in Figure 2.2. These high/low signal levels can turn on and off the switch circuit and these loading modulation processes will tune and detune the resonant circuit of the transponder to its resonant

frequency thus vary the signal levels seen on the reader coil. These signal amplitude fluctuations can be detected by the envelope detector circuit of the reader. Because the output frequencies of the frequency generator are modulated by the sensor data, the sensor data can be easily detected by the reader circuit.

The analog outputs of the sensor are processed with analog circuit on the transponder with the sensor data encoded into frequency shifts. The data are transmitted back to reader via the inductive link. On the reader side, the signals are first processed with analog circuits such as an envelope detector and filters. The signals are then acquired by a data acquisition device to convert into a digital format. Then, the data are processed with a digital signal processing technique, such as spectrum analysis, and the data are recorded in digital format.

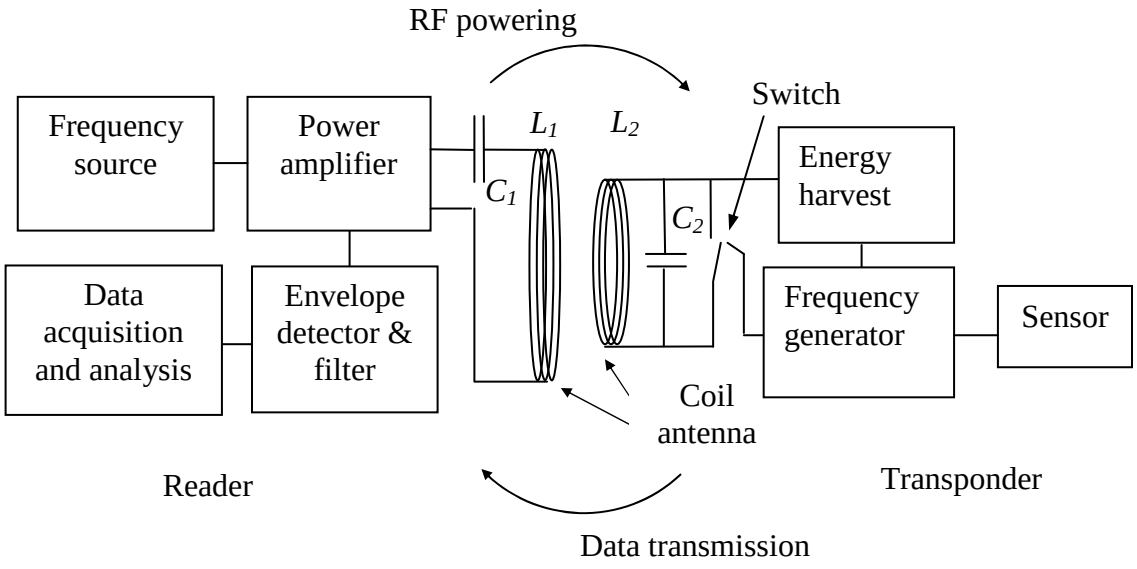

Figure 2.1 System diagram of the system.

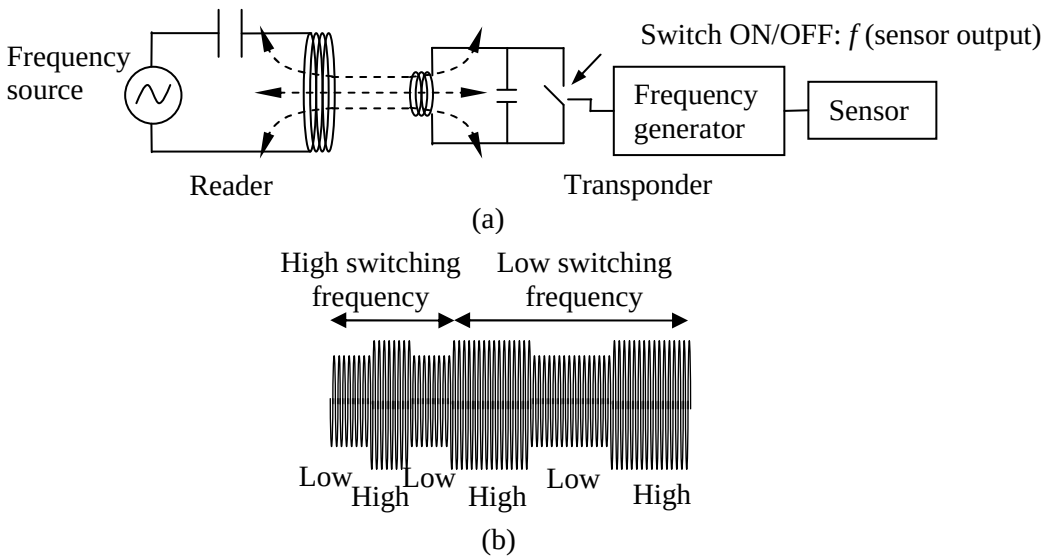

Figure 2.2 (a) A batteryless wireless sensing platform. (b) Signals at the reader coil.

2.2.2 Transponder

The front end of the transponder consists of a coil antenna, denoted as L_2, and a tuning capacitor, denotes as C_2, forming a resonant circuit used to receive RF power from the reader. The transponder circuit was designed on a 4-layer printed circuit board (PCB). A coil antenna with inductance value of 22 µH was made from a 34 AWG magnet wire (Belden Wire & Cable) wound around the PCB. The designed operating frequency was at 1.34 MHz. This is based on the recommended maximum permissible exposure (MPE) of magnetic field is the highest in the frequency ranges from 1.34 to 30 MHz [2.22]. The calculated tuning capacitor was done with a capacitance value of 640 pF based on the formula

$$f_0 = \frac{1}{2\pi\sqrt{LC}} \tag{2.1}$$

where f_0 represents the resonant frequency.

The energy-harvesting unit was designed using voltage multiplier circuitry, including a series of diodes and capacitors with the capacitance values of 100 pF that can build up the DC voltage from the received RF energy. A regulator circuit was implemented (S-817A20ANB, Seiko Instruments) to guarantee a constant DC level for biasing the circuits. Figure 2.3 shows the energy-harvesting circuit which consists of a voltage multiplier and a regulator.

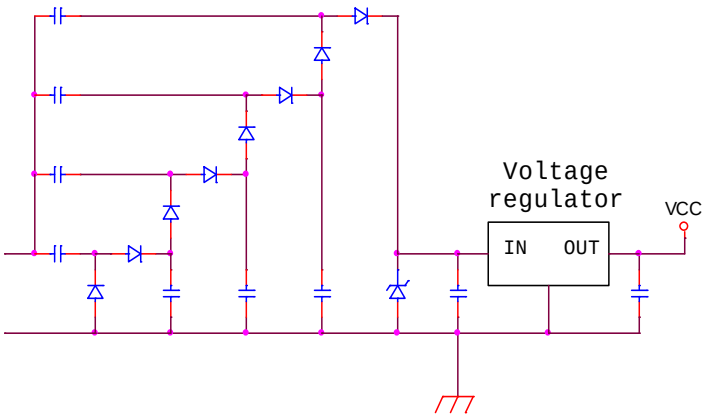

Figure 2.3 Voltage multiplier and regulator circuits.

The frequency generator unit was realized with a relaxation oscillator circuit using comparator ICs (TLV3012, Texas Instruments). The relaxation oscillator circuit consists of a comparator, a capacitor and several resistors. The output frequency of the oscillator was reversely proportional to the time constant at the inverting input and can be calculated from the resistance and capacitance values in the feedback loop of the circuit [2.23]. The frequency generator circuit can be used to interface with both resistive and capacitive type of the sensors [2.24]. Figure 2.4 shows the circuit diagram of the relaxation oscillator. The modulated frequency can be found as

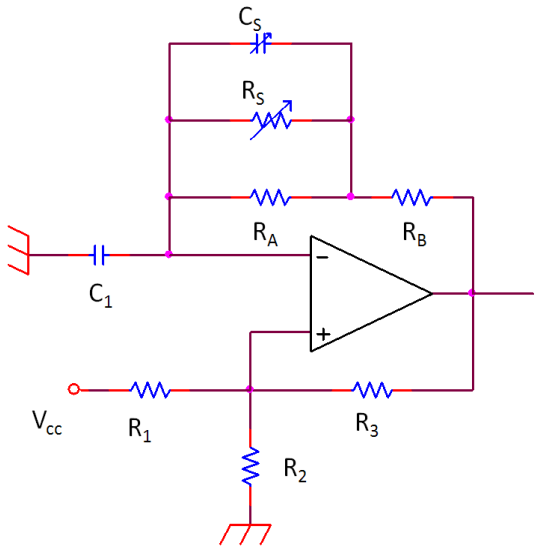

Figure 2.4 Relaxation oscillator circuit to interface with both resistive and capacitive type of the sensors, represented as R_s and C_s.

$$f \propto \frac{1}{\left[\left(R_A // R_S // C_S\right) + R_B\right] \times C_1} \tag{2.2}$$

where R_S and C_S represent the resistive and capacitive type of the sensors connected in parallel, R_A, R_B and C_1 are lumped components. The resistors R_A and R_B have the resistance values of 12 and 10 kΩ, respectively, the capacitor C_1 has the capacitance value of 2.2 nF. With R_S in the range of 0-40 MΩ and C_S in the range of 0-2 pF, the modulated frequencies had the frequency range from 9.5 to 16.8 kHz. Thus, the sensor data were encoded into frequency shifts. The resistors R_1, R_2, and R_3 were designed with the same resistance value of 1 MΩ resulting in a duty-cycle of 50% on the output waveform from the relaxation oscillator. This time domain symmetric output waveform has the optimal amplitude on its power spectrum in frequency domain. Thus, the signal

to noise ratio can be optimized under the same noise level when we perform spectrum analysis on the reader side.

2.2.3 Reader

In this work, a class-E power amplifier was chosen and built for its high efficiency. Because the voltage and current of the amplifier circuit are 180° out of phase, the theoretical power consumption is zero [2.25]. The class-E power amplifiers have been used in other RF power amplifier for biomedical implant applications [2.26-2.28]. The circuit diagram of the class-E amplifier is shown in Figure 2.5.

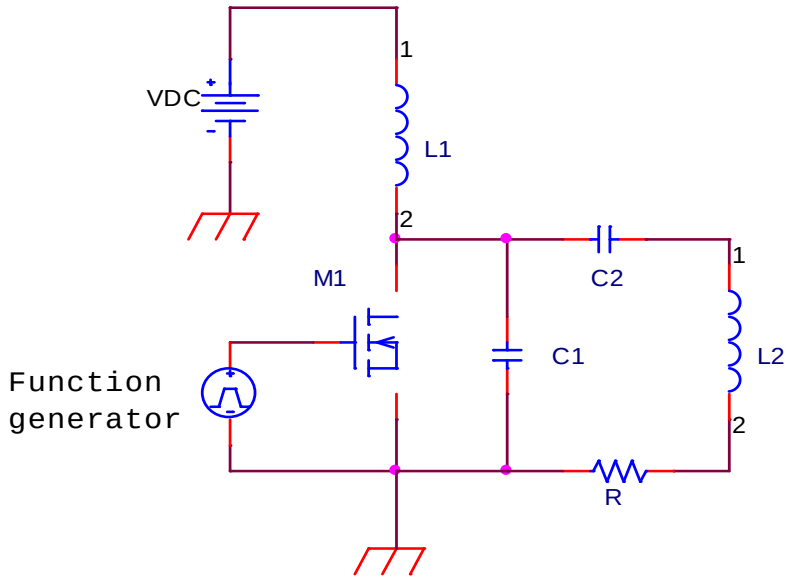

Figure 2.5 A circuit diagram of Class-E power amplifier.

A function generator provided a 0-5 V square wave signals to drive the MOSFET switch M1 (IRL510A, Fairchild Semiconductor), that had low threshold voltage of 1 Volt. A duty-cycle of 30% was chosen to minimize DC power consumption. A portable reader can be powered by batteries eventually. A coil antenna

with a size of 9×12 cm^2 was made from an AWG26 magnet wire wound around a frame resulting in an inductance of 17 µH and a high quality factor Q of 70. Following the calculation procedures for a high quality factor Q approximation in [2.29], the values of C_1 and C_2 were chosen to be 10 nF and 900 pF, respectively.

Figure 2.6 shows the circuit of envelope detector, that includes a diode and RC networks, and a low pass filter for sensor data detection. The diode (1N4936, Vishay Semiconductors) rectified the high voltages at the coil antenna of the class-E amplifier. The time constant of the 100 kΩ resistor and 100 pF capacitor gave a modulation frequency of 0.1 MHz that was suitable for a carrier frequency above 1 MHz. The 4.7 kΩ resistor and 1 nF capacitor suppressed the high-amplitudes of the high-frequency carrier signals. The 1 nF capacitor and 100 kΩ resistor form a low-pass filter to reduce the DC level before the signals were fed into an op-amp buffer. The sensor data were then acquired and logged into a computer by a data acquisition device (NI USB-6210 DAQ, National Instruments) with 16 bit resolution, and the sampling rate of 250 kS/s that was sufficient enough to detect the signal. A system level *LabVIEW* program was used to implement the benchtop spectrum analysis mechanism.

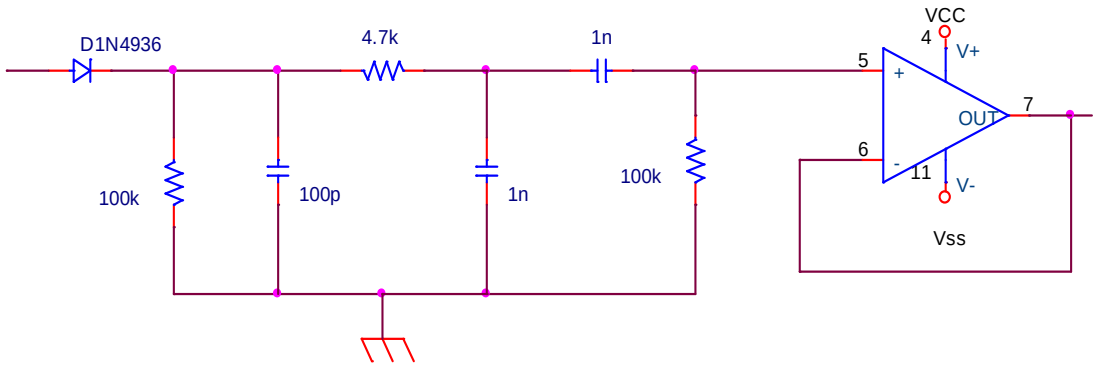

Figure 2.6 Envelope detector and low pass filter circuit.

2.2.4 Read Distance

The read distance of a passive RFID system depends on several factors, such as the supply current at the reader, the power consumption of the transponder circuit, antenna size, coupling efficiency between the two resonant circuits, and quality factor (Q) of the antenna, etc [2.30, 2.31]. The typical read distances of the inductive coupling RFID device are shown in Figure 2.7 [2.32, 2.33].

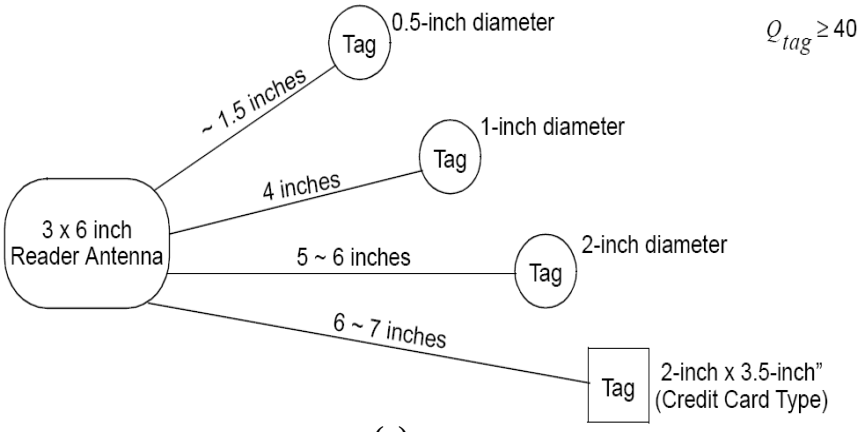

(a)

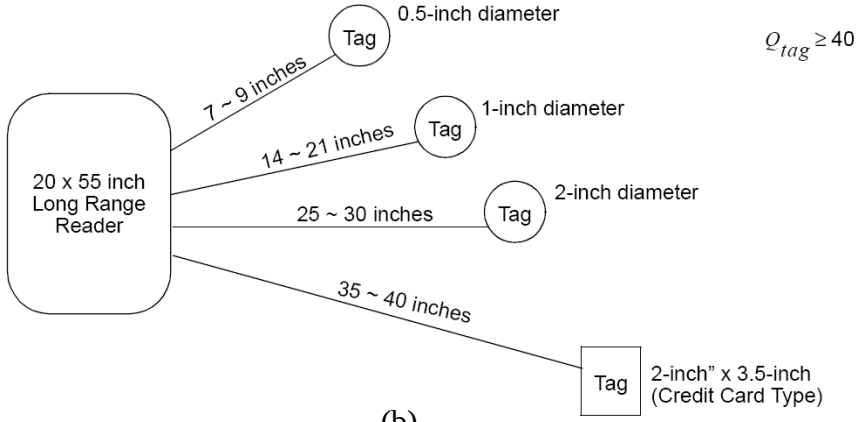

(b)

Figure 2.7 Read ranges vs. tag sizes for (a) proximity applications, and (b) long range applications [2.32, 2.33].

Figure 2.8(a) shows the prototype of the sensing device packaged with biocompatible material, Polydimethylsiloxane (PDMS). The device dimensions were $2.5\times0.8\times0.5$ cm^3 with the coil antenna wound around the PCB. The transponder circuit was design on a four-layer PCB, consisting of the voltage multiplier, regulator, and frequency generator circuit. The surface mount devices (SMD) were used, while the size of our prototype can be further reduced by IC technology. Figure 2.8(b) shows the reader system with a 9×12-cm^2 coil antenna.

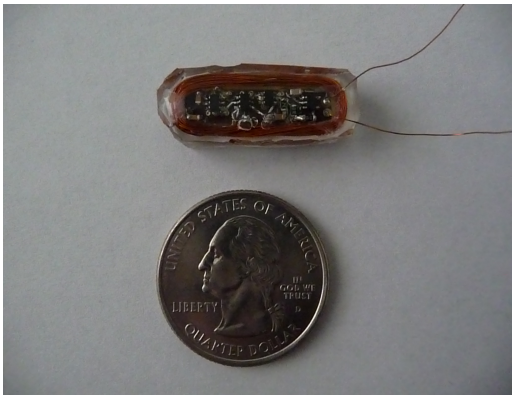

(a)

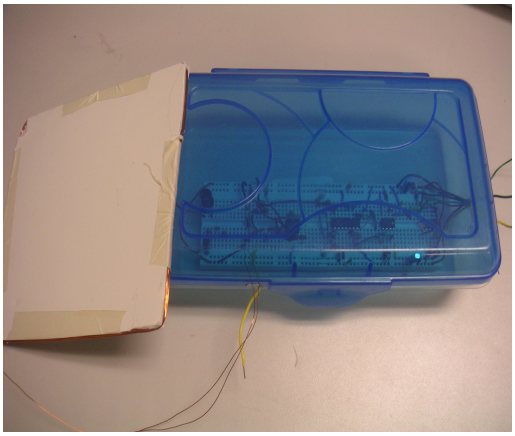

(b)

Figure 2.8 (a) Prototype of the batteryless wireless sensing device. (b) Prototype of the remote reader system.

The optimization of the read distance for inductive coupling passive RFID was discussed in [2.34]. The optimization approaches are twofold. First, the transponder must receive enough power from the reader to be able to operate properly. Second, the reader, on the other hand, must have enough sensitivity to extract the signal from the transponder. The read distance depends on the noise level in the environment as well. The signal to noise ratio of the received signal will degrade along with the distance due to the power budget and environmental noise between the inductive links. Therefore, it is important to characterize the minimal acceptable signal to noise ratio with the maximum read distance to make sure an acceptable signal quality can be obtained. We characterized the minimum acceptable signal to noise ratio by increasing the distance between transponder and reader antenna and measured S/N ratio, as shown in Figure 2.9. The signal to noise ratio was determined by the measured signal amplitude compared to the noise level presented. The measurements on amplitude of frequency spectrum and noise level were performed by using spectrum analyzer (E4403B, Agilent).

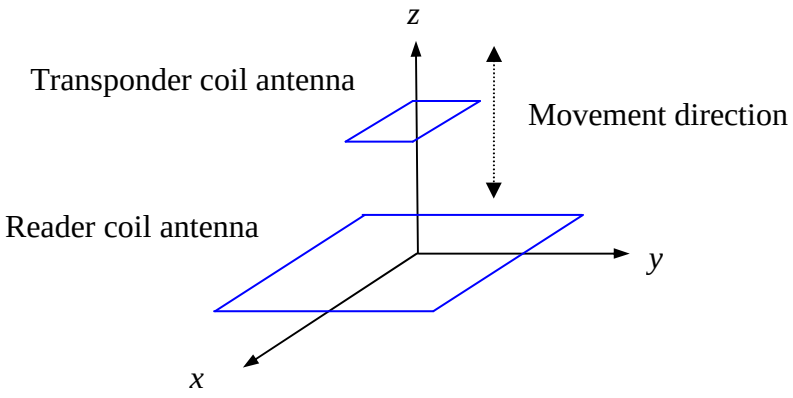

Figure 2.9 Illustration of read distance characterization.

We obtained the maximum read distance of 13cm with minimum distinguishable signal to noise ratio of 2.95 dB. Compared to the typical RFID tag with the size of 2.54 cm in diameter can be read at 10.16 cm from the 7.62×15.24 cm^2 antenna [2.32], our transponder achieved the same range with smaller transponder size and smaller reader antenna.

2.3 Multiple Sensor Integration

Multisensor measurements give more accurate measurements since they provide more information than single sensor measurement [2.35, 2.36]. Multiple sensor data can be used to correlate and calibrate to each other and thus more reliable and correct measurements can be achieved [2.37, 2.38]. Our sensing platform can also be used to integrate with multiple sensors for multisensor measurements. A time-multiplexing switch mechanism is used to multiplex the sensor data; therefore, a sequence of sensor data can be read by using only one reader system. Figure 2.10 shows two topologies used for multiple sensor integration in our study. In the first integration topology, as shown in Figure 2.10(a), we used one frequency generator to process multiple sensor data that were coordinated into a sequence of data stream by a time-multiplexing switch. In this topology, all sensors had the same type of output signal so one frequency generator was used as sensor interfacing circuit. In the second sensor integration topology, all sensors needed to be interfaced with their corresponding frequency generators first, because all sensors had different types of output signals that needed to be processed properly first, as shown in Figure 2.10(b).

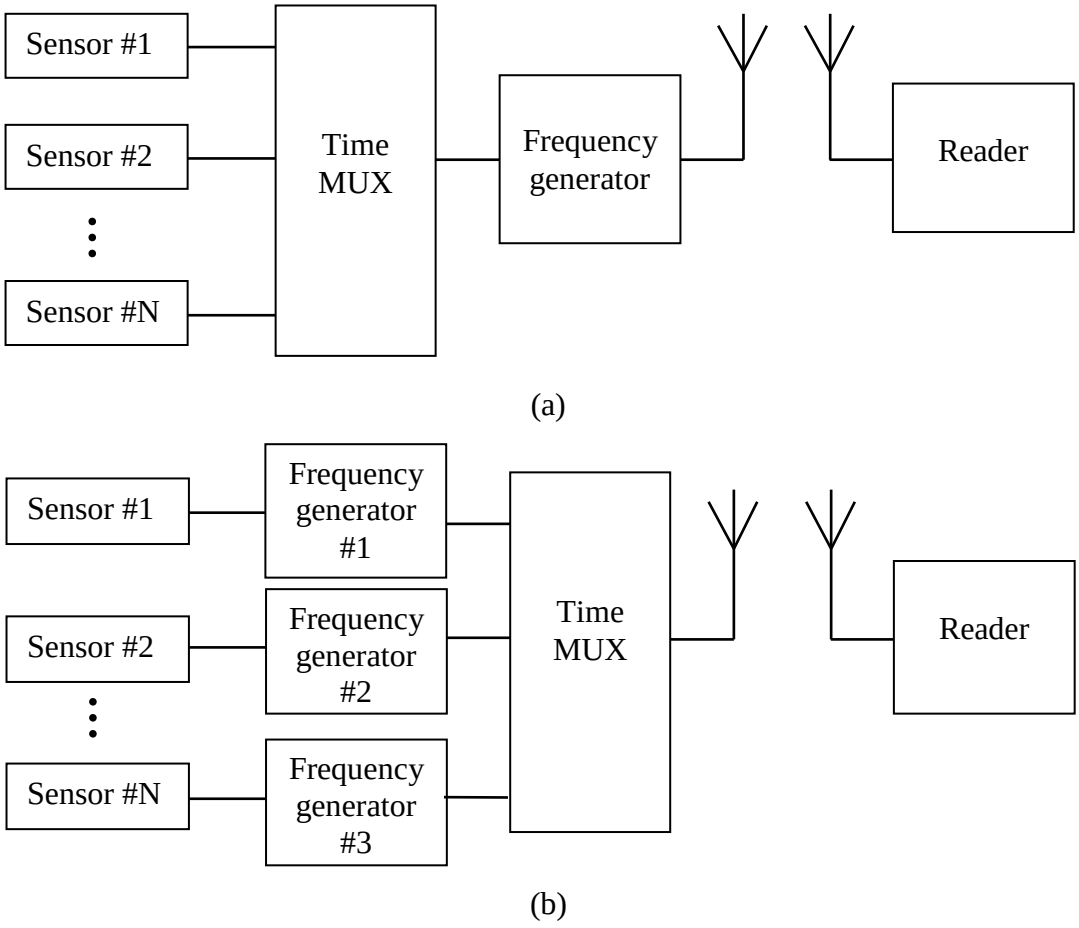

Figure 2.10 Topologies for multiple sensor integration with one reader system, and (a) one frequency generator, (b) multiple frequency generators as sensor interfacing circuits.

2.4 Summary

A batteryless, wireless, sensing system, suitable for biomedical applications, was proposed and the prototype of the system was built. The sensing system contained a reader and a transponder and the working principles were based on a passive RFID system. Sensor signals were encoded into frequency shifts to prevent signal quality

degradation due to the misalignments between two coil antennas that might be caused from motion artifacts in real physiological environment. Our system had competitive performances in read ranges, compared to typical RFID system, with even smaller antenna size in both transponder and reader. Our sensing platform can also be extended to multiple sensor integration suitable for different medical applications that will be studied in this dissertation.

CHAPTER 3

A WIRELESS BATTERYLESS PIEZORESISTIVE PRESSURE SENSING SYSTEM FOR PRESSURE SORE PREVENTION APPLICATIONS

3.1 Motivation

Pressure sores is an important health and economic problem. They affect a large part of hospitalized patients [3.1], and the cost has been estimated more than 6.4 billion dollars per year in United States [3.2]. Several risk factors have been identified for the development of pressure sores classified as extrinsic and intrinsic factors. Extrinsic factors include interface pressure, shear forces, friction, moisture, etc. Intrinsic factors are related to the nutritional state of the patient, age, infection, diseases, etc. Three main mechanical factors are thought to play a part in the development of pressure sores: pressure, friction and shear [3.3]. A prolonged and unrelieved pressure will collapse the vessels while shear and friction will bend the vessels. This will result in the occlusion of blood flow and damage the tissues. Hence, using technologies to detect those factors effectively to prevent pressure sores development is necessary for those patients.

A pressure sensing system for pressure sores monitoring is important for patients who might have higher risks to develop pressure sores. There are several technologies for pressure sores prevention. The seat cushion method is to reduce and redistribute interface pressures for the patient by supplying a compliant support at the patient-seat interface. However, Ferguson-Pell presented an extended review of the seat

cushion selection and noted that no single cushion meets the needs of all users [3.4]. Braden scale is a well-known method to check if the patients have high risks to develop pressure sores [3.5]. Nevertheless, mastering this method relies on professional experience. Using conventional pressure sensors to design tools for interface pressure measurement is also a popular topic. These conventional pressure sensors include conductive polymer sensors, semiconductor and metal strain gages, capacitive, and optoelectronic sensors [3.6, 3.7]. Each of them has its pros and cons, considering its cost, size, repeatability, linearity, hysteresis, temperature dependence, and ease of use, etc [3.6]. The development of pressure mapping systems has enhanced pressure sores risk assessment. This is due to their ability to objectively measure interface pressure and provide computer generated data that are not based on subjective opinions [3.8, 3.9]. Therefore, a pressure sensing system that can show the pressure profiles by taking advantage of conventional sensors has been studied in this work.

In this research, a force sensing resistor is used as the sensing element due to its sensitivity, planar substrate, small size, and relative low cost and [3.6]. The force sensing resistors are laid out in such a way that the pressure mapping system can be realized to visually monitor the pressure points. In addition, in pressure sores prevention applications, a wireless approach is preferred because the wired one creates limitation for patient mobility. Furthermore, a batteryless sensing device provides a good way for long-term use without the need to change batteries. Hence, a prototype of a wireless batteryless pressure sensing system was proposed.

3.2 System Design

The wireless batteryless pressure sensing system consists of force sensing resistors, transponder devices, and a monitoring reader system. The force sensing resistors were in an array format to measure the pressure distribution across an aperture. Resistors were connected to a switching unit to time-multiplex the signals. The pressure information in the format of resistance values was fed into the transponder device to be converted into frequency shift information. The transponder and reader system are based on the passive radio-frequency identification (RFID) principle, hence the pressure information can be wirelessly transmitted to the reader without the need of a battery. The frequency shifts then were extracted by the reader circuit and recorded by a monitoring terminal. Figure 3.1 shows the systematic diagram of our proposed telemetric pressure monitor system.

3.2.1 Pressure Measurement System

Measuring the pressures and shears is the main interest because they are the main factors to cause pressure sores [3.6, 3.10]. A force sensor was chosen to be embedded into a specially designed mechanical structure that can measure both pressure and shear forces. A force sensor responds to forces regardless of the area over which the force is applied while a pressure sensor responds to pressure, which gives an output inversely proportional to the area under a constant force. Therefore, while using force sensors in pressure sensing applications, care must be taken to ensure that the force is applied over the same area [3.6]. In this study, a weight is applied on top of the sensor array to measure the pressure distribution. For this interface pressure measurement, the

maximal pressure encountered is about 500 mmHg (9.7 psi) when a subject is sitting on a hard surface [3.11].

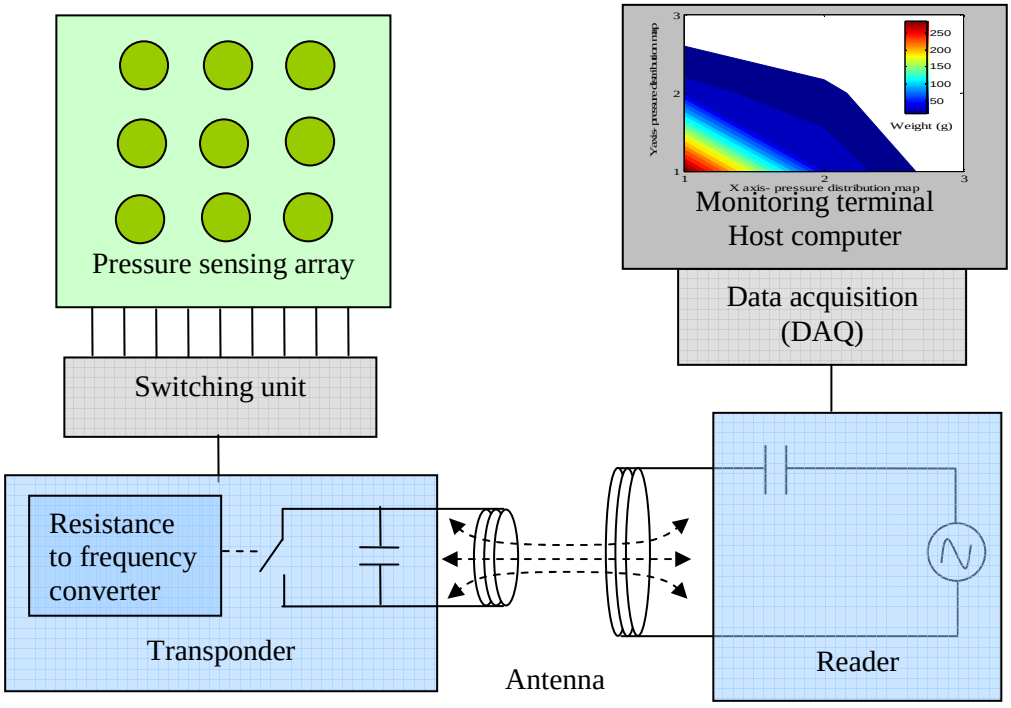

Figure 3.1 Systematic diagram of the proposed pressure monitoring system.

3.2.1.1 Mechanical Design

In this work, a mechanical configuration was designed to measure the pressure distribution. Figure 3.2 shows the cross section of the pressure sensing system. A layer of polydimethylsiloxane (PDMS) was used as the substrate. PDMS, with physical and chemical stability, has a unique flexibility with a shear elastic modulus that varies with different preparation conditions [3.12]. Force sensing resistors were positioned on top of the PDMS substrate with spatial design consideration. On top of each force sensing resistor, a flexible and elastic PDMS buffer structure was introduced to define the

sensing area. This buffer structure not only converts forces into pressures but also measures the shear force due to its elastic properties. Then, a layer of polyimide film was introduced to provide the correlative link between the neighboring sensors. Table 3.1 lists the mechanical properties of the materials used in this study. The polyimide layer not only provides sufficient support strength for objects sitting on top of the structure but also plays a role for measuring shear forces. Finally, a layer of PDMS was introduced on top of the polyimide to protect the pressure sensing structure and provide a soft contact interface with the object.

Table 3.1 Mechanical properties of the materials.

	PDMS	Polyimide
Modulus	360-870 kPa	2.5-15 GPa
Poisson ratio	0.5	0.34
Mass density	0.97 kg/m3	1420 kg/m3

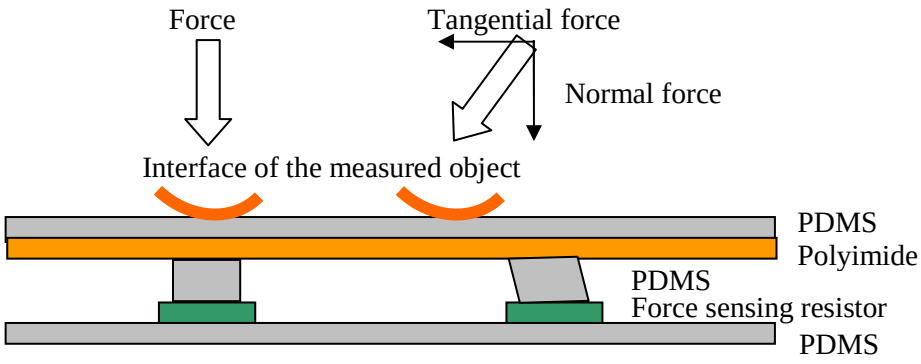

Figure 3.2 Cross section of the pressure sensing system and its capability for pressure and shear force measurements.

As shown in Figure 3.2, when a force is applied directly on top of the sensing area of the force sensing resistor, the force will be converted into pressure that is

defined by the buffer PDMS structure. Moreover, the effects of off-axis loading which contain shear forces information can also be measured in this pressure sensing structure as shown on the right side of Figure 3.2. The mat structure conforms to a deformed surface and the force can be spitted into the normal and tangential components. The normal force will be measured by the sensor underneath and the shear force will contribute to the readings of the neighboring sensors that are connected by the polyimide structure.

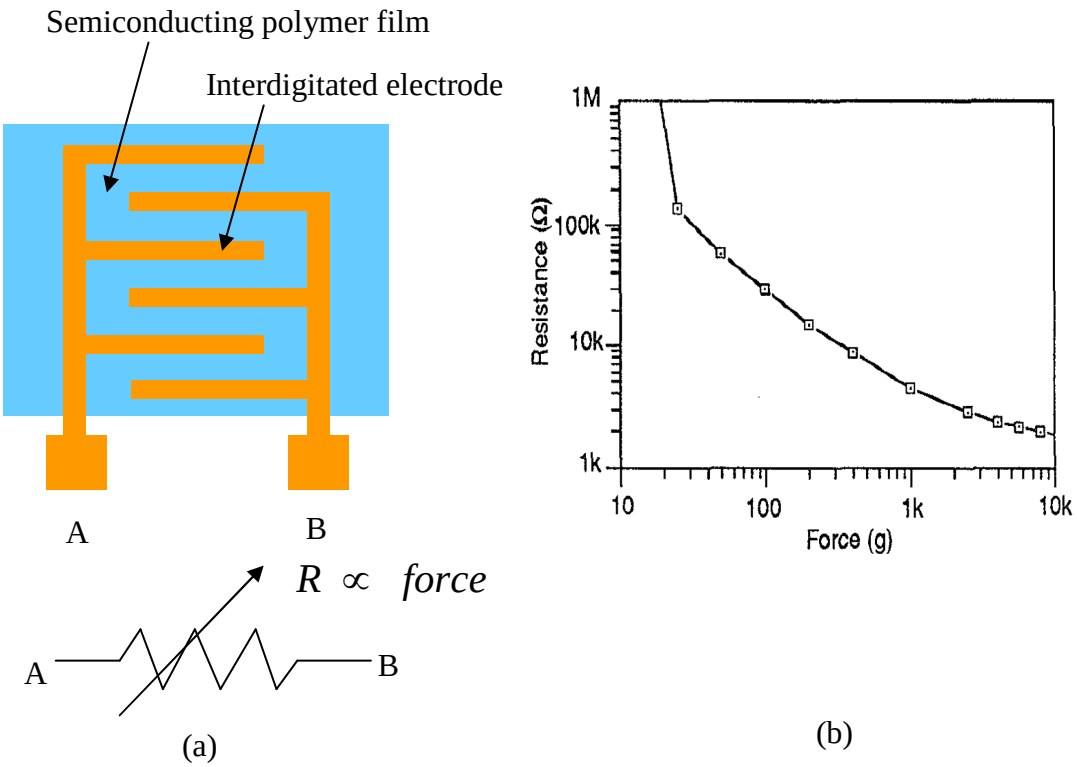

Figure 3.3 (a) Physical structure of force sensing resistor, and its (b) typical characteristic curve of resistance versus force [3.13].

3.2.1.2 Force Sensing Resistor

The force sensing resistor is a flat, flexible device that exhibits a decreasing electrical resistance with increasing force applied normal to its surface [3.13]. The physical structure of a typical force sensing resistor is shown in Figure 3.3(a). An interdigitated finger electrode is deposited on top of the semiconducting polymer film that changes its electrical resistance corresponding to different values of force applied on top of it. When no force is applied to the sensing film, the resistance between the interdigitated finger electrodes is quite high, usually 1 MΩ or more. With increasing force, the resistance drops following an approximate power law. A typical plot of resistance versus force is shown in Figure 3.3(b) [3.13].

3.2.1.3 Pressure Sensing Array

A pressure mapping system that can objectively measure interface pressure and provide the recorded data instead of subjective opinions would enhance pressure sore risk assessment [3.8]. As shown in Figure 3.4(a), our pressure sensing array is composed of 9 force sensing resistors to demonstrate the working principle. The array size can be easily scaled for various applications. For accurate measurements of pressure distributions, a dense sensor array will be necessary. In our design, each force sensing resistor was spaced evenly on top of the PDMS layer with a 3-cm spacing. The spatial resolution then is 9 cm^2. A flexible mat structure was placed on top of the sensor array as the interface. When a weight is on top of the mat structure, the sensor directly underneath the object will respond to the normal pressure reading, while the neighboring sensors will show force information related to shear forces. Figure 3.4(b)

shows that when a force, F, is applied on the mat structure, the closer sensor will show a higher pressure while the other ones show lower readings. This force can be decomposed into normal and tangential forces respectively, to be measured.

The readings related to the shear force could be measured by the closer neighboring sensors. As shown in Figure 3.4(b), when a force, F, was applied on the mat structure, the shear forces, F_L and F_R, were induced. These two forces were further decomposed into their normal and tangential forces, respectively.

$$F_{L,normal} = F_L sin\theta \tag{3.1}$$

$$F_{L,tangential} = F_L cos\theta \tag{3.2}$$

$$F_{R,normal} = F_R sin\alpha \tag{3.3}$$

$$F_{R,tangential} = F_R cos\alpha \tag{3.4}$$

The two normal forces, $F_{L,normal}$ and $F_{R,normal}$, are measured by the sensors underneath with the readings W_L and W_R, respectively. The two tangential forces, $F_{L,tangential}$ and $F_{R,tangential}$, contribute to the shear stress-strain distribution of the mat structure can also be calculated. Assuming that the displacement, Δ, is relatively small so the distance, x, can be expressed as

$$x \cong \frac{LW_L}{W_L + W_R} \tag{3.5}$$

Hence, the force, F_R, can be obtained from

$$F_R \cong \frac{W_R}{\sin\left(\tan^{-1}\frac{\Delta(W_L + W_R)}{LW_L}\right)} \tag{3.6}$$

So, the shear stress, τ, can be calculated as

$$\tau \equiv \frac{F_R}{A} \tag{3.7}$$

where A is the sensing area of the force sensing resistor.

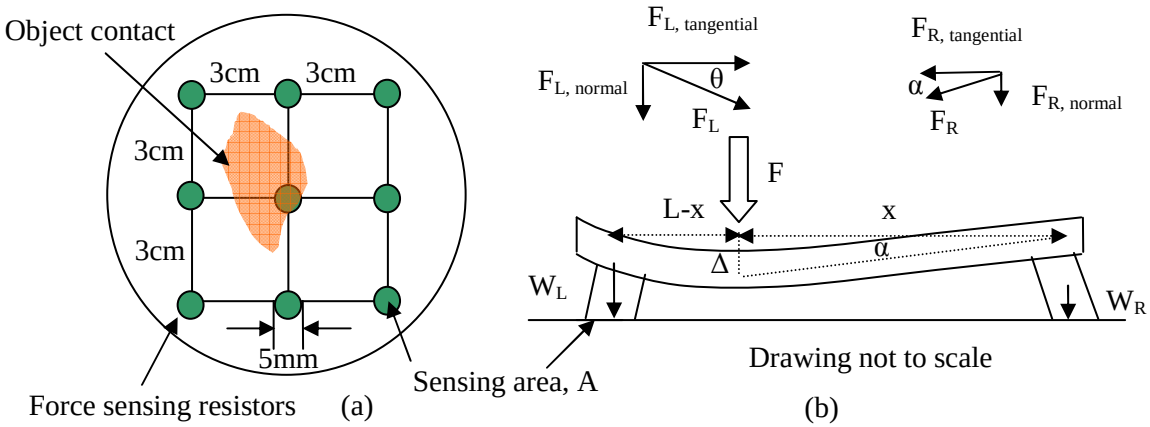

Figure 3.4 (a) Top view of the proposed pressure sensing array. (b) Cross section view to illustrate the normal and shear force measurements.

The stress-strain behavior of the mat structure was simulated using the finite element method ANSYS. Figure 3.5(a) shows the simulation configuration with a thin plate supported at its four corners that is subjected to a force F on the plate. L_1 and L_2 are the length of the plate with a dimension of 3×10^{-2} m and t is the thickness with a dimension of 2×10^{-3} m. E_1 and E_2 are the distances with a dimension of 1.5×10^{-2} m and a contact area of 0.2 cm^2 to the mat structure are defined. The polyimide plate was assumed to be an isotropically and linearly elastic material. As shown in Figure 3.5(b), the corners and the center encountered the highest stress-strain force of 1.89×10^{6} Pa with a 4.35×10^{-4} m displacement. Hence the mat structure can provide enough

supporting stress-strain force within the desired pressure range of 0-10 psi.

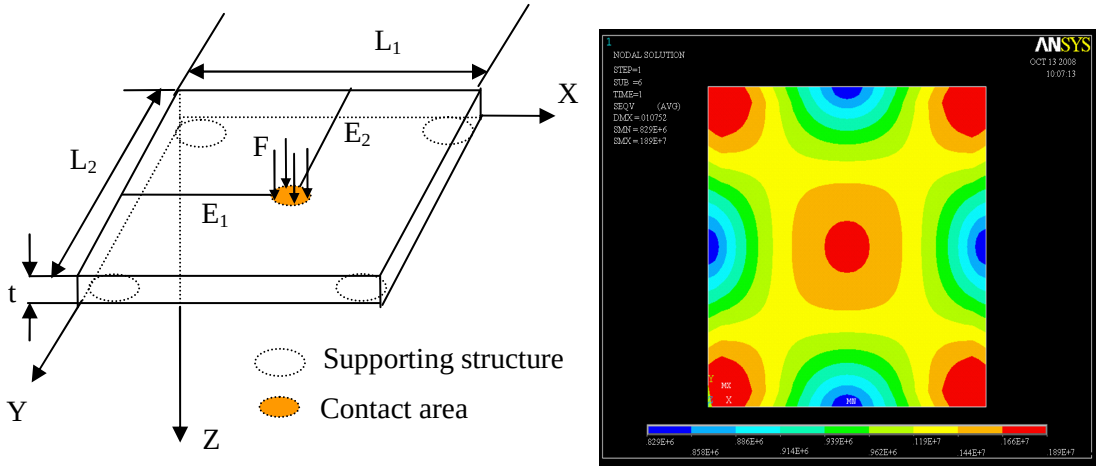

(a) (b)

Figure 3.5 (a) Geometry and loading of the thin plate. (b) ANSYS simulation of the stress-strain behavior of the mat plate structure.

3.2.1.4 Experimental Results

Nine sensors were calibrated with objects weighted from 0 to 400 grams to obtain their individual characteristic curves. Force sensing resistors yield a decrease in resistance with increasing force and their corresponding plots are shown in Figure 3.6(a). After obtaining the curve for each sensor, we can convert the resistance reading back to the weight information. Then a weighted 300 gram object was placed on top of the mat structure to examine the long-term stability performance of piezoresistive type force sensors due to the concern in value drifting issue [3.13]. As shown in Figure 3.6(b), for a period of 7 days, 14 data points were taken to examine the resistance drifting. The maximum resistance drifting is 0.44 kΩ (4.3%). This value is considered

small compared to that for an object weighted in the range of 100 grams which usually yields more than 5 kΩ resistance change. Therefore, the drifts will not be a factor affecting force readings. In addition, in pressure sores prevention application, when the sensor readings have no abrupt and large changes for a long time, which means that the patient has remained in the same position for some time and needs to be rotated to change his/her lying position.

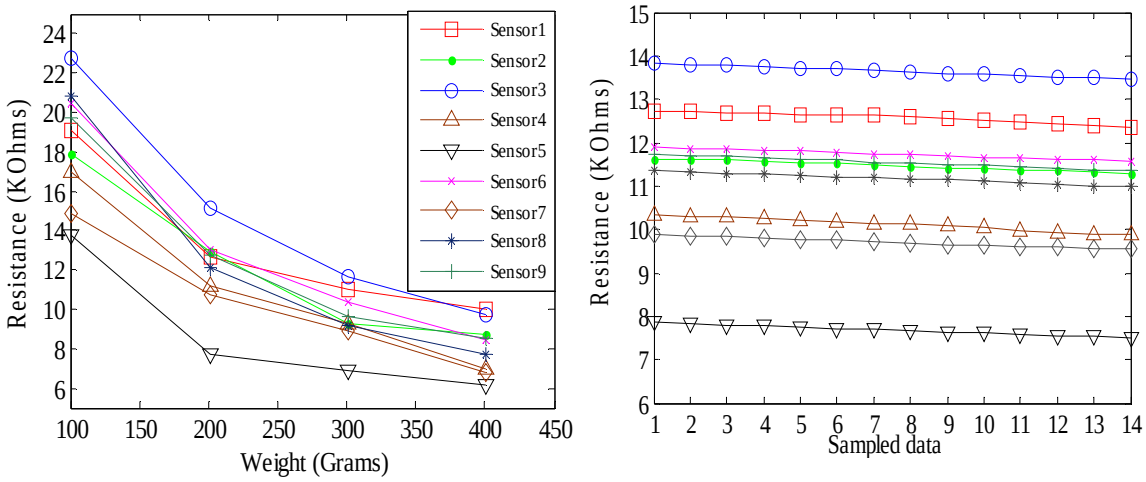

(a) (b)

Figure 3.6 Nine force sensing resistors with their corresponding (a) Characteristic curves. (b) Sensor long-term stability tests for 7 days with two data points taken per day.

The pressure sensor array was further examined on its ability to identify high pressure points. Figure 3.7(a) shows a photo of the pressure sensor array with nine sensor locations indicated. A weight of 300 grams was placed on top of the pressure sensor array in different locations. Figures 3.7(b)-(d) show measured weight distributions when a weight was applied at different locations on the array. Figure

3.7(b) shows the weight distribution when the object was placed at the location (1,1), the sensor at this location indicated that there was a 298-gram weight. The object has a contact area of 19.64 cm^2 to the sensor array. The neighboring sensors (1,2), (2,1), and (2,2) indicated the shear forces induced by the finite contact area with the readings of 42, 35, and 17 grams, respectively. Sensor locations at (3,1), (3,2), (3,3), (1,3) and (2,3) indicated no force since the object was far away from these positions. In Figure 3.7(c), when the 300-gram object was placed on top of the sensor (2,2), it indicated that the object was on top of it with a 290 grams reading and its closer neighboring sensors (1,2), (2,1), (2,3), and (3,2) had the readings of 16, 15, 17, and 15 grams, respectively. Sensor locations at (1,1), (1,3), (3,1), and (3,3) indicated no force occurred at those points. Similarly, in Figure 3.7(d), the sensor position (1,2) indicated that a 293 grams object was placed on top of it and its closer neighboring sensors (1,1), (1,3) and (2,2) had the readings of 23, 25, and 20 grams, respectively. Sensor locations at (2,1), (2,3), (3,1), (3,2), and (3,3) indicated no force occurred at these points.

A weight of 300 grams with a contact area of 0.2 cm^2 to the sensor array was placed in the center among the locations (1,1), (1,2), (2,1), and (2,2) to examine the shear force. Sensor locations (1,1), (1,2), (2,1), and (2,2) had the readings of 76, 78, 75, and 76 grams, respectively. Sensor locations at (1,3), (2,3), (3,1), (3,2), and (3,3) indicated no force occurred at these points. From equation 3.6, the force, F_R, was estimated as 36.75 N . The shear stress can be obtained as 1.81×10^6 N/m^2 (Pa) from equation 3.7. This value is close to the result in the ANSYS simulation.

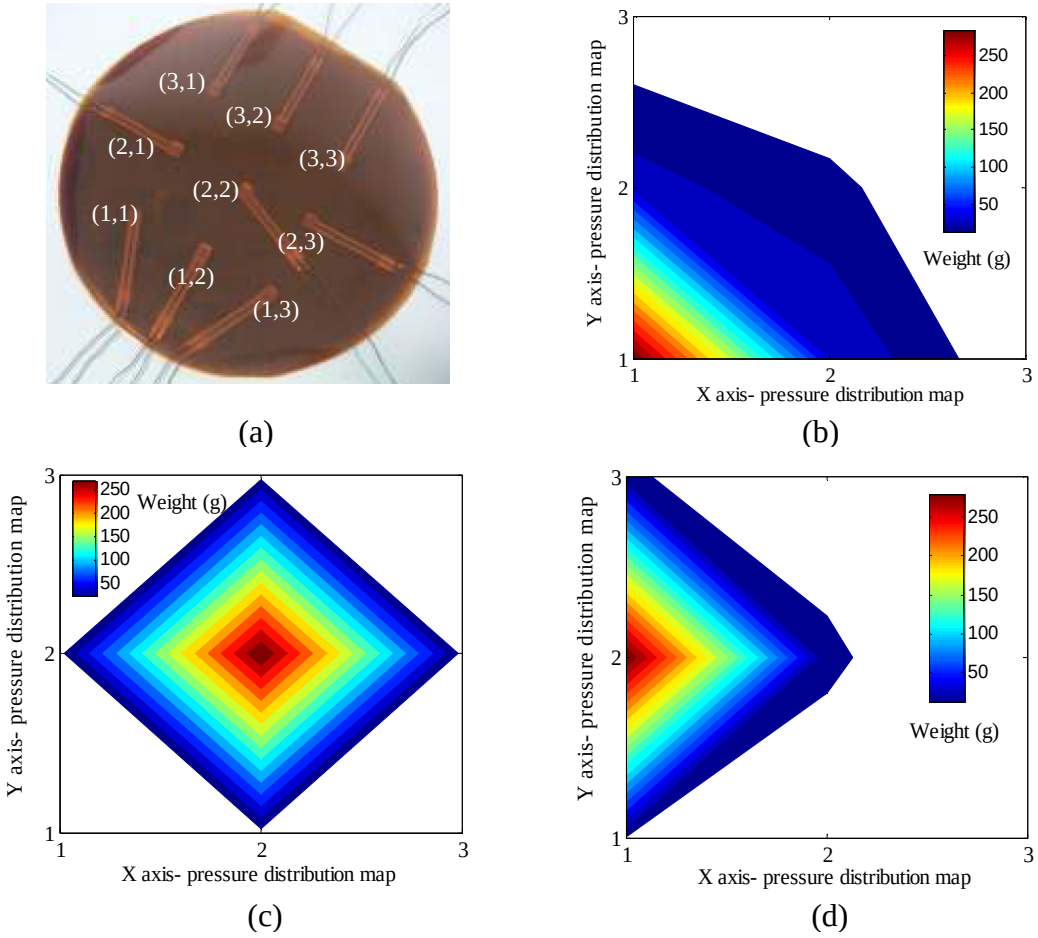

Figure 3.7 (a) Photo of the pressure sensor array, and measured pressure distribution profiles of the sensors located (b) at the corner, (c) in the middle, and (d) at the boundary.

3.2.2 Batteryless Telemetry Monitoring System

The telemetry is based on inductive coupling between two coils. As shown in Figure 3.1, the reader coil generates electromagnetic fields coupling into the transponder coil. Both coils are connected to capacitors forming resonant circuit. In the near field region, the impedance seen by the reader coil changes when the switch at the

transponder opens or closes. This load modulation alters the voltage level at the reader coil. As a result, the transponder switching frequency can be extracted at the reader using envelope detection [3.14].

3.2.2.1 Transponder Architecture

The transponder consists of an antenna, a tuning capacitor to receive power and modulate sensor data, a voltage multiplier and a regulator to build up a constant DC voltage, and a relaxation oscillator to transduce resistance variations to frequency-varying signals. The frequency (f) of the relaxation oscillator can be calculated as

$$f \propto \frac{1}{\left[(R_A // R_S) + R_B\right] \times C_1} \tag{3.8}$$

with a piezoresistive force sensor R_S and lumped components R_A, R_B and C. A low-power op-amp was used as a comparator and the resistors R_A and R_B are 20 kΩ and 10 kΩ, respectively. The capacitor C_1 is 1 nF. With R_S in the range of 0-40 MΩ, the modulation frequency ranges between 7.5 and 16.8 kHz.

3.2.2.2 Reader Configuration

The reader includes a class-E power amplifier to generate high electromagnetic fields and an envelope detector to read the load modulation signals. A frequency source provides the carrier signal feeding the amplifier at the resonance frequency resulting in a high voltage at the reader coil. With the modulation, the voltage levels at the reader coil fluctuate. The pressure sensor resistance signal is extracted by an envelope detector and fed through a band-pass filter to suppress the high frequency carrier.

3.2.2.3 Experiment Results

A transponder device was made on a 4-layer printed circuit board (PCB). Figure 3.8 shows the prototype of the transponder integrated with the force sensing resistor. A coil antenna of 22 µH was made from a 32 AWG magnet wire wound around the PCB.

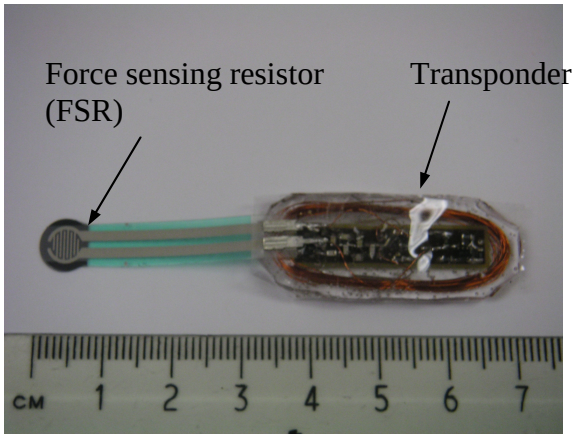

Figure 3.8 The transponder integrated with piezoresistvie force sensing resistor.

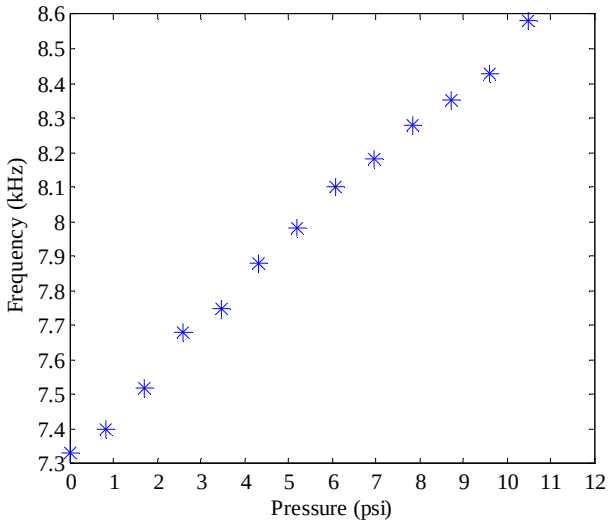

Figure 3.9 The measured frequency shift as a function of pressure change.

When connected to a capacitor of 680 pF, the device operated at 1.3 MHz. The pressure sensing transponder device was characterized with a pressure range from 0 to 10 psi. By adding weights onto the sensing area the corresponding frequency shifts were measured. The reader was placed 12 cm away from the transponder device. Figure 3.9 shows the frequency over the pressure range from 0 to 10 psi along with the respective sensor resistance changes. The reading frequency increased from 7.35 to 8.55kHz with a 0.12 kHz/psi resolution. The device is capable of reading the pressure wirelessly without a battery at the sensor.

3.3 Summary

A wireless batteryless sensing system that can monitor pressure distribution was presented. In this work, a pressure sensor array was built to detect pressure distribution in a certain area for sensing wound condition in pressure sore prevention applications. The experimental results showed that the system can not only indicate the high pressure points but also indicate shear force information over a contact area. Stability tests of the sensor were carried out for long-term use purposes. The experimental results indicated that the drifting of reading was smaller than the readings for high pressure indications. The pressure information was sent to the reader system wirelessly without the need of a battery in the sensing device. The experimental results showed that the reading frequency increased from 7.35 to 8.55 kHz over the pressure range from 0 to 10 psi linearly.

CHAPTER 4

AN IMPLANTABLE, BATTERYLESS AND WIRELESS CAPSULE WITH INTEGRATED IMPEDANCE AND PH SENSORS FOR GASTROESOPHAGEAL REFLUX MONITORING

4.1 Introduction

Gastroesophageal Reflux Disease (GERD) is a medical condition that affects approximately 15% of adult population in the United States and is one of the most prevalent clinical conditions afflicting the gastrointestinal tract [4.1]. GERD refers to symptoms or tissue damage caused by the reflux of stomach contents into the esophagus and pharynx. The reflux contents are both acidic and nonacidic [4.2-4.4]. GERD has been associated with a major risk factor for esophageal cancers which have the fastest growing incidence rate of all cancers in the developed countries [4.5]. Therefore, monitoring GERD symptoms accurately, reliably and comfortably is important for treatment screening.

Multichannel intraluminal impedance (MII) probe is a currently available instrument that has been used to correlate symptoms with episodes of gastroesophageal reflux [4.6]. Whereas electric conductivity is directly related to the ionic concentration of the intraluminal content, materials with high ionic concentrations (e.g. gastric juice or food residues) have relatively low impedance compared with that of the esophageal lining or air [4.7]. Although the MII probe system brings more accurate monitoring

results compared to the conventional pH meter alone, patient tolerability is too low for patient to complete the test [4.8]. The tethered sensor probe requires a transnasal insertion procedure and the wire, connecting from the electrodes that stay inside the esophagus to the external electronic unit worn by the patient, stays transnasally for 24 to 48 hours while the patient supposedly resumes normal daily activities. The wired feature limits the clinical utility and accuracy of this technique for protracted monitoring of gastroesophageal reflux. A miniature wireless device that does not require tethered external connections is thus preferred for esophageal reflux monitoring.

To date, a wireless pH monitoring capsule (Bravo, Medtronic) has been used in some clinical practices [4.9]. However, it cannot detect non-acid reflux and has a limited battery life of 48 hours unless prolonged [4.8, 4.17]. Recent studies and reviews have suggested combined pH and impedance monitoring increased the accuracy of GERD diagnosis [4.10, 4.11]. Lately, a combined impedance and pH sensor capsule that could detect both acid and non-acid reflux was developed using a microcontroller and a wireless transmitter [4.12]. However, the device has limited sampling rates to conserve battery energy and may miss reflux episodes between sampling. The limited battery lifetime prohibits the possibility of prolonged measurements that in some clinical cases are needed for increased diagnosis accuracy [4.13]. Table 4.1 compares different sensing technologies for GERD monitoring.

In this work, passive telemetry was demonstrated to achieve the reflux monitoring wirelessly. The system configuration is shown in Figure 4.1. The implanted sensor harvests radio frequency (RF) power transmitted from an external reader and

sends the modulated impedance and pH data as frequency shifts back to the reader. A prototype of the implantable, batteryless, wireless capsule integrated with impedance and pH sensors along with its external reader unit was designed. The whole system was tested with benchtop experiments and *in vivo* live pig animal experiments to validate the system performances.

Table 4.1 Comparison of different GERD monitoring technologies.

	Conventional Esophageal Impedance and pH Study	Commercially Available Wireless pH Sensor
Usage	Catheter based with transnasal wire connection [4.6, 4.7, 4.17, 4.18].	Wireless communication between sensor and reader [4.8, 4.9, 4.17, 4.18].
Capability	Detect acid and non-acid reflux episodes [4.2, 4.3, 4.4, 4.17, 4.18].	Only detect acid reflux episodes [4.2, 4.3, 4.4, 4.17, 4.18].
Limitation	Patient tolerability is low [4.8, 4.17].	Require batteries, up to 48hrs unless prolonged [4.8, 4.13, 4.17].

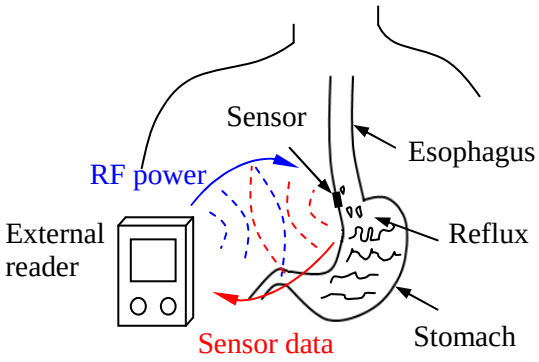

Figure 4.1 Schematics of the wireless batteryless sensing system consisting of an implant sensor and an external reader.

4.2 Methods

4.2.1 System Overview

The sensing system includes a transponder and a reader in which the communication is based on inductive coupling between two coil antennas. This technique has been widely used in passive RFID (radio frequency identification) systems [4.19]. Figure 4.2 shows the system blocks diagram of our proposed system. It consists of coil antennas, denote as *L*, and the tuning capacitors, denote as *C*, forming a resonant circuit and they are tuned to the resonant frequency to optimize the coupling efficiency. This resonant circuit uses the inductive link between reader and transponder for radiating RF power and transmitting sensor data. To power up the transponder, the reader has an interrogatory frequency source to provide the desired operation carrier frequency and a high efficiency power amplifier circuit suitable for powering the implant in biomedical applications. To detect the data, the reader has the envelope detector and filter unit to recognize the data and filter out the noise. The data are acquired by a data acquisition device and then investigated by spectrum analysis methods. The transponder has the energy harvest unit to harvest the RF energy generated from the reader and provides the required power for the rest of the circuitry on the transponder. The impedance and pH sensor are connected to their corresponding frequency generators with proper sensor interfacing circuitry. The modulated frequency of impedance and pH data stream is time-multiplexed and then transmitted back to the reader.

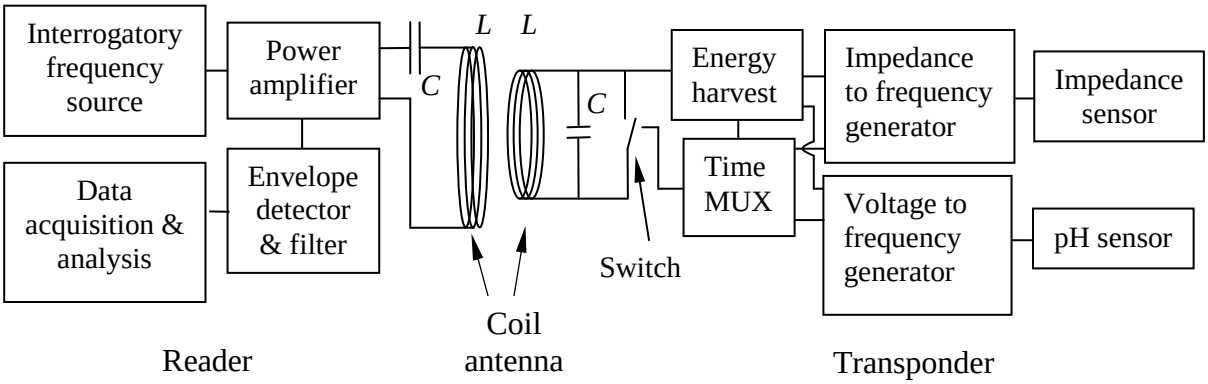

Figure 4.2 System diagram of the proposed system.

4.2.2 A Batteryless, Wireless Sensing Platform

A batteryless wireless sensing platform consists of an embedded sensor transponder and a remote reader system, as shown in Figure 4.2. On the reader side, the interrogatory frequency source generates electromagnetic fields through the reader coil antenna and coupling into the transponder coil antenna. The transponder can harvest the electromagnetic energy to power the frequency generator circuit without the need of battery. The frequency generator circuits are designed as interfaces of the sensors so the sensor data are encoded into frequency shifts. A relaxation oscillator is designed to implement the frequency generator, which consists of a comparator, a capacitor and several resistors [4.20]. The output frequency of the oscillator is reversely proportional to the time constant at the inverting input and can be calculated from the resistance and capacitance values in the circuit. Thus, the sensor data are encoded into frequency

shifts. The frequency generator circuit can process both resistive and capacitive type of the sensors [4.21]. An unit gain buffer amplifier along with the frequency generator circuit is used as an interface of the pH sensor. Therefore, the action potential generated from pH sensor can also be encoded into frequency shifts. The output from the frequency generator has a rectangular waveform that can turn on and off the switch. These loading variations will tune and detune the transponder resonant circuit to its resonant frequency and cause the signals seen from the reader to have different signal levels, high and low, respectively. These high and low signal levels can be detected by the circuitry of the reader and recorded by the monitoring unit. Since the output of frequency generator is modulated by the sensor data, the data can then be detected by the reader circuit. Figure 4.3 shows the typical detected frequencies of impedance and pH sensor when the sensors are positioned in air environment.

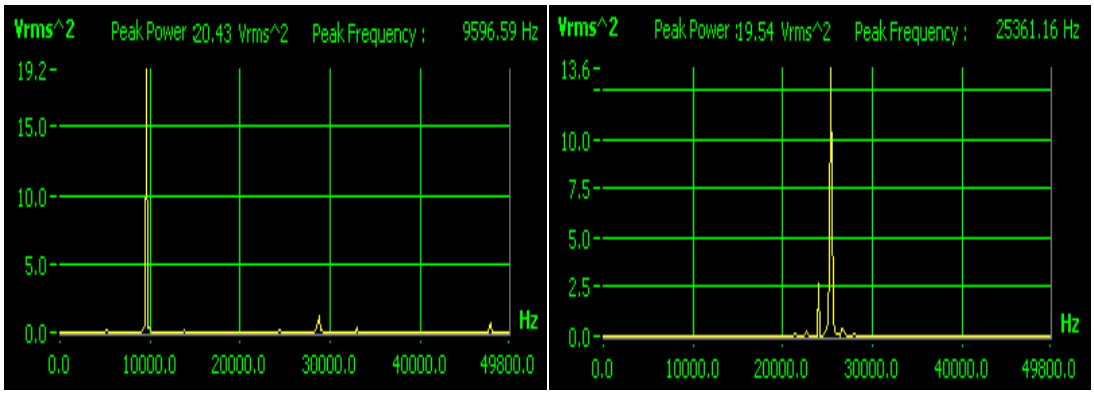

(a) (b)

Figure 4.3 Typical detected frequencies for (a) impedance sensor, and (b) pH sensor in air environment.

4.2.3 Impedance Sensor

In this research, the interdigitated electrode is designed to realize the impedance sensor because of its sensitivity to impedance changes [4.22]. The electrode contains 6 fingers that are 0.18-mm long, 0.18-mm wide and with a 0.18-mm spacing with a printed circuit board design. The material of our sensing electrodes is made of copper. The electrical property of the electrode can be represented by variable resistors and variable capacitors in parallel [4.23]. The resistance variations are due to the conductivity change while the capacitance variations are due to the dielectric constant changes of different tested materials. The material with low impedance such as acid has low resistance and high capacitance resulting in a high-frequency output. For high impedance material such as air, the resistance is high and the capacitance is low resulting in a low-frequency output.

It is known that a lower pH number indicates higher H^+ concentration which reduces the impedance [4.24]. However, it is important to realize that the measured frequencies of the impedance sensor are based on the ion concentrations of the solutions. The measured high frequency could be a result from either acid or non-acid materials as long as it contains high concentration of ion. For this reason, it is important that an impedance sensor deployed along with a pH sensor to verify the acidity of the reflux.

4.2.4 pH Sensor

Bravo pH monitoring devices have prominent and stiff glass electrodes outside the capsules and they need to be calibrated before use which is not convenient for doctors and patients [4.25]. MII-pH monitoring electrode has a pH catheter structure, to be inserted transnasally into the esophagus, which is not comfortable for the patients [4.8]. In this work, an iridium oxide (IrOx) based pH sensing electrodes are made on the thin flexible substrates that can be easily embedded into an implantable device. Both iridium oxide sensing films and Ag/AgCl reference electrodes are formed on a single polyimide flexible substrate by sol-gel, dip-coating and thermal oxidation processes. Fabrication processes for our deformable potentiometric pH electrodes were presented in [4.26]. The IrOx pH sensors, with a nanoscale amorphous surface, exhibited super-Nernstian responses of sensitivity between –69.6 and –71.6 mV/pH in the pH range from 1.9 to 12 at 25°C. For acid solution, our pH sensor has a higher action potential level resulting in a high output frequency in our pH sensor circuit. For alkaline solution, our pH sensor has a lower action potential level resulting in a low output frequency in our pH sensor circuit.

4.2.5 Dual Sensor Integration

To integrate impedance sensor and pH sensor for GERD monitoring is important, since it provides a complete solution for detecting both acid and non-acid materials [4.15-4.17]. For implant application, to read the data from impedance and pH sensors, it is preferable to have only one implant connected to two sensors, rather than having two implants with their impedance or pH sensor separately. This way the size of

the implant can be minimized. In addition, to detect GERD episode properly, both sensors should be positioned as close as possible so that the reflux activities can be measured correctly within the same spatial region.

A simple and reliable architecture to integrate both impedance and pH sensors with a time-multiplexing scheme is used in this study. As shown in Figure 4.2, the impedance and pH sensors are interfaced with their corresponding frequency generators while each of them generates different frequency ranges for each sensor. The frequency gap between the variations of impedance and pH sensor is properly designed so that the frequency ranges of these two data will not overlap and cause error readings. Then, the modulated sensor data are coordinated into a sequence to be transmitted with time-multiplexing scheme. Thus, we can use one reader to monitor dual sensors that are integrated into a single implantable capsule. The time-multiplexing scheme can be realized using a switch mechanism and its control signal can be adjusted to satisfy the required sampling rate needed for the monitoring. The sweeping frequency between two sensors is designed for 1 Hz.

4.2.6 Transponder Design

The transponder circuit was designed on a 4-layer printed circuit board (PCB). A coil antenna with the inductance value of 22 μH was made from a 34 AWG magnet wire (Belden Wire & Cable) wound around the PCB. We designed our operating frequency at 1.34 MHz owing to the recommended maximum permissible exposure (MPE) of magnetic field is the highest in the frequency ranges from 1.34 MHz to 30 MHz [4.27]. The calculated tuning capacitor was 640 pF based on the formula

$$f_0 = \frac{1}{2\pi\sqrt{LC}} \tag{4.1}$$

where f_0 represents the resonant frequency.

The energy harvesting circuit, consisting of a series of diodes and capacitors with the capacitance value of 100 pF, builds up the DC voltage from received RF energy. A regulator circuit is implemented (S-817A20ANB, Seiko Instruments) to guarantee a constant DC level for biasing the circuits. Two frequency generators for impedance sensor and pH sensor are designed correspondingly, that are realized with relaxation oscillator circuits using comparator ICs (TLV3492, Texas Instruments). For impedance sensor, its modulated frequency ($f_{impedance}$) can be found as

$$f_{impedance} \propto \frac{1}{\left[\left(R_A // R_S // C_S\right) + R_B\right] \times C_1} \tag{4.2}$$

where impedance sensor represented by R_S and C_S in parallel, and R_A, R_B and C_1 are lumped components. The resistors R_A and R_B are with the resistance values of 12 kΩ and 10 kΩ, respectively, the capacitor C_1 is with the capacitance value of 2.2 nF, along with impedance sensor parameters, R_S and C_S, forming a feedback loop to its inverting terminal of the comparator. With R_S in the range of 0-40 MΩ and C_S in the range of 0-2 pF, the modulation frequencies vary from 9.5 to 16.8 kHz. For pH sensor, its modulated frequency (f_{pH}) can be found as

$$f_{pH} \propto \frac{1}{R_1 \times C_1} \tag{4.3}$$

where R_1 and C_1 are the resistor and capacitor with the values of 13 kΩ and 1 nF forming a feedback loop to the inverting terminal of the comparator. An unit gain buffer amplifier is designed using low input bias current op-amp (LMV301, National Semiconductor) that serves as an interface between the pH sensor and the relaxation oscillator circuit. When the pH values change from 1 to 12, a pH sensor generates output potential voltages from 0.5 mV to -0.1 mV, the modulated frequencies are from 30.95 to 24.25 kHz.

The output signals from frequency generator circuits of impedance and pH sensor are fed into one of the switch sets of a quad SPDT switch (TS3A44159PWR, Texas Instruments) to multiplex the data. Therefore, the impedance sensor and pH sensor data are coordinated into a sequence of data stream. To ensure the performance of the dual sensor, the impedance and pH electrodes are isolated using the rest of the switch sets of a qual SPDT to prevent the sensor cross talk interference.

Figure 4.4(a) shows a transponder prototype with a size of 1×1.2×3.8 cm^3. The circuits are designed using the surface mounted (SMD) passive components and the off-the-shelf discrete IC components on printed circuit board to demonstrate the feasibility and performances, while the size can be further reduced by designing the transistor level integrated circuit. The board was then coated with biocompatible material, polydimethylsiloxane (PDMS), for implant applications so as to prevent short circuit when placed in the esophagus. The small windows expose the sensing electrodes to make contact with the refluxant. The impedance sensor and pH sensors were positioned close to each other so the episodes of the refluxant can be detected correctly.

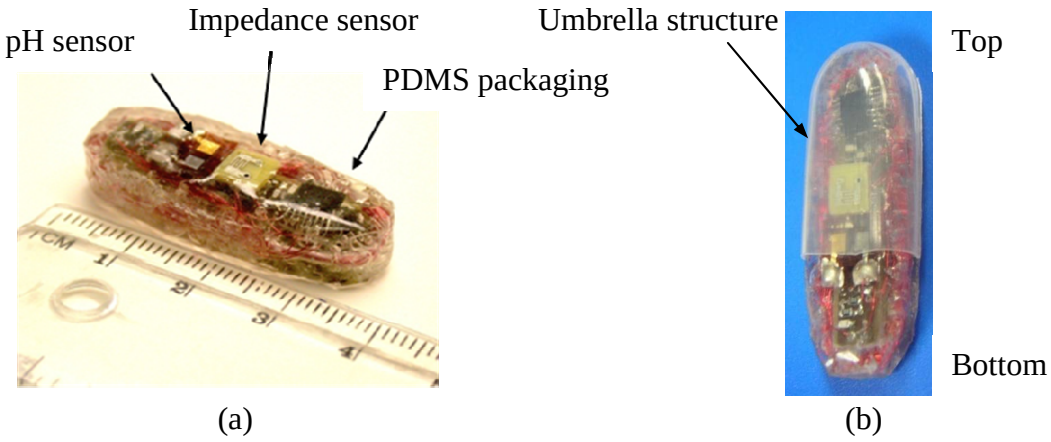

Figure 4.4 (a) The prototype of the implantable, batteryless, wireless capsule integrated with impedance and pH sensors. (b) Umbrella structure for unidirectional reflux activities monitoring.

In order to distinguish the direction of reflux episodes correctly, an umbrella structure was designed. The direction of the refluxant coming out from the stomach is from bottom to top, while the direction of drinking liquids from the mouth is from top to bottom. We need to filter out the data caused by the drinking water. Therefore, an umbrella structure made of polyimide was designed to provide a simple and feasible way for unidirectional detection of the reflux activities, as shown in Figure 4.4(b). When the liquids flushed from bottom to top, the liquids can touch with the impedance and pH sensing electrodes and gave the readings of the tested liquids, correspondingly. When the liquids flushed from top to bottom, the impedance and pH sensing electrodes will be protected from touching the liquids, therefore, the readings of both sensors will not be affected by the tested liquids. Hence, a simple and feasible method for unidirectional monitoring on reflux activities was performed.

4.2.7 Reader Design

The reader includes a power amplifier, which generates high electromagnetic fields coupling into the transponder, and an envelope detector to read the load modulation signals. As shown in Figure 4.2, a frequency source provides carrier signals feeding to the amplifier. The source is adjusted to the resonant frequency of the LC circuit resulting in a high voltage at the reader coil. When modulation occurs, the signal levels at the reader coil fluctuate. The signal is extracted by the envelope detector and fed through a band-pass filter to suppress the high frequency carrier. Then, the signal was amplified and processed.

In this work, a class-E power amplifier was chosen and built for its high efficiency. The class-E power amplifiers have been used in RF power transfer for biomedical implant applications [4.28-4.30]. A frequency source provided 0-5 V square wave signals with a duty-cycle of 30% to minimize DC power consumption. A coil antenna with a size of 15×15 cm^2 was made from an AWG 26 magnet wire wound around a frame resulting in an inductance of 17 μH and a high quality factor Q of 70. Following the calculation procedures for a high quality factor Q approximation in [4.31], the values of C_1 and C_2 were chosen to be 10 nF and 900 pF, respectively. The designed envelope detector includes a diode and RC networks. The diode rectifies the high voltages at the coil antenna of the class-E amplifier. The time constant of the 100-kΩ resistor and 100-pF capacitor gives a modulation frequency of 0.1 MHz that is suitable for a carrier frequency above 1 MHz. A bandpass filter was designed in the frequency bandwidth of 6 to 35 kHz to read the data from the transponder using op-

amps. The dual sensor data were then acquired and logged into a computer through a data acquisition device (NI USB-6210 DAQ, National Instruments). A system level *LabVIEW* program was used to implement the spectrum analysis mechanism. The modulated frequencies for both impedance and pH sensor was detected and recorded into a computer for data analysis.

4.3 Experiment Results

4.3.1 In Vitro Benchtop Experiment

System performances were characterized and calibrated first with benchtop experiments to insure the fidelity of our system. In this section, the dual sensor performances were demonstrated first and then the performances on unidirectional flow detection, short reflux episode recognition and repeatability were characterized. We also calibrated the dual sensor with known pH value solutions. The motion artifacts and temperature dependence effects were also characterized.

4.3.1.1 Dual Sensor Performance

The dual sensor performances were demonstrated first. We placed the dual-sensor capsule on the wall of a tube mimicking esophagus environments and flushed different liquids with known pH values of 2, 3, 5, 11, and 7 to demonstrate the performances of our dual sensors. The data of dual sensors in terms of frequency shifts were detected by the reader system and logged into a computer via a data acquisition device. Figure 4.5 shows the experiment results. The baseline frequencies for the impedance and pH sensor were obtained for around 20 sec with the frequencies of 9.51 and 25.36 kHz, respectively. The liquids with pH=2, 3, 5, 11 and 7 were flushed

through the capsule at the time stamps of 20, 55, 90, 125, and 160 sec, respectively. The experiment results showed that impedance sensor can identify each reflux episode with the modulated frequencies of 14.8, 13.9, 13.5, 13.6 and 12.5 kHz, respectively. In the mean time, pH sensor can indicate the pH levels for each reflux episode with the modulated frequencies of 29.5, 29, 27.6, 24.5, and 26.13 kHz, respectively. The impedance sensor showed good performance to identify each simulated reflux episode while the pH sensor provided the functionality to recognize the pH levels of the corresponding reflux episodes. The pH sensor readings after each episode will be transient to high frequency saturation point first and then gradually return to the base line due to the transitions of electrochemical reactions between liquids and air [4.12, 4.32].

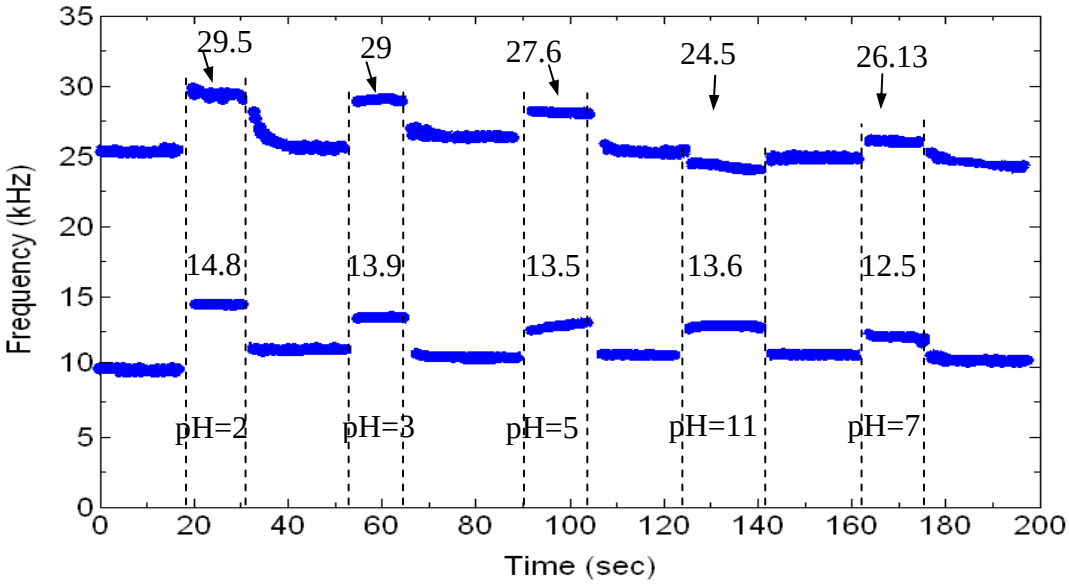

Figure 4.5 *In Vitro* dual sensor performances.

4.3.1.2 Unidirectional Detection

Due to the fact that the direction of the refluxant from the stomach is from bottom to top, and the direction of drinking liquids from the mouth is from top to bottom. We need to distinguish these two activities so the reflux episodes can be detected correctly. To demonstrate the unidirectional reflux detection, an umbrella structure made of polyimide was affixed to the sensing capsule, as shown in Figure 4.4(b). We positioned our dual sensor on the wall of a tube mimicking esophagus environments. First, we continuously flushed the liquids, from top to bottom, creating several simulated episodes like drinking liquids. Then, we created the simulated reflux episodes, from bottom to top by using U-tube principle by which the liquid was filled into the tube by adjusting the pressure level inside the tube. The capsule were immersed into the tested liquid when the pressure level inside the tube is high and the capsule was released from the liquid when the pressure level inside the tube is low, thus we can generate the reflux episodes. Figure 4.6 shows the experiment results. During the time period from 30 to 120 sec, several simulated episodes, from top to bottom, were created using the liquid with pH value of 5. The sensing electrodes of dual sensors were protected by the umbrella structure so the readings of dual sensors remained the same frequency of 9.56 kHz for impedance sensor and 25.28 kHz for pH sensor. At the time stamps of 133, 140 and 148 sec, the simulated reflux episodes from bottom to top were introduced, and the modulated frequency of 13.48 kHz for impedance sensor and 27.69 kHz for pH sensor were observed. Therefore, the unidirectional reflux detection was demonstrated with a mechanical umbrella structure. The umbrella structure was not

affixed to our sensing capsule in the *in vivo* animal experiment, since we established our experiment protocol by flushing the tested liquids from one direction to generate simulated reflux episodes. We will discuss our *in vivo* animal experiments in section 4.3.2.

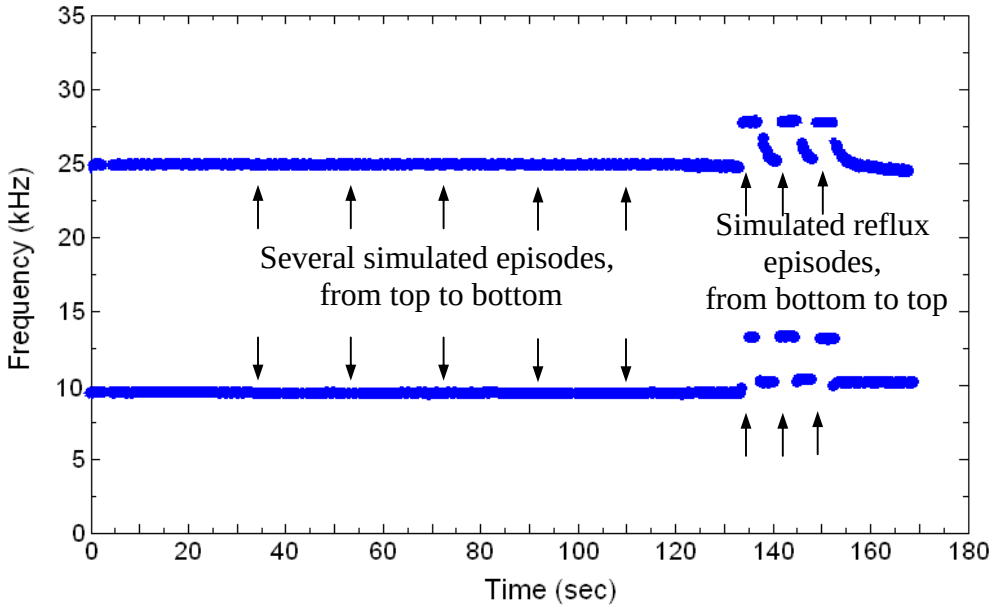

Figure 4.6 *In Vitro* unidirectional detection performances.

4.3.1.3 Short Episode and Repeatability Tests

Several reflux episodes may happen within a short period of time. To address this issue, the performances on short episodes detection were examined. In the same time, the performances on repeatability of our dual sensor were also examined using both acid and alkaline solutions with pH values of 3 and 11. We removed the umbrella structure from the capsule and placed the dual-sensor capsule together with the Bravo pH sensor on the wall of a tube mimicking esophagus environments. First we flushed

the liquid with a pH value of 3 and the experiment results were shown in Figure 4.7(a). Each short episode lasted for 5 sec and then paused for 5 sec break. Sensors were exposed to air between episodes. The Bravo readings were recorded from its external reader and our dual sensor readings were detected by the reader system and logged into a computer through the data acquisition device. In the experiment, the baseline frequencies of our dual sensors were obtained for 15 sec as a reference first with frequencies of 9.5 kHz for impedance sensor and 25.34 kHz for pH sensor. At the time stamp of 15, 25, and 35 sec, we flushed liquid with a pH value of 3 for 5 sec and then paused for 5 sec break. In the mean time, we also monitored the readings of Bravo pH sensor and recorded its pH readings. Our dual sensors responded to every simulated reflux episode immediately with modulated frequencies of 13.94 kHz for impedance sensor and 29.05 kHz for pH sensor, respectively. The commercially available Bravo pH sensor remained the same reading with the pH value of 3.2 during the test period. The experiment results showed that our dual sensor were able to generate the same modulated frequency for both impedance and pH sensor with respect to the same tested liquid with the tolerance less than ±0.1 kHz. While the frequency shifts for the episodes were more than 2 kHz, the ±0.1 kHz frequency variation is considered small. The experiment results for the alkaline solution were with the frequencies of 13.58 kHz for impedance sensor and 24.52 kHz for pH sensor with the tolerance less than ±0.1 kHz. Figure 4.7(b) showed the experiment results for the pH=11 solution. The Bravo pH sensor failed to detect the alkaline solution with a pH value of 11.

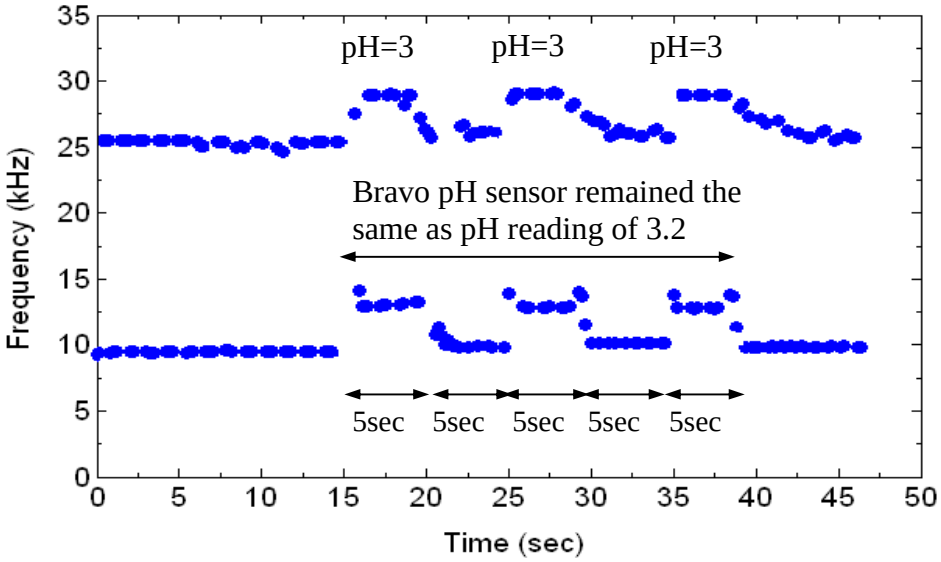

(a)

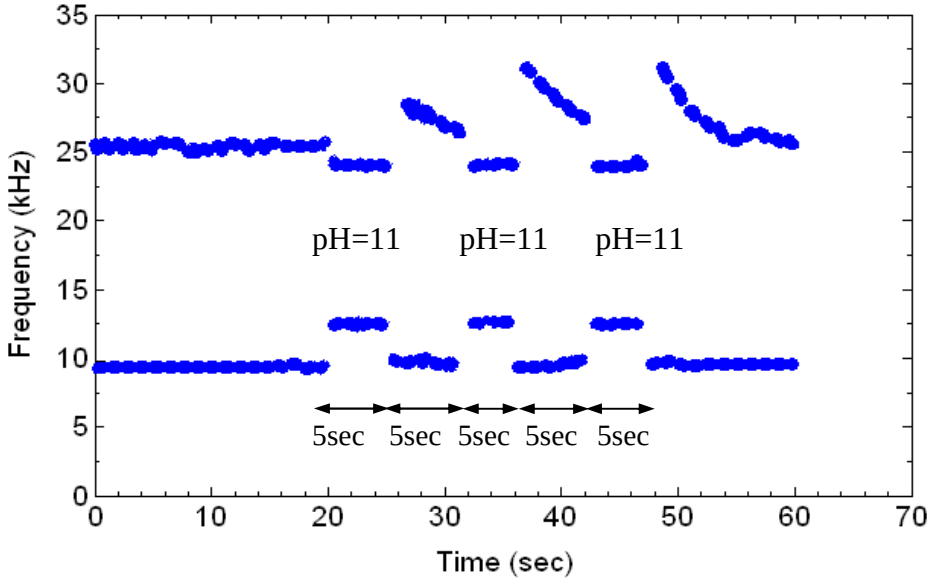

(b)

Figure 4.7 *In Vitro* simulated short reflux episode and repeatability test with (a) pH=3 solution compared with Bravo reading, and (b) pH=11 solution while Bravo indicated out of range.

.

4.3.1.4 Calibration

We calibrated the modulated frequency of our impedance sensor using solutions with different pH levels. The solutions with pH values of 2, 3, 4, 5, 6, and 7 were made by mixing the concentrated HCl acid with tap water while the solutions with pH values of 9 and 11 were made by mixing KOH with tap water. All pH readings of the solutions were verified by commercial Hanna pH meter (Hanna Instruments). The tested liquids with different pH values were dropped onto the impedance sensor and the corresponding modulated frequencies were detected by the reader. The relationship curve of modulated frequency as a function of pH values for impedance sensor was plotted in Figure 4.8(a). The modulated frequencies for pH=2, 3, 4, 5, 6, 7, 9, and 11 solutions were with the frequencies of 14.82, 13.94, 13.72, 13.5, 12.9, 12.51, 13.1, and 13.61 kHz, respectively. The working principle for impedance sensor is based on the detection of different ion concentrations of the electrode. The solution with pH=2 contained more H^+ ions than the one with pH=7, which was tap water, it gave higher modulated frequencies than the one with pH=7 in our sensing system. The alkaline solution with pH=11 also gave a higher modulated frequency than the one with pH=9. The modulated frequencies of impedance sensor for different pH solutions showed that when the solutions were more acid or alkaline, it gave higher frequencies since it contained more H^+ ions. Note that the modulated frequencies for pH=11 and pH=4 solutions were similar due to the fact that they might contains the same amount of ions in the solutions. Therefore, a pH sensor is needed to distinguish the acid and alkaline solutions

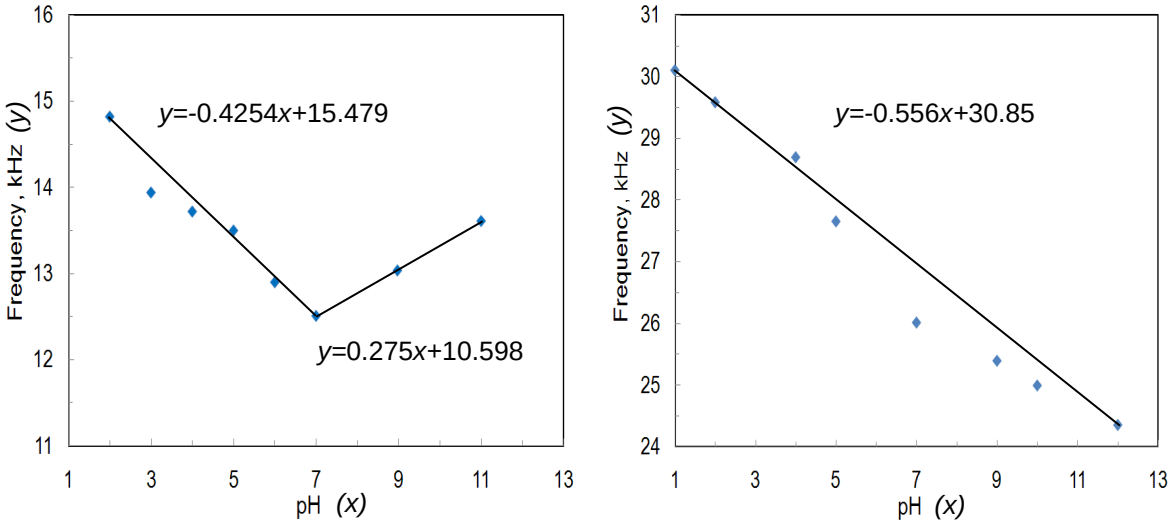

(a) (b)

Figure 4.8 Calibration of frequency readings corresponding to pH buffer solutions for (a) impedance sensor, and (b) pH sensor.

We also calibrated our pH sensor with pH buffer solutions (Cole-Parmer) so we can map the modulated frequency to pH values. The pH buffer solutions with different pH values of 1, 2, 4, 5, 7, 9, 10, and 12 were dropped on top of our pH sensing electrodes, and the corresponding modulated frequencies were detected by the reader. Therefore, the modulated frequencies corresponding to different pH values were obtained and plotted as frequencies as a function of pH values. A near-linear relationship of frequencies versus pH values was shown in Figure 4.8(b). For pH=1, 2, 4 5, 7, 9, 10, and 12 buffer solutions, the frequencies of 30.11, 29.59, 28.7, 27.66, 26.02,

25.4, 25, 24.36 kHz were measured, respectively. Thus, we can map the obtained frequency shifts to their corresponding pH values.

4.3.1.5 Motion Artifacts

We characterized our system robust performance with simulated motion artifacts mimicking physiological environments. We tested our sensing system performance in various scenarios, including the movements in *z* direction, the motion artifacts in *x*-*y* plane, and the misalignments between two antennas, defined as tilt and pan angle, α and β, respectively, as shown in Figure 4.9.

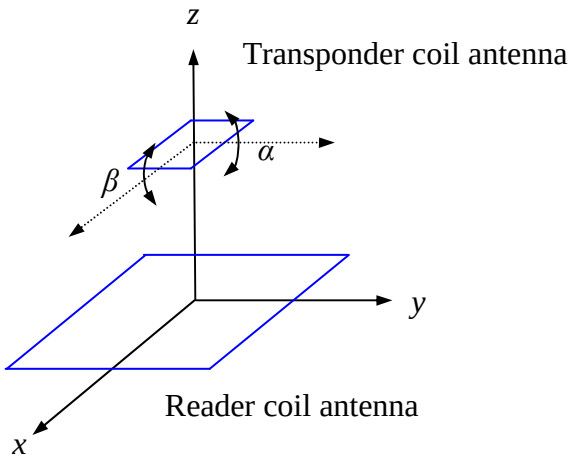

Figure 4.9 Coordinate x-, y-, and z-axis, tilt angle α, and pan angle β to characterize motion artifacts.

The coil antennas of the reader and transponder were first positioned in parallel. Then, we moved the transponder in z direction away from the reader and measured the modulated frequency at the reader. The frequency readings remained stable until the distance exceeded the maximum reading distance, which was 13 cm, in this experiment.

The signal drop was because the received energy was not enough to power the transponder circuit. The experiment results showed that the system had stable frequency readings within the reading distance, with the tolerance frequency (δf) less than ±0.1 kHz, as shown in Figure 4.10(a). Considering that the frequency shifts related to the episodes were usually more than 2 kHz, the small frequency shifts less than ±0.1 kHz was the acceptable tolerance. We also characterized the system performance by moving the transponder across the *x*-*y* plane and measured the frequency shifts. Figure 4.10(b) showed the area of our measurement results that had stable frequency readings within the area with a size of 14×14 cm^2, and the tolerance frequency (δf) less than ±0.1 kHz. The frequency readings outside this area were not stable due to the fact that the acquired energy may not be enough to power up the transponder circuit properly. For example, the frequency readings on the boundary of the reader antenna were not stable that had the frequency drops more than 4 kHz. This was due to the weak inductive coupling between two coil antennas in this area. The frequency readings of four rectangular areas outside this area indicated that the transponder can also obtain the frequency shifts with tolerance less than ±0.1 kHz, however, the size of these four rectangular areas will vary along with the distance between the reader and transponder antenna. It is suggested to position the transponder inside the area of 14×14 cm^2 to ensure stable modulated frequency is obtained. We also characterized the system performance by orientating the transponder antenna to different angles with respect to the reader antenna and measured the frequency shifts. The measurement results showed that the system had stable frequency readings with the tolerance frequency (δf) less than ±0.1 kHz except from

60 degree to 120 degree, and from 240 degree to 300 degree in both tilt and pan angles measurements, as shown in Figure 4.10(c) and (d). The frequency readings within those ranges were not correct because the coupling energy is not sufficient to power the transponder circuit due to the misalignments between the reader and transponder coil antenna.

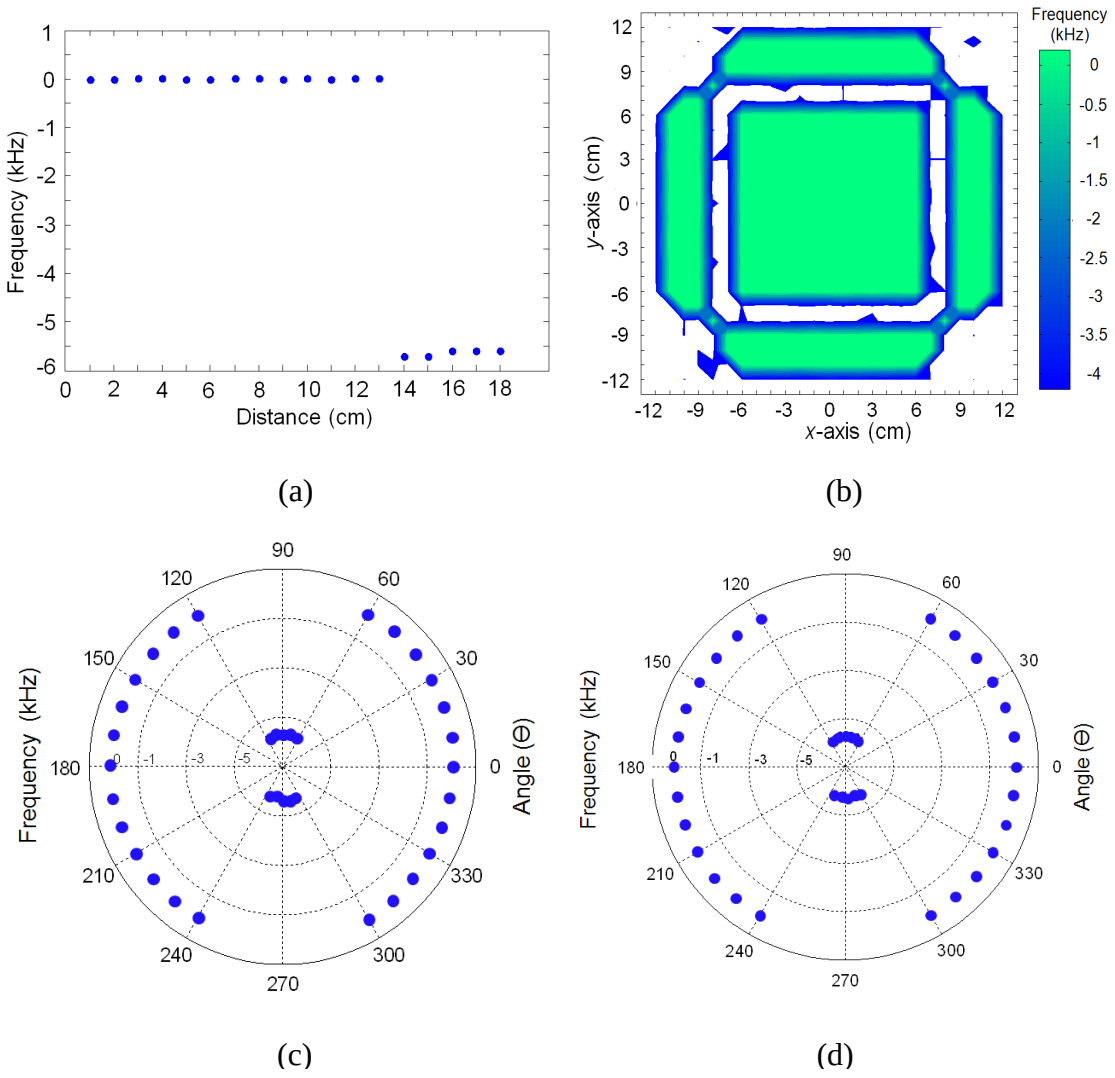

Figure 4.10 Sensor output frequencies at (a) different distance, (b) different x-y coordinate, (c) different tilt angle, and (d) different pan angle.

The experiment results demonstrated a robust sensing system with the sensor data encoded into modulated frequency. The system performance remained stable with the proper powering conditions. The system is robust enough to resist the attacks of motion artifacts across *x*-*y* plane, the distance variations in *z* direction, and the orientations in both tilt and pan angle.

4.3.1.6 Temperature Dependence

It is known that the pH levels of the solutions change as the temperatures change [4.24]. There are two types of temperature effects: one is the solution temperature effects, and the other is pH electrode temperature effect. While the solution temperature effect indicates the true pH of the solution at the new temperature, there is no need to correct or compensate for this temperature effect. However, if the temperature variations change the electrode's responses to pH readings, it is necessary to perform temperature compensation procedures to correct it. Therefore, we also measured the temperature dependence effects of the system and compared to the commercial pH sensors for possible temperature compensation processes.

We dipped Bravo pH senor together with our dual sensors into different pH buffer solutions with the pH values of 2, 4, 7, 10, and 12 under different temperature conditions ranging from 10°C, 20°C, 30°C, 40°C, and 50°C. The Bravo pH sensor malfunctioned at pH =10 and pH=12, so we used commercial Hanna pH meter as a substitute. Figure 4.11(a) shows the experiment results on the commercial pH meter at different temperatures. When the temperatures of the solutions increased, the pH solutions became more acid. Therefore, new calibration curves along with different

temperatures were plotted for the usage at different temperate ranges. It was noticed that the pH variations were smaller at pH=10 and 12 solutions when commercial Hanna pH meter was used for measurements, providing the fact that it has auto temperature compensation mechanism.

Figure 4.11(b) shows the frequency readings of our pH sensor tested with various pH buffer solutions under different temperature ranges. The experiment results also indicated that when the temperature increased, the solutions became more acid. However, the variations of pH readings are larger than those measured with commercial pH meters, especially those with pH values of 10, and 12. A temperature compensation process was required to correct this temperature effect. However, due to the size constraint of our implant, without adding more circuitry to it, a manual temperature compensation process was performed in different temperature conditions. Also, our sensor is positioned inside the body, where the body temperature is around 37˚C.

Figure 4.11(c) shows frequency readings on the impedance sensor tested with various pH buffer solutions in different temperature conditions. When the temperature increased, the frequency readings also increased on each tested pH buffer solution. This was because the ion activities were more energetic when temperatures increased. Hence, there were more ions detected by impedance sensing electrodes. The conductivity of the impedance sensor increased, therefore, the modulated frequency of our circuit also increased.

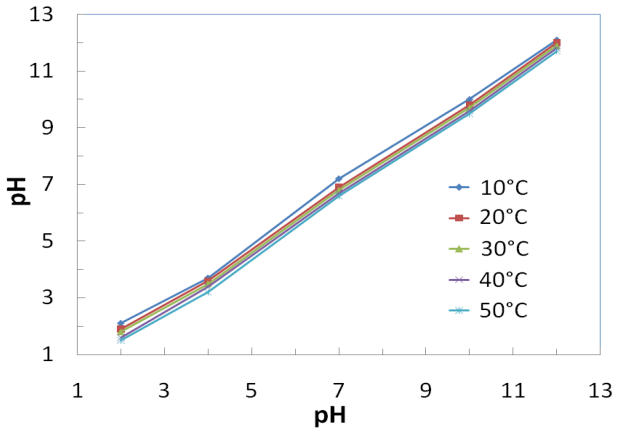

(a)

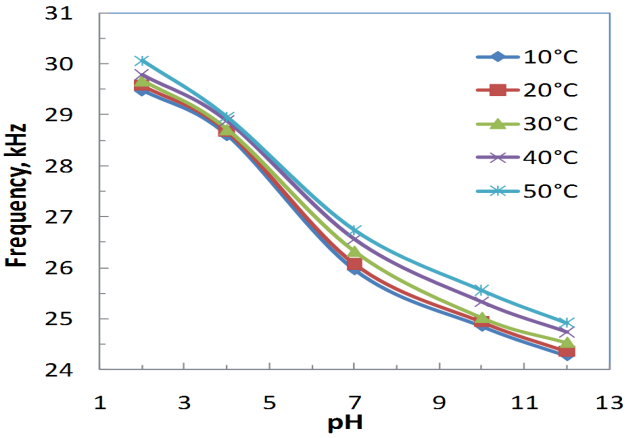

(b)

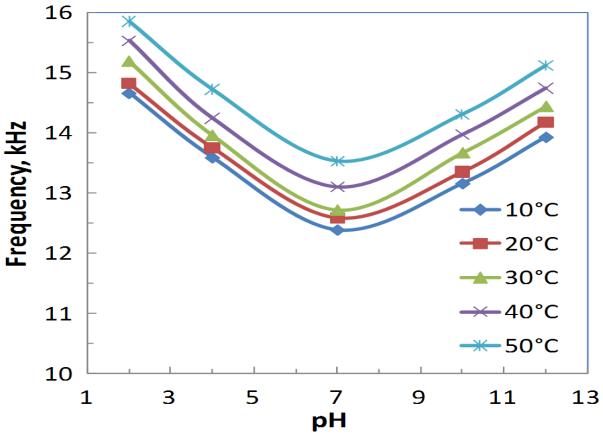

(c)

Figure 4.11 Temperature dependence effects of (a) commercial pH sensor, (b) our pH sensor, and (c) our impedance sensor.

4.3.2 In Vivo Animal Experiments

The system performances were further verified with *in vivo* animal experiments to demonstrate the abilities of our implantable sensing capsule in living biological environment. We tested our batteryless, wireless, dual sensor capsule together with the commercial wireless pH sensor and compared the performances to each other.

4.3.2.1 Animal Preparation

The animal experiments in this study were approved by Institutional Animal Care and Use Committee (IACUC). The protocol number is 20080266. The animal studies were conducted in the animal lab at the Southwestern Center for Minimally Invasive Surgery, University of Texas Southwestern. The surgeries were performed by Dr. Shou-Jiang Tang and assisted by Ms. Deborah Hogg. Three live female pigs were used in our experiments with the average weight of 105 lb/47.62 kg and average chest perimeter of 31 in/78.74 cm measuring at the level of mid-sternum. The pigs were under anesthesia for 5-8 hours. We maintained the pigs' life activities with life supporting system while the heart beat rates were measured by ECG with the reading of 96, the oxygen saturation SpO_2 were measured on ear by oximeter with the readings of 96-99%, and the blood pressure were measured by non-invasive blood pressure (NIBP) with the readings of 66/24 mmHg.

4.3.2.2 Experiment Procedure

The test solutions were flushed using a syringe pump from the mouth passing the sensor into the stomach which was cut open to drain the test solutions and also to insert the devices. A great amount of tap water was used to flush through the esophagus

to clean out the residues inside the esophagus first. The devices were positioned on the esophagus wall, few centimeters above gastroesophageal (GE) junction. An open gastrostomy was created through the anterior gastric wall in the body of the stomach. The gastroscope (Olympus GIF160) was then advanced into the stomach to remove excessive gastric fluid and content. The sensors were placed in the distal esophagus about 3 cm proximal to the GE junction under direct endoscopic guidance. The measurement of the distance was based on the markings on the shaft of endoscope.

The reader antenna was attached to the pig's skin outside the body around the chest. With the transponder in the esophagus, the motion artifact effects of live pigs were tested and the sensor signals did not fluctuate. A 16-French nasogastric (NG) tube was advanced through the mouth, larynx and into the mid esophagus for flushing various solutions. The intralumenal location of the NG tube was confirmed by endoscopic visualization. The NG tube was then secured externally to the skin by forceps.

Several solutions, including stimulated acid with the pH values of 2, 3, 5, alkaline with a pH value of 11, DI water, salt water, and tap water with the pH value of 7, and orange juice with pulp, OJ(P), without pulp, OJ(W), with the pH value of 4 were used to test the dual sensor performance. Tap water was flushed in between test solutions to clean out the residues. A surgical suction tube with continuous suction was placed inside the stomach to remove excessive solution. After each flushing of solution through the esophageal tube, intermittent suction was also applied though the accessory channel of the endoscope to remove excessive fluids in the distal esophagus right below

the implant sensors.

The implant location and fluidic activities were monitored under direct endoscopic visualization. Dual sensor signals were recorded continuously with a data acquisition device. The Bravo results were recorded discretely with the constraints of its specific sampling time. The Bravo sampling rate is one sample every 30 seconds.

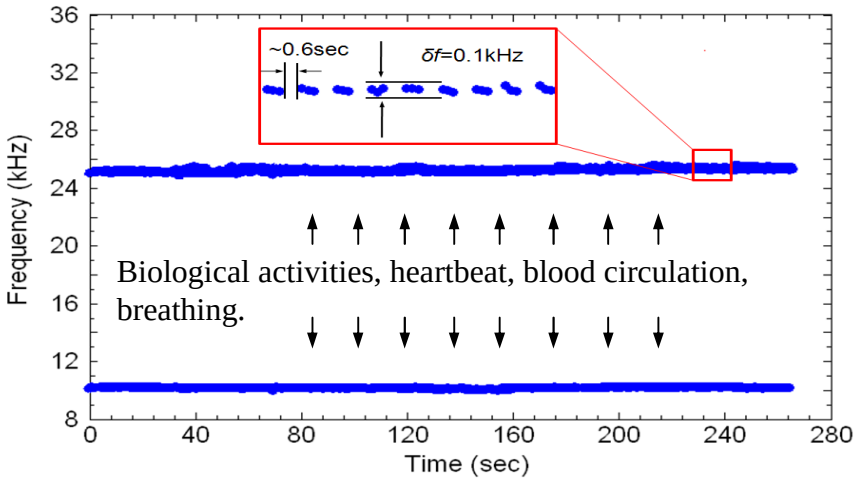

Figure 4.12 Recorded data in biological environment.

4.3.2.3 Dual Sensor Performance

Our dual sensor capsule was implanted inside the esophagus in live pig body, together with wireless Bravo pH sensing device. The RF energy generated from the reader was able to penetrate through the pig tissue to power up the sensing transponder and the sensor signals in terms of modulated frequencies from the transponder were able to be detected by the reader system. There were a lot of biological activities going on, such as heartbeats, blood circulation, breathing, and motion artifacts, and the recorded data from such living biological environment are shown in Figure 4.12. The recorded data suggested that our sensing system was robust enough to resist such

biological motion artifacts and was able to provide the stable and reliable modulated frequency signals.

The *in vivo* dual sensor performances were also tested using solutions with known pH values. The experiment results are shown in Figure 4.13. The baseline frequency of impedance sensor increased from 9.5 kHz to 10.85 kHz, compared to the one with *in vitro* benchtop experiment where the electrode was surrounded by the air. This meant that the impedance values inside the esophagus have lower impedance values than those in air. The baseline frequency for pH sensor was similar to the one with *in vitro* benchtop experiment with a frequency of 25.74 kHz. Then we flushed with different pH solutions. With the pH=2, 3, 5, 11, and 7 liquids, the pH sensor responded at 29.63, 28.82, 27.75, 24.66 and 26.12 kHz, respectively, while the impedance sensor gave modulated frequencies of 14.99, 13.95, 13.67, 13.75 and 12.61 kHz. The results were similar to those in the *in vitro* bench top experiments except that the frequency shifts for impedance sensor were smaller than those in the *in vivo* experiment. However, the frequency shifts were sufficiently clear to identify every flushing episode.

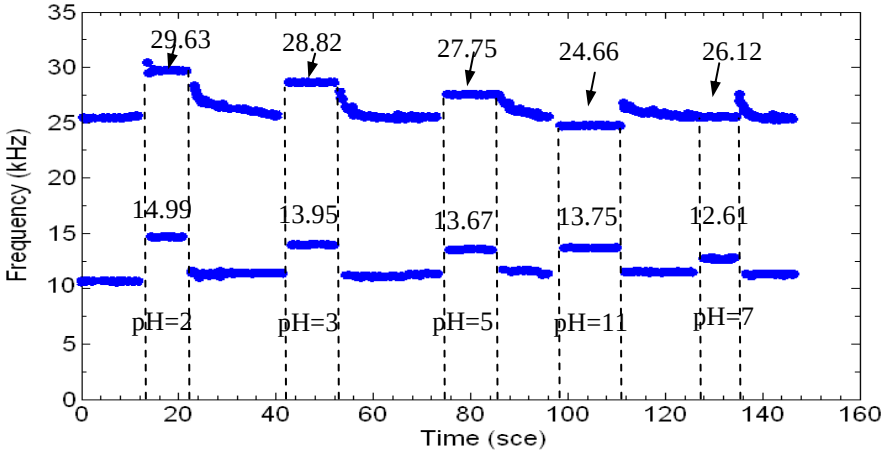

Figure 4.13 *In Vivo* dual sensor performance.

4.3.2.4 Short Episodes and Repeatability Tests

The *in vivo* dual sensor performances on short episodes detection and repeatability test were examined using both acid and alkaline solutions with pH values of 3 and 11. The Bravo readings were recorded from its external reader and our dual sensor readings were detected by the reader system and logged into a computer through the data acquisition device. The baseline frequency was obtained at the frequencies of 10.85 kHz for impedance sensor and 25.74 kHz for pH sensor, respectively. We used pH=3 solution to flush into the esophagus at the time stamps of 10, 20 and 30 sec, creating the simulated short reflux episodes, each short episode lasted for 5 sec and then paused for 5sec break. The experiment results are shown in Figure 4.14(a). There was a few second delay after flushing the liquids due to the liquid flow time from the mouth. Our dual sensors responded to every simulated reflux episode immediately with modulated frequencies of 14.06 kHz for impedance sensor and 29.15 kHz for pH sensor, respectively. The Bravo pH sensor remained the same reading with the pH value of 3.1 during the test period. Also, by examining the experiment results of those three short simulated reflux episodes, it also indicated that our dual sensor was able to generate the same modulated frequencies for both impedance and pH sensor with respect to the same tested liquid with the tolerance less than ±0.4 kHz. The experiment results for the alkaline solution with a pH value of 11 are shown in Figure 4.14(b). The pH=11 liquid was flushed into the esophagus at the time stamps of 15, 25 and 35 sec. At time stamp 33 sec, there was a small amount of alkaline liquid passed through the electrodes due to miss timing flushing. Our dual sensor responded to those simulated

reflux episodes with the modulated frequencies of 13.72 kHz for impedance sensor and 24.68 kHz for pH sensor. The Bravo pH sensor indicated error as the pH value was out of the detection range when tested with this pH=11 alkaline solution. Similarly, we also examined the repeatability performances of our dual sensors. The experiment results indicated that our dual sensors were able to generate the same modulated frequencies for both impedance and pH sensor with the tolerance less than ±0.5 kHz.

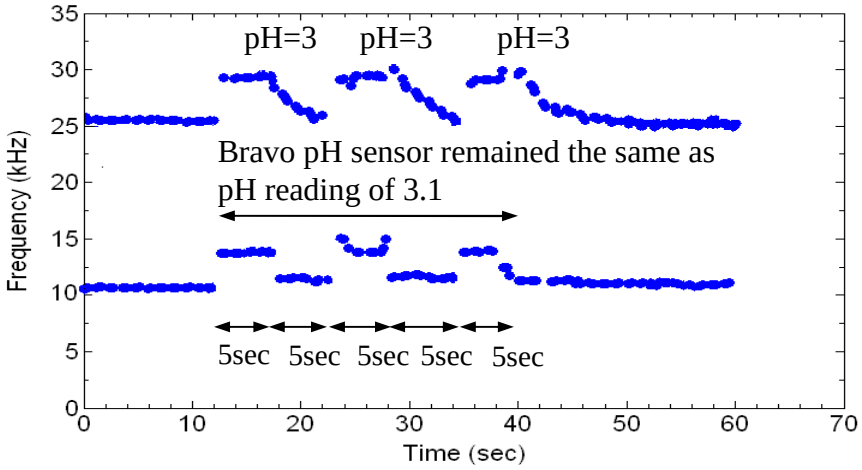

(a)

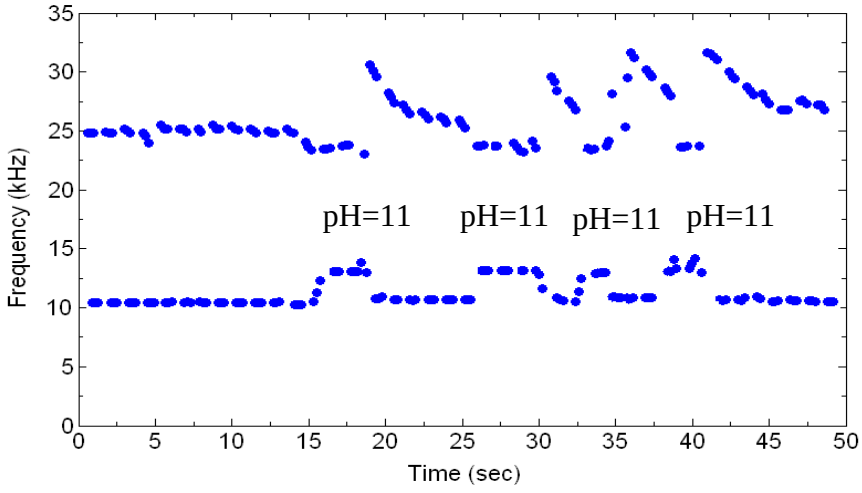

(b)

Figure 4.14 *In Vivo* simulated short reflux episode and repeatability test with (a) pH=3 solution, and (b) pH=11 solution.

4.3.2.5 *In Vivo* Experiment Results and Data Interpretation

Figure 4.15 shows the typical measurement results of our Batteryless Endoluminal Sensing Telemeter (BEST) capsule with integrated impedance and pH sensor, and compars to the performances of the Bravo pH sensor capsule in the esophagus. The frequency readings of the pH sensors were converted to the pH readings using the calibration curve and the impedance sensor data were presented as the modulated frequency shifts. The Bravo readings were recorded discretely along with the simulated reflux episodes to verify the pH readings measured by our pH sensor in the esophagus. The experiment results showed good correlation on the pH readings between our pH sensor and Bravo pH sensor with differences less than ±0.4. However, Bravo failed to indicate the correct pH value for the alkaline solution with a pH value of 11. The reading on the Bravo indicated an error symbol “HI” while our pH sensor indicated a pH value of 10.8. It was also noted that the readings of our pH sensors were measured continuously along with each simulated reflux episode. After each episode, the readings of our pH sensor gradually came back to its original state, indicating the period of reflux episodes as well, while the readings of Bravo pH sensor remained the same due to the constraint of its low data sampling rate.

Between flushing events, the frequencies from the impedance sensor dropped and pH sensor gradually decreased when the liquid left the electrode. However, the frequencies did not go back to the baseline frequency because there were still some liquid residues left on the electrodes. The frequency drop amounts were also not the same after every flushing due to unpredictable amounts of residue that might stay on the

electrodes. The frequency drops however were sufficiently clear to identify every flushing episode. The phenomena of liquid residue left on the electrode were also observed in the pH values of Bravo. After the liquid flushing events, tap water flushing was not able to bring the pH values back to 7. This indicated that there was a phenomenon of residue left on both devices when doing *in vivo* animal experiment.

The measurement results of our impedance sensor for the episodes with the pH values of 2, 3, and 5 were with the frequencies of 14.99, 14.08, and 13.51 kHz, respectively. The experiment results showed that when the tested solutions were more acid, which contained more H^+ ions in the solutions, the modulated frequency of our impedance sensor were higher. To demonstrate that the impedance sensor is sensitive to the ion concentrations, we used salt water, that contained a lot of ions, and DI water, that contained almost zero ions in the solution, to do the experiment. The modulated frequency of impedance sensors were with the values of 15.89 and 10.85 kHz, for salt water and DI water, respectively. The salt water solution which has low impedance generated a high modulated frequency; however, it did not significantly change the pH values therefore cannot be detected from the pH sensor. Also, when the tap water with a pH value of 7 was flushed into the esophagus twice to serve as multiple reflux episodes, the readings of Bravo pH sensor did not indicate these events while our impedance sensor indicated these two episodes with the frequency shifts of 12.51 and 12.35 kHz, respectively.

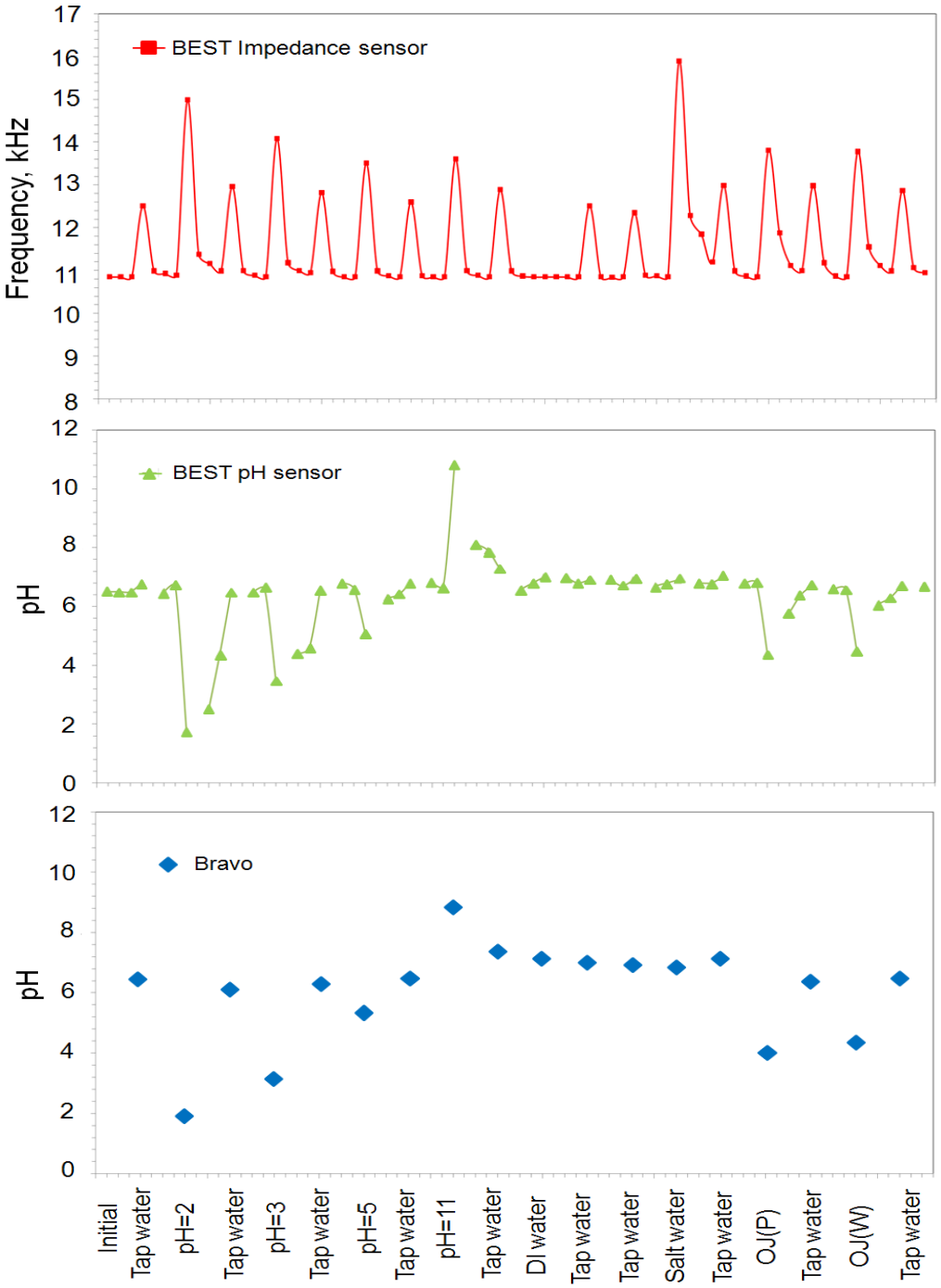

Figure 4.15 *In vivo* animal experiment results.

Two liquid juices, orange juice with pulp, OJ(P), and orange juice without pulp, OJ(W), with the measured pH values of 4.1 and 4.2, were also used to test the sensor performances. The purpose of using these two liquids was to examine whether the pulp materials will affect our measurement results or not. The experiment results showed that the modulated frequencies of our impedance sensor were with the frequencies of 13.81 and 13.78 kHz for OJ(P) and OJ(W), respectively. The pH readings of our pH sensor were also around the pH values of 4 for both OJ(P) and OJ(W). The experiment results suggested that the pulp materials didn't make differences on the sensor performances.

In Figure 4.16(a), the pH readings for Bravo pH sensor and our pH sensor are plotted as a function of each tested episode. It indicats that our pH sensor readings had good agreement with the commercial Bravo pH sensor with pH value differences less than ±0.4 in most of the cases. However, our pH sensor can indicate the alkaline solution with a pH value of 10.8 while Bravo pH sensor gave the error readings. Furthermore, we used the impedance calibration curve to convert the tested simulated episodes to pH values. The purpose of doing this was to find out the correlation between the pH values and the impedance sensor readings. In Figure 4.16(b), it shows that the impedance sensor can also indicate pH values of the test liquids. However, for the solution with a pH value of 11, the impedance sensor readings might be confusing. It could be converted into pH=4 or pH=11. The modulated frequencies for both cases were similar because they might contain similar amount of the ion in the solutions. Furthermore, the impedance sensor gave the wrong pH readings on salt water and DI water. These again pointed out the importance of the integration of both pH sensor and

impedance sensor into a single sensing device.

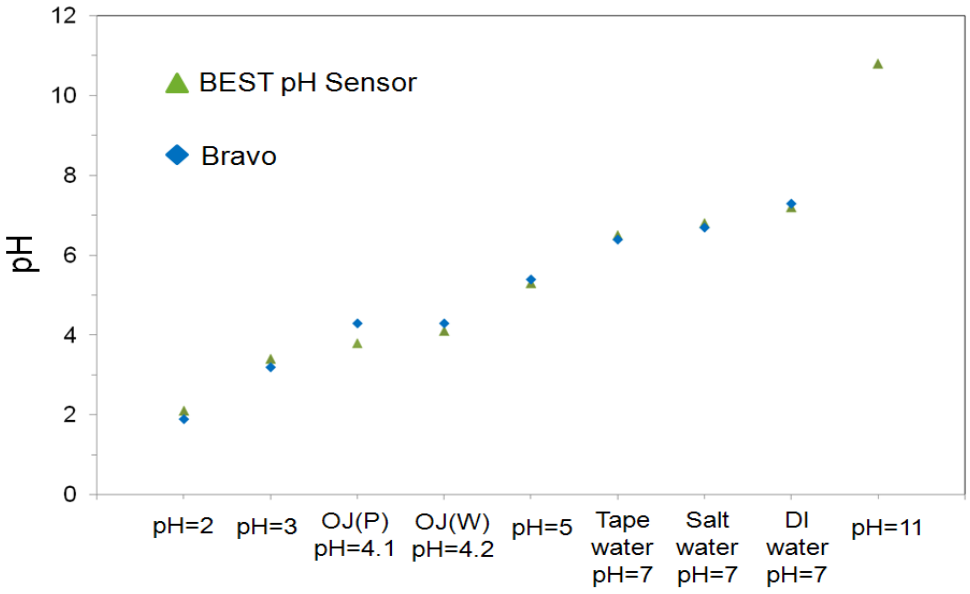

(a)

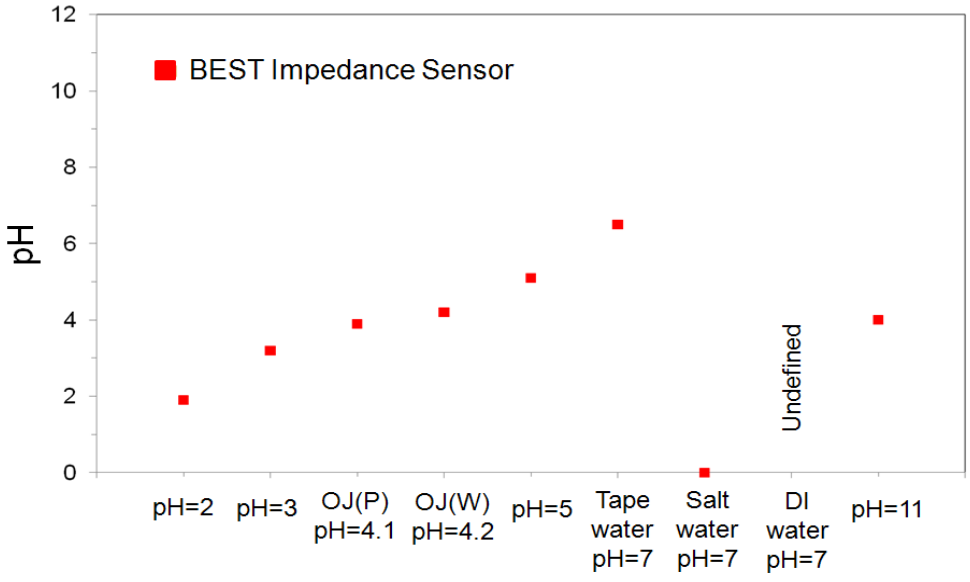

(b)

Figure 4.16 pH values of the events (a) pH sensor, and (b) impedance sensor.

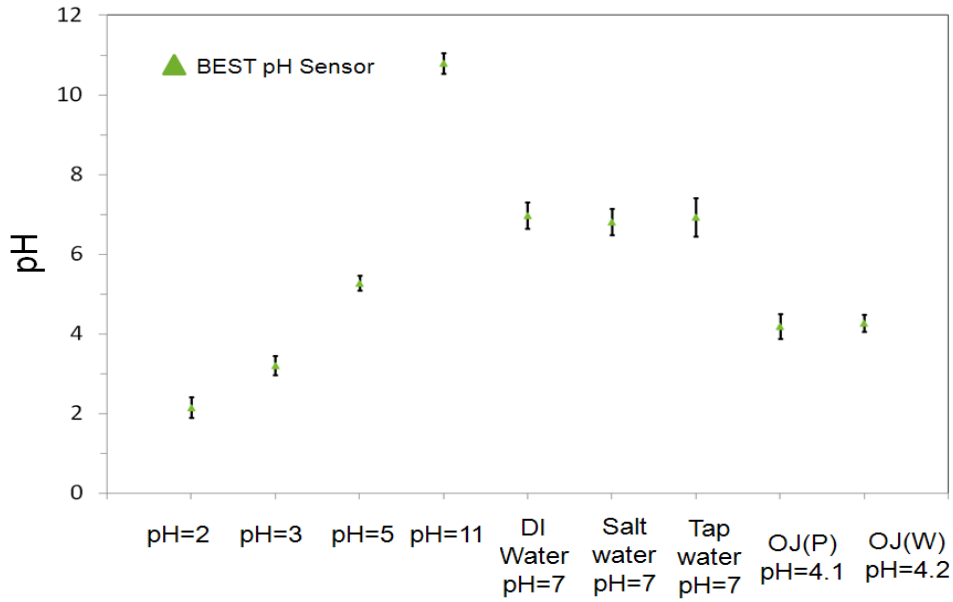

(a)

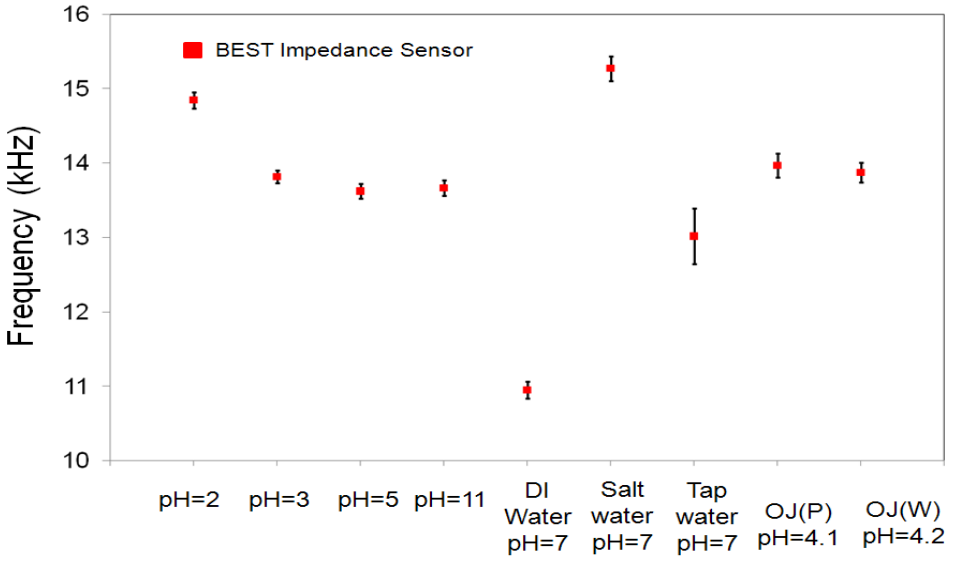

(b)

Figure 4.17 Statistical data analysis of (a) pH sensor and (b) impedance sensor.

4.3.2.6 Data Analysis

We carried out the experiments on three different days and each day we performed the experiments on one pig to validate the system performances. We obtained 5 sets of data and performed the statistic data analysis to verify the reliability of our sensing system. First, we calculated the mean values from the readings of BEST pH sensor and BEST impedance sensor for each tested solutions and calculated the corresponding standard deviations. Figure 4.17 showed the analysis results. For BEST impedance sensor, we obtained the standard deviation less than 0.16 kHz among all the tested liquids except for tap water with the standard deviation values of 0.37 kHz. For BEST pH sensor, we obtained less than 0.33 on the pH value variation, except for tap water with the pH value variation of 0.48. The reason that tap water had larger standard deviation was because it was used to clean out the residue. Our experiment results indicated that the reliability of our dual sensors is pretty good with the standard deviations less than the frequency shift of 0.16 kHz for impedance sensor, and the pH value of 0.33 for pH sensor in most of the cases.

4.4 Summary

An implantable, batteryless, and wireless capsule integrated with impedance and pH sensors for gastroesophageal reflux monitoring has been designed, fabricated and validated. The approach on the integration of impedance and pH sensors provides a complete solution for gastroesophageal reflux monitoring. Our wireless device does not require a battery so there is no time limit for monitoring compared to battery powered wireless devices. The device was tested in live pigs demonstrating the feasibility and

accuracy of detecting various simulated reflux episodes. The read range was demonstrated with the reader at a 13-cm distance from the transponder in a beaker and through the pigs' body with an average chest perimeter of 78.74 cm. The signals kept the same accuracy even under the attacks of motion artifacts. Our dual sensor can identify the short reflux episode while the commercial pH sensor gave the same reading during the short test period. The experiment results showed comparable performance to the commercial wireless pH sensors with our pH sensor. Furthermore, the impedance sensing method was able to detect non-acid reflux episodes as it could distinguish air, acid, alkaline and salt solutions from water. The experiment results showed that our dual sensor can detect both acid and non-acid reflux episodes providing both impedance and pH sensor information simultaneously for GERD monitoring.

CHAPTER 5

CONCLUSIONS AND FUTURE WORK

5.1 Conclusions

In this dissertation, a batteryless, wireless sensing platform was investigated. The sensing platform consists of a sensing device and a remote reader system. The remote reader radiates the RF energy to power up the sensing device and records the data from it. The sensing device can process either resistive, capacitive, or voltage type of sensor inputs and encode into frequency shifts without the need of battery in it. The sensing platform is robust enough to provide the immunity to the motion artifacts suitable for physiological environment usage. The system performances were demonstrated in two medical applications, one is external and the other one is internal. A pressure sensor array that can monitor the pressure profile for pressure sore development monitoring is for external application and an implantable integrated impedance and pH sensor capsule for gastroesophageal reflux monitoring is for internal application.

For external physiological sensing application, a batteryless wireless piezoresistive pressure sensing system was presented for applications of monitoring pressure sore development in paralyzed patients who might be in beds or in wheelchairs. A piezoresistive force sensing resistor was chosen as the sensing element

due to its good sensitivity. The mechanical design knowledge was exercised first to convert the force signals, measured by the force sensing resistors, into pressure data. The sensing elements were then arranged in an array format with spatial design consideration to monitor the pressure distribution profile accordingly. The sensors were able to identify high pressure points dynamically. Stability tests of the sensor were carried out for long-term monitoring purposes. The experimental results indicated that the drifting of reading was smaller than the readings of high-pressure indications so the sensors can be used for a long period of time. Then the electrical design knowledge was employed for sensor interfacing circuit. The sensing device includes an energy harvesting circuit, a force sensing resistor, a resistance-to-frequency converter, and an antenna. The reader provides power to the device remotely and measures the sensor values in terms of frequency shift simultaneously. The experimental results showed good linearity, sensitivity, and resolution in the tested pressure range.

For internal physiological sensing application, an implantable, batteryless, and wireless capsule integrated with impedance and pH sensors for gastroesophageal reflux monitoring has been designed, fabricated and validated. The prototype of dual sensor transponder was implanted into esophagus, wirelessly transmitting the modulated sensor signals to the external reader. The impedance sensor picked up every simulated reflux episode and the pH sensor recognized the pH readings of each reflux episode. The wireless device does not require a battery so there is no time limit for monitoring, superior to the commercial wireless pH sensors that are limited by battery life time. The device was tested in live pigs and demonstrated the feasibility and accuracy of detecting

the simulated reflux episodes in real physiological environment. The signals kept the same accuracy without being affected by motion artifacts. The experiment results showed superior performance than the commercial wireless pH sensors with our pH sensor. Furthermore, the impedance sensing method was able to detect non-acid reflux episodes as it could distinguish air, acid, alkaline and salt solutions from water. Our dual sensor responded to the short simulated reflux episodes immediately while the commercial wireless pH sensor remained the same reading due to the slow sampling rate of the device. Our batteryless, wireless and integrated sensor capsule system can detect acid and nonacid reflux episodes providing both impedance and pH information simultaneously for GERD monitoring.

5.2 Future Work

In this research, we used time-multiplexing scheme to coordinate multiple sensor input data. Our system was designed to be simple using a time switch mechanism to switch between sensor input data. The purpose of this was to minimize the size of device and to reduce the power consumption with less active components added into the circuit, especially when our sensing device was designed to be implantable. However, by using time-multiplexing scheme, each sensor was shared one time slot within every scanning cycle. Some data points measured from the sensor were lost when not in that time slot. Thus, we would like to lay out the other topology for the integration of multiple sensors as future work when transistor level integrated circuit design tool is used to realize the transponder circuit in a smaller scale.

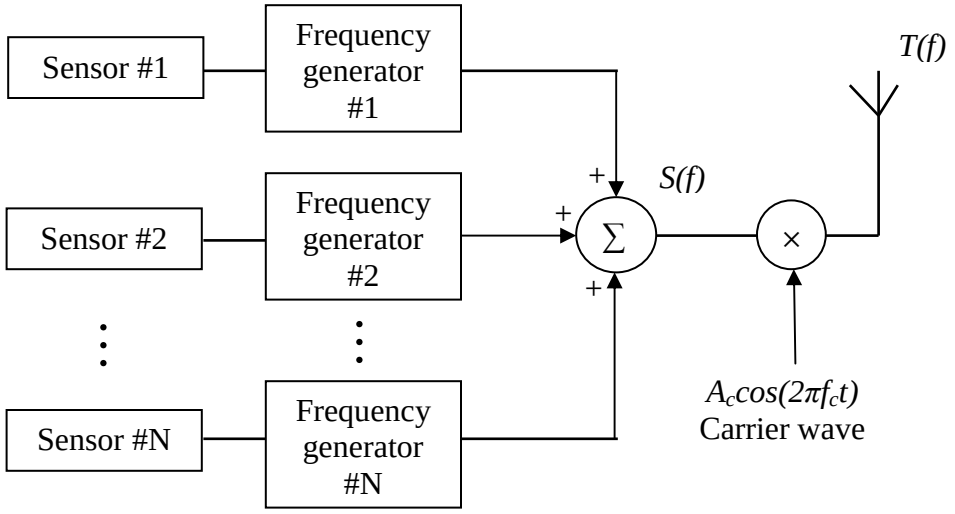

(a)

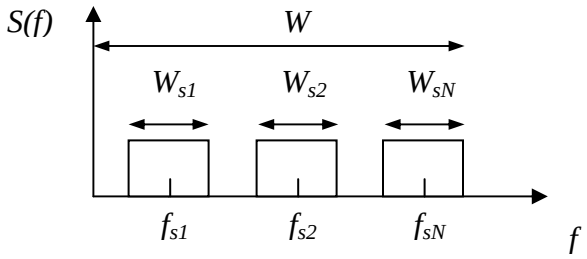

(b)

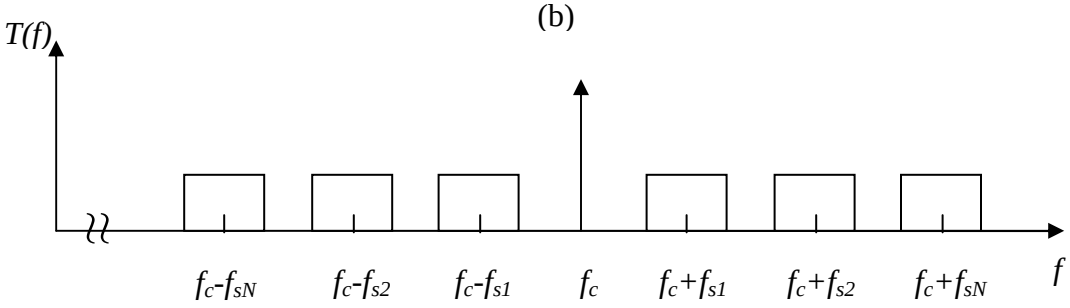

(c)

Figure 5.1 Multiple sensor integration topology. (a) Transmitter block diagram. (b) Spectrum of multiple sensors. (c) Spectrum of transmitted sensor signals.

Figure 5.1(a) shows the transmitter block diagram on the topology for multiple sensor integration. The output frequencies from frequency generators are modulated by sensors first. They are designed to have different modulated frequencies of, f_{s1}, f_{s2}, and f_{sN}, with bandwidths of W_{s1}, W_{s2}, and W_{sN}, correspondingly, and they are not overlapped to each other. In frequency domain, the frequency spectrums of those sensors can be added up and are considered as a baseband signal with bandwidth of W, as shown in Figure 5.2(b). Then, the baseband signal spectrum, $S(f)$, is multiplied by the carrier wave $A_c cos(2\pi f_c t)$ with carrier frequency, f_c, and the modulated sensor signal is ready to be transmitted with the transmitted spectrum $T(f)$, as shown in Figure 5.1(c). On the receiver end, we need to demodulate the received signal and extract the sensor signals correctly. Figure 5.2 shows the receiver block diagram. The received signal with the spectrum $R(f)$ is first multiplied by the carrier wave frequency. Then the band pass filter with the center frequencies, f_{s1}, f_{s2}, and f_{sN} are designed with the bandwidth of W to extract the sensor signal, correspondingly.

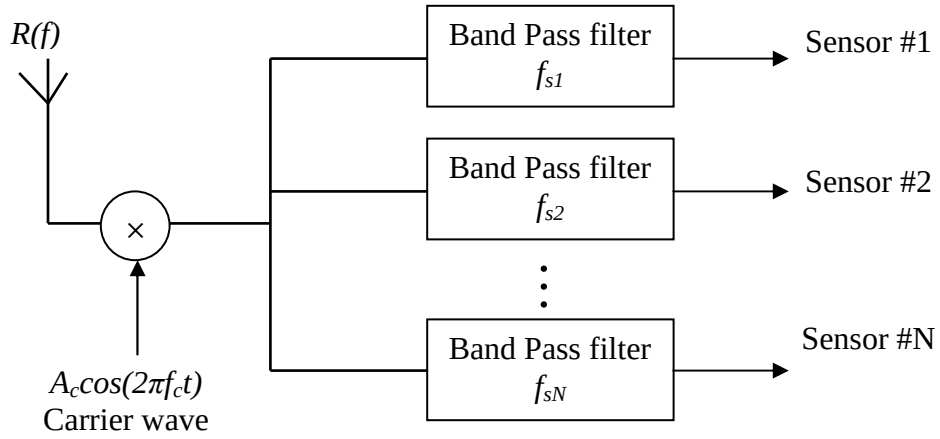

Figure 5.2 Receiver block diagram to extract multiple sensor signals.

In Figure 5.1 and Figure 5.2, the main topology of the transceiver for multiple sensor integration is depicted. The future work should focus on implementing the topology to demonstrate the capability of this architecture for system integration.

The miniaturization of the circuitry into a single chip would also be the future work and it can be done either by using a custom ASIC chip or transistor level integrated circuit design. The small size of the chip allows the integration of multiple sensors without adding extra size on the transponder while using board level circuit design has its limitations. Furthermore, with digital circuit design, the sensor data could contain identification information for better tracking of the information.

APPENDIX A

A SYSTEMATIC APPROACH TO OPTIMIZE THE POWERING EFFICIENCY OF INDUCTIVE LINKS FOR BIOMEDICAL APPLICATIONS

A.1 Introduction

Passive RFID technology that uses the inductive links for RF powering and data transmission between the reader and transponder realizes a batteryless, and wireless communication system [A.1]. Moreover, to supply energy to implanted devices, wireless electromagnetic energy transfer is an effective and proven technique [A.2-A.4]. Low-frequency electromagnetic energy transfer is currently used in cochlear implants [A.5-A.6], radio-frequency identification (RFID) implants [A.7], retinal prosthetics [A.8], and neurostimulators [A.9-A.11], etc. However, how to improve the powering efficiency, especially for implantable biomedical systems, has been an important issue for researchers to solve [A.12, A.13]. For small implanted applications, where volume limitations constraint the size of the receive coil, the practical range of energy transfer is limited to a few centimeters. So, researchers have worked on design optimization and invention of new techniques to increase the read distance and coupling efficiency. However, the optimization approaches were either confined to some specific constraints [A.14-A.20], or used consecutive planning methods to optimize the system performances [A.21-A.23]. Therefore, in this section, a systematic approach was attempted to optimize the powering efficiency based on one governing equation that will fine tune all the parameters to optimize the system performances. Theoretical assumptions and mathematical formula derivations were performed first and followed by the experiment results to verify the correctness and completeness of the theoretical

modeling approaches.

A.2 Equivalent Circuit

Figure A.1 shows the equivalent circuit of inductive coupling resonant circuit. It consists of two coil antennas with the inductance values of L_1 and L_2, an AC source V_{in} with specified operating frequency, f_0, and two tuning capacitors, C_1 and C_2, calculated from the formula of resonant frequency

$$f_0 = \frac{1}{2\pi\sqrt{LC}} \tag{A.1}$$

M represents the mutual inductance between two coil antennas while it can be calculated by

$$M = k\sqrt{L_1 \cdot L_2} \tag{A.2}$$

where k is the coupling coefficient that varies between $0 \le k \le 1$.

k=0 means full decoupling, that might due to great distance or magnetic shielding, and k=1 means total coupling while both coils are subject to the same magnetic flux.

Equivalent series resistors (ESR), R_1 and R_2, account for the resistance values of the inductors for reader and transponder, respectively, and R_{ACload} represents the load impedance of the transponder circuit.

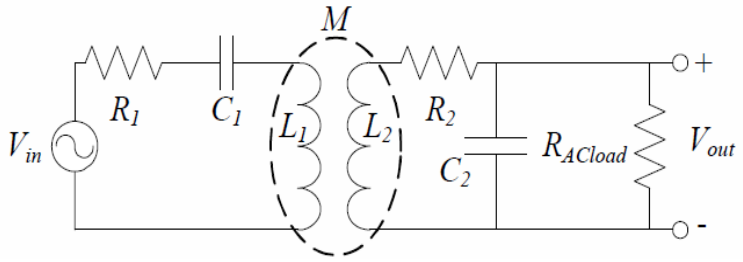

Figure A.1 Equivalent circuit of inductive coupling resonant circuit.

A.3 Formula Derivation

To optimize the coupling coefficient of the resonant circuit, we define the coupling efficiency, η_c, as the ratio of power received by R_{ACload} versus the power drawn from the input source V_{in}.

$$\eta_C = \frac{P_{out}}{P_{Vin}} = \frac{\dfrac{V_{out}^2}{R_{ACload}\sqrt{2}}}{\dfrac{V_{in}^2}{R_1\sqrt{2}}} = \left(\frac{V_{out}}{V_{in}}\right)^2 \frac{R_1}{R_{ACload}} \tag{A.3}$$

where the voltage gain expression from V_{in} to V_{out} can be expressed as [A.24, A.25]

$$A_V = \frac{V_{out}}{V_{in}} = \frac{\omega_0^2 M L_2}{R_1 R_2 + R_1 \dfrac{(\omega_0 L_2)^2}{R_{ACload}} + (\omega_0 M)^2} \tag{A.4}$$

and angular frequency $\omega_0 = 2\pi f_0$.

By plugging (A.4) into (A.3), an expression for η_c can be derived as

$$\eta_C = \left(\frac{\omega_0^2 M L_2}{R_1 R_2 + R_1 \dfrac{(\omega_0 L_2)^2}{R_{ACload}} + (\omega_0 M)^2} \right)^2 \frac{R_1}{R_{ACload}} \tag{A.5}$$

Knowing the facts that the values of R_1, R_2, L_2, and mutual inductance, M, will vary while the number of the turns of the coil antenna change; we need to find the expressions to describe their relationships. In the literatures [A.21-A.23, A.26], the equations to describe the relations between number of turns and the parameters, such as self inductance, L, mutual inductance, M, and equivalent series resistance, R, can be

found as

$$L = N^2 L_0 \tag{A.6}$$

$$M = \frac{\mu\pi N_1 N_2 r_{Tag}^2 r_R^2}{2\sqrt{\left(r_R^2 + x^2\right)^3}} \tag{A.7}$$

$$R = NR_0 \tag{A.8}$$

where N represents the number of turns of the coil antenna; L_0 and R_0 represent the single-turn resistance and inductance; r_R and r_{Tag} represent the radii of reader and tag coil antennas; and x represents the distance between two antennas. Using (A.6), (A.7), and (A.8) in tandem with (A.5), the coupling efficiency formula can be derived as

$$\eta_C = \left(\frac{\omega_0^2 \frac{\mu\pi N_1 N_2 r_{Tag}^2 r_R^2}{2\sqrt{\left(r_R^2 + x^2\right)^3}} N_2^2 L_{20}}{N_1 R_{10} N_2 R_{20} + N_1 R_{10} \frac{\left(\omega_0 N_2^2 L_{20}\right)^2}{R_{ACload}} + \left(\omega_0 \frac{\mu\pi N_1 N_2 r_{Tag}^2 r_R^2}{2\sqrt{\left(r_R^2 + x^2\right)^3}} \right)^2} \right)^2 \frac{N_1 R_{10}}{R_{ACload}} \tag{A.9}$$

This formula contains the parameters, such as N_1 and N_2, which give us some degrees of freedom to perform the optimization strategy. Therefore, we took the derivative of η_c with respect to N_1 and N_2, and set the equations equal to zero to find their optimal values. By setting $\frac{\partial \eta_c}{\partial N_2} = 0$, and solving for N_2, we can get

$$N_2 = \sqrt[3]{\frac{2R_{20}R_{ACload}}{\omega_0^2 L_{20}^2}} \tag{A.10}$$

Similarly, by setting $\frac{\partial \eta_c}{\partial N_1} = 0$, and solving for N_1, we can get

$$N_1 = \frac{R_{10} R_{20} N_2 + R_{10} \frac{(\omega_0 N_2 L_{20})^2}{R_{ACload}}}{\left(\omega_0 \frac{\mu\pi N_2 r_{Tag}^2 r_R^2}{2\left(r_R^2 + x^2\right)^{3/2}} \right)^2} \quad \text{(A.11)}$$

(A.10) and (A.11) describe the behaviors about number of turns of the coil antennas on the transponder and reader, respectively.

First, we explored the theoretical plot of N_2 based on equation (A.10). However, to begin with the optimization process, we need to fix some parameters first. Since the operating frequency is usually defined by the regulation, we fixed the frequency at 1.34 MHz first; due to the fact that the recommended maximum permissible exposure (MPE) of magnetic field is the highest in the frequency ranges from 1.34 MHz to 30 MHz [A.27]. Then, the size of the transponder coil antenna was determined by the size of our PCB board design. The area was around 4.5 cm^2, so we can calculate the transponder radius with the value of 1.2 cm. We made the coil antenna by using the AWG 34 magnet wire. Then, we made a single-turn circular shape coil antenna with the radius 1.2 cm and used the impedance meter (HP 4192AF) to measure its parameters, R_{20}, L_{20}, and the Quality factor (Q) with the values of 0.262 Ω, 0.283 µH, and 8.8, respectively. With those parameters, we were ready to explore the theoretical plot of N_2 as a function of different R_{ACload} value.

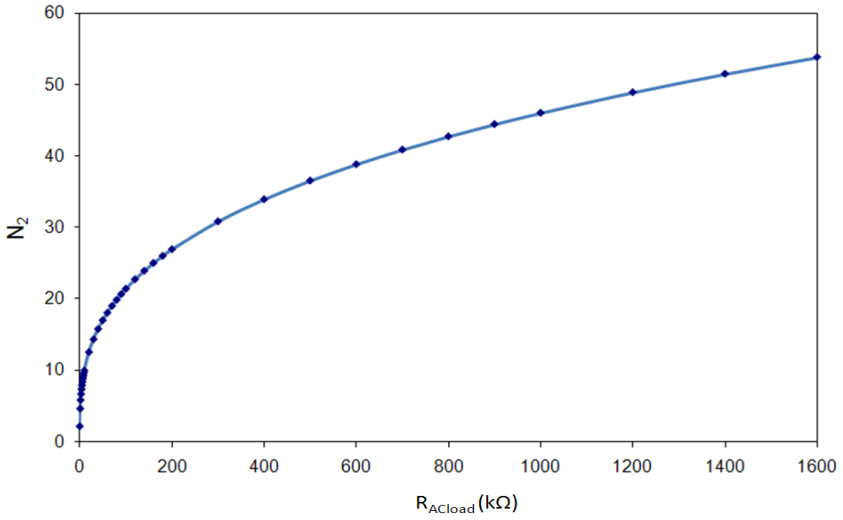

Figure A.2 Theoretical plot on N_2 as a function of R_{ACload}.

Figure A.2 shows the theoretical plot on the number of turns, N_2, as a function of R_{ACload}. When the load impedance R_{ACload} increases, the required number of turns, N_2, also needs to be increased, therefore, more voltage can be induced in the transponder. The induced voltage, V, in the transponder antenna coil can be found as

$$V = -N \frac{d\Phi}{dt} \tag{A.12}$$

where Φ is the total magnetic flux through surface of transponder antenna coil.

When the R_{ACload} were with the resistance values of 100, 200, 400, 600, 800, 1000, 1200, 1400, and 1600 kΩ, the required numbers of turns, N_2, were with the values of 21, 27, 34, 39, 43, 46, 49, 51, and 54, respectively. Note that the values of N_2 were round into the closest integer.

Then, we would like to explore the theoretical plot of N_1 based on the equation (A.11). Also, equation (A.13) can be obtained from (A.11) under the assumption when $x >> r_R$,

$$N_1 = \frac{R_{10} R_{20} N_2 + R_{10} \frac{(\omega_0 N_2 L_{20})^2}{R_{ACload}}}{\left(\omega_0 \frac{\mu\pi N_2 r_{Tag}^2 r_R^2}{2x^6} \right)^2}, \; x >> r_R \qquad \text{(A.13)}$$

To explore the theoretical plot of N_1, we had L_{20}=0.283 µH, R_{20}=0.262 Ω, Q=8.8 and r_{Tag}=1.2 cm. Then, we chose a pair of R_{ACload} and N_2 with the values of 100 kΩ and 21 earlier from tag. To proceed with the verification process, we fixed the distance between the reader and transponder at the distance of 10 cm. Then, a circular shape coil antenna with the radius of 1cm was made from AWG 26 magnet wire. The measured equivalent series resistance of single-turn resistor, R_{10}, was with the value of 0.051 Ω. Note that the resistance values for different size of coil antennas will be proportional to their radii. Now, we can plot the theoretical plot of N_1 as a function of different radii, r_R. First, we plotted equation (A.11) and the curve was shown in Figure A.3.

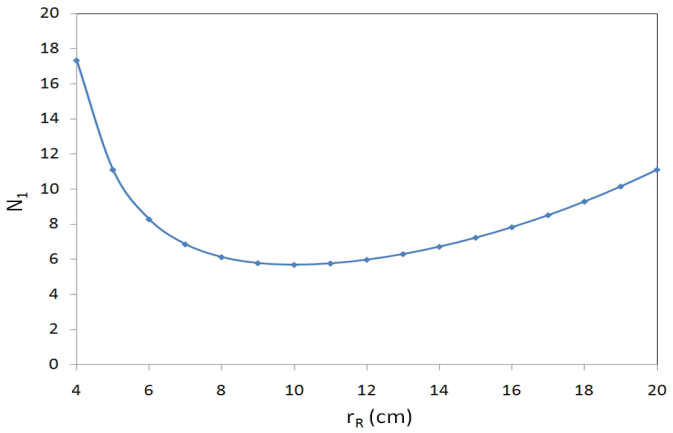

Figure A.3 Theoretical plot on N_1 as a function of r_R.

We also plotted equation (A.13) and obtained the curve of N_1 as a function of different radii of reader coil antennas, as shown in Figure A.4.

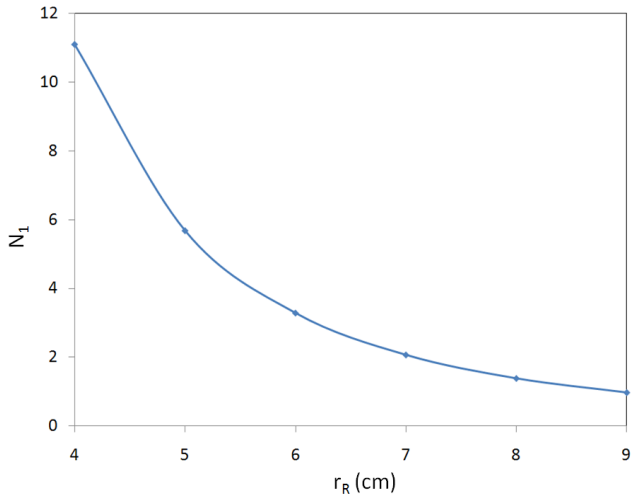

Figure A.4 Theoretical plot on N_1 as a function of r_R under the assumption when $x >> r_R$.

A.4 Experiment Results

A.4.1 Measured Parameters Approach

To verify the theoretical plot, the experiments were performed on the test bench circuit mentioned in Figure A.1. N_1 curves were examined first in the following procedures. First, the reader and transponder coil antennas were positioned in parallel apart from each other with a distance of 10 cm. The resonant frequency, f_0, was set to the frequency of 1.34 MHz, the parameters on the transponder, such as r_{Tag}, R_{ACload}, N_2, L_2, and the calculated tuning capacitor, C_2, were with the values of 1.2 cm, 100 kΩ, 22, 21.45 µH, and 700 pF, respectively. Then, a combination of various numbers of turns coil antennas were made on different sizes of the reader frames with the radii of 4, 5, 6, 7, 8, and 9 cm. The inductance values of each combination were measured by impedance meter and the values of tuning capacitor, C_1, were calculated correspondingly. Then, the oscilloscope was used to measure the output voltage across

the R_{ACload} to find out which combination gave the optimal output voltage.

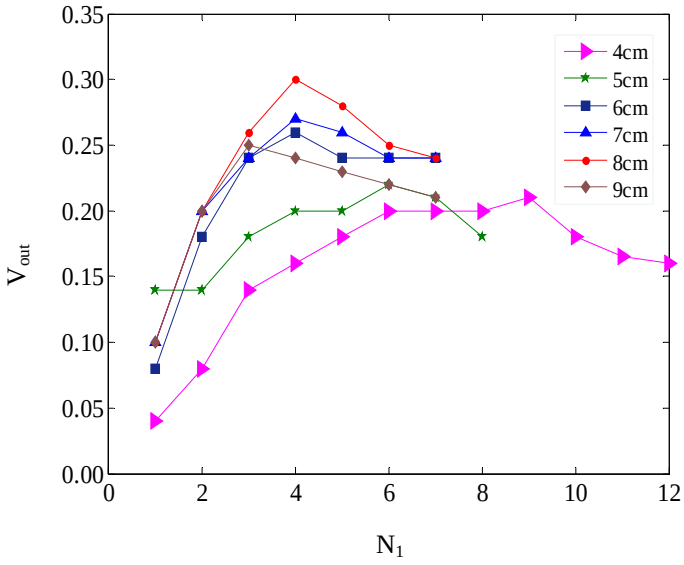

Figure A.5 Measurement results on the combinations of N_1 and r_R to find optimal V_{out}.

Figure A.5 shows the measurement results on the combinations of N_1 and r_R with their corresponding output voltage V_{out}. The experiment results showed that the optimal output voltage was with the value of 0.32 V on the combination of the radius of 8cm along with 4-turns reader antenna. Hence, we plotted the measurement results on the combinations of N_1 and r_R that gave the maximum output voltage along with equation (A.11) and equation (A.13), as shown in Figure A.6. Note that the values are rounded into the closest integers. Obviously, the experiment results didn't match with either one of the theoretical estimation equations. However, equation (A.13) is closer to the measurement results. There were some issues that might contribute to this discrepancy, for example, we can only use the tuning capacitors with the closest value to the theoretical ones while they are available. The coil antenna quality wound around

the reader antenna frame also affected the measurement results. General speaking, when the coil antennas wound around the reader antenna frame become more compact, the better the quality factor, more energy can be transferred at resonance [A.28].

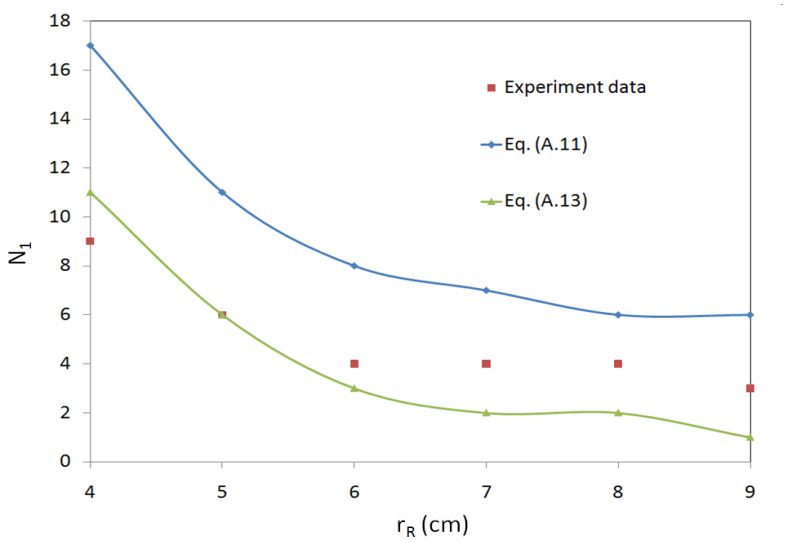

Figure A.6 Comparison of N_1 as a function of r_R on Eq. (A.11) and Eq.(A.13) with parameters based on measurement and compared to the experiment data.

Then, we would like to examine equation (A.10). We fixed the reader and transponder antenna at the distance of 10 cm. The operating resonant frequency was set to the frequency of 1.34 MHz. We fixed the parameters on the reader side, such as r_R, N_1, L_1, R_1, and tuning capacitance with the values of 8 cm, 4, 13.10 µH, 2.3 Ω, and 1.1 nF, respectively. We increased the resistances of R_{ACload} and made the coil antennas to have different turns on transponder antenna frame with the radius of 1.2 cm. Then we measured the output voltage, V_{out}, across the R_{ACload} to find out which combinations of N_2 and R_{ACload} gave the maximum V_{out}. Figure A.7 shows the measurement results on the combinations of N_2 and R_{ACload} in finding optimal V_{out}. The experiment results show

that when the R_{ACload} was with the resistance of 0.6 MΩ and with N_2=44 gave the maximum V_{out} with the reading of 0.42 V.

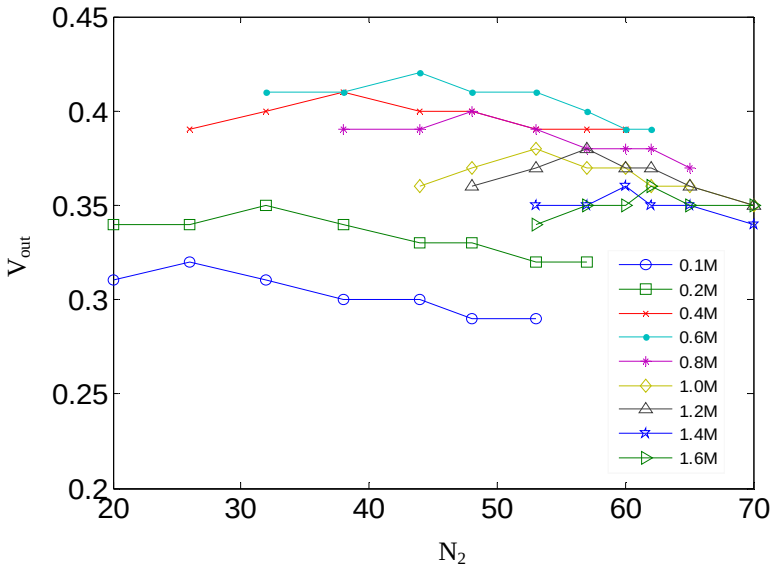

Figure A.7 Measurement results on the combinations of N_2 and R_{ACload} to find optimal V_{out}.

We plotted the measurement results on the pairs of R_{ACload} and N_2 that gave the maximum output voltage along with equation (A.10), as shown in Figure A.8. Again, the experiment results didn't match with the theoretical estimation. However, the trends of the plots for experiment data and theoretical estimation were both mono tone increasing. The values of N_2 increased along with the increments of R_{ACload}, therefore more voltage can be induced to drive larger load impedance. Since the parameters we used to plug into the equations were based on the measurement data, there might be some errors occurred either due to the equipment limitations or simply measurement errors. Therefore, we explored the theoretical parameters of the coil antenna on its self inductance values and equivalent series resistances in next section.

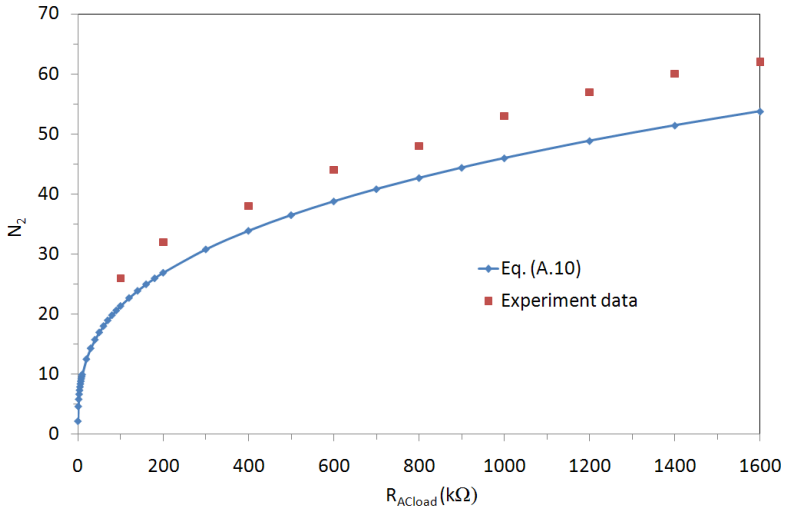

Figure A.8 N_2 as a function of R_{ACload} on Eq. (A.10) with parameters based on measurement and compared to the experiment data.

A.4.2 Theoretical Parameters Approach

A.4.2.1 AC Resistance

When the wire of the coil antenna is used at high frequency, its resistance value will increase due to the skin effect of the conductor wire [A.29]. The formula of AC resistance, R_{ac}, that describe this phenomenon can be found as [A.30]

$$R_{ac} \approx \frac{l}{2\pi r_w \delta \sigma} = \frac{l}{2 r_w}\sqrt{\frac{f\mu}{\pi\sigma}} \tag{A.14}$$

where r_w is the radius of the wire, δ is the skin depth, σ is the conductibility of the material, l is the total length of the wire, f is the frequency, μ is the permeability.

The skin depth formula can be found as

$$\delta = \frac{1}{\sqrt{\pi f \mu \sigma}} \tag{A.15}$$

A.4.2.2 Inductance of Circular Antenna

Figure A.9 shows a single-turn circular coil antenna with its radius of r and the wire diameter of $2r_w$.

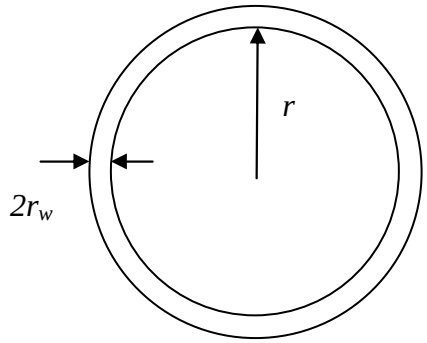

Figure A.9 A single-turn circular coil antenna.

Then, the low frequency inductance formula for a circular coil antenna can be found as [A.30]

$$L = 4\pi \times 10^{-7}(2r - r_w)\left[\left(1 - \frac{k^2}{2}\right)K(k) - E(k)\right] + 10^7 \times \pi r\mu \text{ , if } r>r_w \qquad \text{(A.16)}$$

$$L = 4\pi \times 10^{-7} r\left[\ln\left(\frac{8r}{r_w}\right) - 2 + \frac{\mu_r}{4}\right] \text{ , if } r>>r_w$$

where $k = \dfrac{2\sqrt{r(r-r_w)}}{2r - r_w}$

and *K(k)* and *E(k)* are the complete elliptic integrals of the first and second kind defined as

$$K(k) = \int_0^{\pi/2} \frac{d\theta}{\sqrt{1-k^2\sin^2\theta}}, E(k) = \int_0^{\pi/2} \sqrt{1-k^2\sin^2\theta}\, d\theta \qquad \text{(A.17)}$$

where μ_r is the relative permeability.

The high frequency inductance can be found as [A.30]

$$L = 4\pi \times 10^{-7}(2r - r_w)\left[\left(1 - \frac{k^2}{2}\right)K(k) - E(k)\right], \text{ if } r>r_w \qquad (A.18)$$

$$L = 4\pi \times 10^{-7} r\left[\ln\left(\frac{8r}{r_w}\right) - 2\right], \text{ if } r>>r_w$$

A.4.2.3 Experiment Results

Based on parameters from AWG wire chart [A.31], the single turn AC resistance, R_{10} and R_{20}, and inductance, L_{10} and L_{20}, can be calculated as

$R_{20} = 0.04\Omega$
$L_{20} = 0.11\mu H$
$R_{10} = 0.0136\Omega$
$L_{10} = 0.083\mu H$

Along with other parameters we obtained earlier, such as

$f = 1.3MHz$
$R_{ACload} = 50000\Omega$
$x = 10cm$
$r_{Tag} = 1.2cm$
$N_2 = 17$
$R_{ACload} = 50000\Omega$

By plugging those parameters into equations (A.10), (A.11) and (A.13) to have the new curve on N_2 as a function of R_{ACload} and N_1 as a function of r_R, respectively. Therefore, we can obtain the new curves that were all based on the theoretical calculation. Then we compared those new curves to the measurement results again. Figure A.10 shows the curve of N_1 as a function of r_R based on equations (A.11) and (A.13) along with the measurement data, while Figure A.11 shows the curve of N_2 as a function of R_{ACload} based on equation (A.10) along with the measurement results. However, the theoretical

exploration plots still couldn't match with the experiment results. Therefore, the third approach of using the scale factor was introduced to adjust the theoretical curve trying to describe the experiment data.

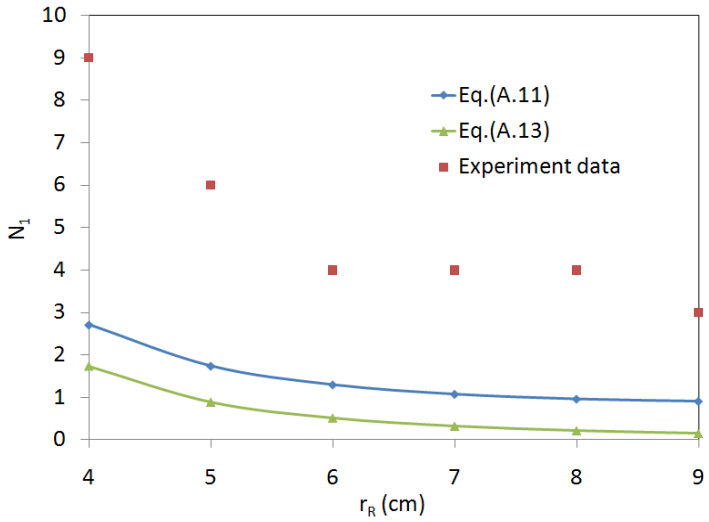

Figure A.10 Comparison of N_1 as a function of r_R plots on Eq. (A.11) and Eq. (A.13) with parameters based on calculation and compared to the experiment data.

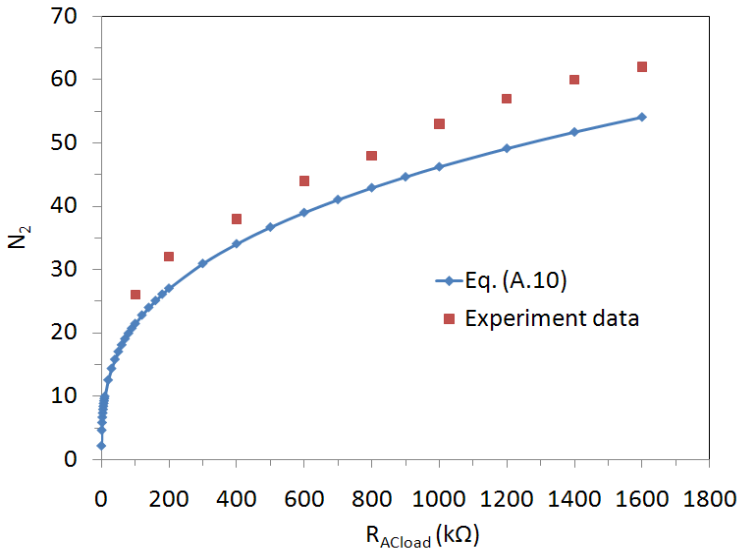

Figure A.11 N_2 as a function of R_{ACload} on Eq. (A.10) with parameters based on calculation and compared to experiment data.

A.4.3 Scale Factor Approach

Since the trends for both theoretical plots and the measurement data were the same, there were just discrepancies between the two. The scale factors α, β, and t were used to adjust our hypothesis equations to better fit the measurement results. The scale factor, α, was used to scale the equivalent series resistance, R_2, and the scale factor, β, was used to scale the self inductance, L_2,on the transponder side. The scale factor, t, was used to scale up the equivalent series resistance, R_1, on the reader side. Therefore the new hypothesis equations became

$$R_2 = \alpha N_2 R_{20} \tag{A.19}$$

$$L_2 = \beta N_2^2 L_{20} \tag{A.20}$$

$$R_1 = tN_1 R_{10} \tag{A.21}$$

Therefore, the new formulas for N_1 and N_2 can be derived as

$$N_2 = \sqrt[3]{\frac{\alpha}{\beta^2}} \sqrt[3]{\frac{2 R_{20} R_{ACload}}{\omega_0^2 L_{20}^2}} \tag{A.22}$$

$$N_1 = t \frac{2\pi r_R R_{10} \left(N_2 R_{20} + \frac{\left(2\pi f N_2^2 L_{20}\right)^2}{R_{ACload}} \right)}{\left(\frac{\pi^2 f \mu_0 N_2 r_{Tag}^2 r_R^2}{\left(r_R^2 + x^2\right)^{3/2}} \right)^2} \tag{A.23}$$

The formula for N_2 was scaled by a factor of $\sqrt[3]{\frac{\alpha}{\beta^2}}$, while the formula for N_1 was scaled by the factor of t.

Next, we would like to find out the values of the scale factor to see if they can be used to adjust the theoretical curves to fit the measured data. The AWG 34 magnet wire was used to make the transponder coil antenna with different number of turns, N_2, on the transponder frame with the radius of 1.2 cm. Then, we used impedance meter (HP 4192AF) to measure the corresponding AC equivalent series resistance, R_2, with respect to different number of turns. Figure A.12 shows the plots of AC equivalent series resistance, R_2, as a function of N_2, on the transponder side. The plot of the theoretical value was explored based on the equation (A.19), while the single turn AC equivalent series resistance, R_{20}, was calculated earlier with a resistance of 0.04 Ω. Then, the values of R_2 were obtained by multiplying to the number of turns to the single turn AC equivalent series resistance.

In Figure A.12, the theoretical value is too far away from the impedance meter measurement data, especially when the number of turns increases to larger numbers. This is due to the current in the adjacent coil wires cause a magnetic field resulting in an asymmetric current distribution. Therefore, in order to determine the AC resistance accurately, numerical methods have to be applied [A.22]. The theoretical values based on the equation (A.8) are valid only when DC resistance is considered. In addition, the scale factor, α, in this case will be varied with respect to different number of turns. However, we still continued this process to see if we can obtain a value of β that can compensate the value of α, so the final scale factor $K=\sqrt[3]{\frac{\alpha}{\beta^2}}$ is able to fine tune and complete our hypothesis equations.

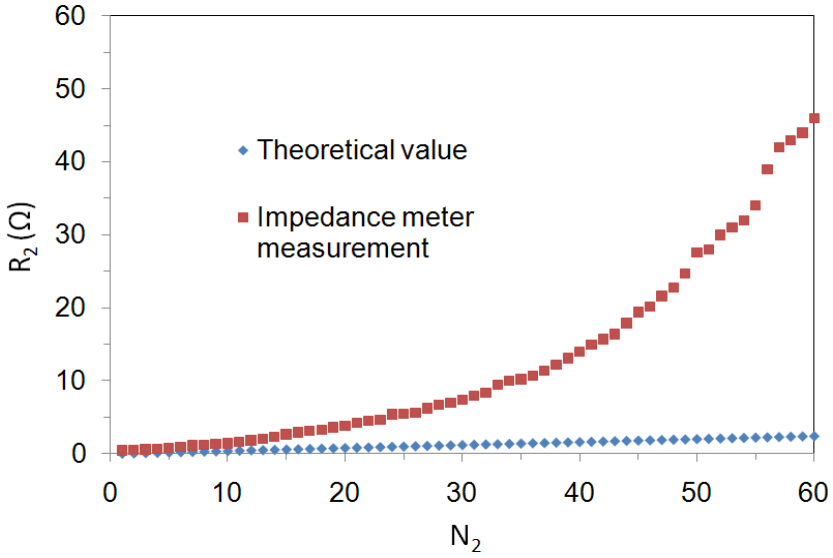

Figure A.12 Theoretical and measurement plots on R_2 as a function of N_2.

Thus, we continue to explore the theoretical plot for self inductance, L_2, with respect to different number of turns by using the equation (A.20). The values of L_2 were obtained by multiplying N_2^2 to the single turn self inductance, L_{20}. The single-turn self inductance was with a value of 0.11 μH that we obtained earlier. Figure A.13 shows the plots of self inductance, L_2, as a function of N_2. The inductance values of L_2 were also measured by the impedance meter and compared to the theoretical values. The theoretical curve and the measurement data were not agreed to each other, especially when the number of turns became too large. This is again due to the adjacent coil wires generate a magnetic field resulting in an asymmetric current distribution [A.30]. Therefore, in order to determine the multi-turn self inductance accurately, numerical methods have to be applied [A.32].

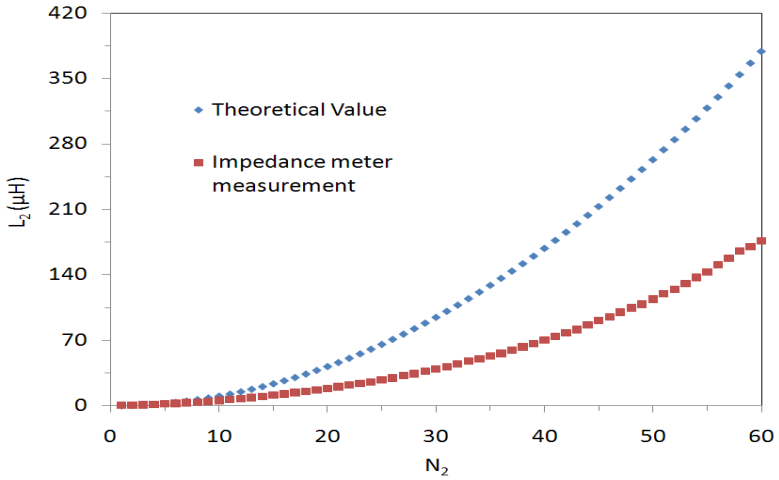

Figure A.13 Theoretical and measurement plots on L_2 as a function of N_2.

Overall, when we put together the scale factor α and β into the final scale factor $K=\sqrt[3]{\frac{\alpha}{\beta^2}}$, and plot as a function of N_2, as shown in Figure A.14. The final scale factor still couldn't help us to fine tune the theoretical curve to match with the measurement data since its values vary with N_2. When N_2 increases, it requires larger scale factor that will make the required number of turns even larger.

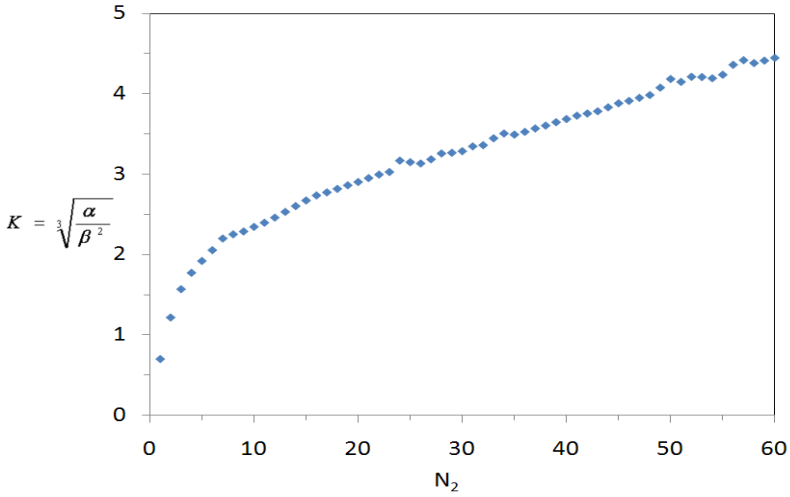

Figure A.14 The scale factor $K=\sqrt[3]{\frac{\alpha}{\beta^2}}$ as a function of N_2.

A.5 Summary

In this study, three different approaches were used to optimize the coupling efficiency of inductive coupling resonant circuit. Those approaches were based on a single governing equation derived from the system point of view. Under the assumptions that the parameters, either measureable or can be calculated from formulas, would be proportional to the number of turns of the coil antenna. The optimization processes were based on the theoretical exploration of the formulas compared to the physical measurement data. The optimization approaches used in this study didn't match with the measurement data; however, the efforts to optimize the coupling efficiency of an inductive coupling resonant circuit from scientific point of view were made. The methodology suggested a systematic way to characterize the parameters toward the optimization of inductive coupling resonant circuit.

To continue this research, some issues need to be exercised, such as the quality of the coil antenna made, the tuning capacitances used, and the limitations of the equipments, etc. These factors also need to be taken into consideration so that the discrepancies between the measurement data and the theoretical exploration would be minimized. In the mean time, a numerical method that determines the multi-turn self inductance and equivalent series resistor needs to be studied to relate the theoretical and measurement data.

APPENDIX B

A BENCHTOP SPECTRUM ANALYZER LABVIEW PROGRAM

Auto Power Spectrum

The two-sided power spectrum is computed from the FFT as follows

$$S_{signal}(f) = \frac{FFT(signal) \bullet FFT^{*}(signal)}{N^{2}}$$

where FFT*(signal) denotes the complex conjugate of FFT(signal) and N is the number of points in the signal taken into calculation.

Frequency Estimate

Estimated frequency of the peak in the input Power Spectrum and is computed as

$$Estimate\_frequency = \frac{\sum(Power\_spectrum(j) * (j * df))}{\sum(Power\_spectrum(j))}$$

for $j = I$ – span/2, …I + span/2,

where I = peak index, Power Spectrum (j) = power at j, and df = frequency span width.

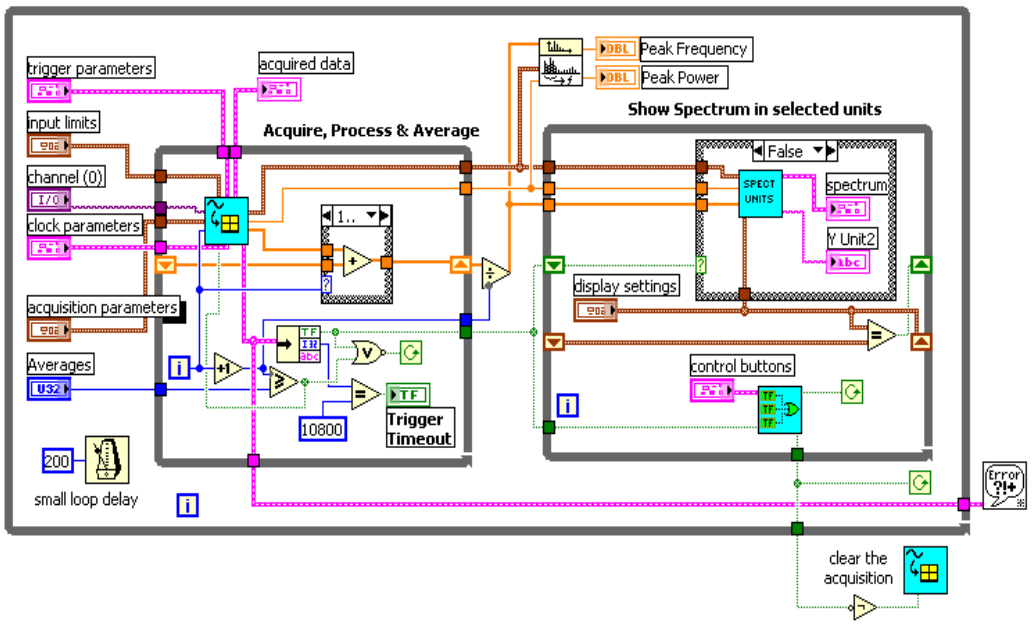

REFERENCES

[1.1] John Enderle, Susan Blanchard, and Joseph Bronzino, Introduction to biomedical engineering, Elsevier Academic Press, 2nd edition, 2005.

[1.2] R.S. Khandpur, Biomedical instrumentation: technology and applications, McGraw-Hill, 1st edition, 2005.

[1.3] Tatsuo Togawa, Toshiyo Tamura, and P. Åke Öberg, Biomedical transducers and instruments, CRC PRESS, 1st edition, 1997.

[1.4] P. Åke Öberg, Tatsuo Togawa, and Francis A. Spelman, Sensors Applications, Volume 3, Sensors in Medicine and Health Care, Wiley-VCH, 1st edition, 2004.

[1.5] Rogier A.M. Receveur, Fred W. Lindemans, and Nicolaas F. de Rooij, "Microsystem technologies for implantable applications," *Journal of Micromechanics and Microengineering*, Vol. 17, pp. R50–R80, 2007.

[1.6] Gregory T. A. Kovacs, Micromachined transducers sourcebook, McGraw-Hill, 1st edition, 1998.

[1.7] K. Finkenzeller, RFID handbook: fundamentals and applications in contactless smart cards and identification, Chichester, England, New York, Wiley, 2nd edition, 2003.

[1.8] Steven Shepard, RFID: Radio frequency identification, McGraw-Hill, 1st edition, 2004.

[1.9] Dennis E. Brown, RFID implementation, McGraw-Hill, 1st edition, 2006.

[1.10] Amy C. Richards Grayson, Rebecca S. Shawgo, Audrey M. Johnson, Nolan T. Flynn, Yawen Li, Michael J. Cima, And Robert Langer, "A BioMEMS review: MEMS technology for physiologically integrated devices," *Proceedings of the IEEE*, Vol. 92, No. 1, pp. 6-21, January 2004.

[1.11] F.E.H. Tay, Microfluidics and bioMEMS applications, Kluwer, 1st edition, 2002.

[1.12] Robert S.H. Istepanian, Swamy Laxminarayan, and S. Pattichis Constantinos, M-health: emerging mobile health systems, Springer, 1st edition, 2005.

[1.13] Krzysztof Iniewski, Wireless technologies: circuits, systems, and devices, CRC, 1st edition, 2007.

[1.14] IEEE 802.15 Working Group for Wireless Personal Area Networks (WPANs)

[1.15] Guang-Zhong Yang and M. Yacoub, Body sensor networks, Springer, 1st edition, 2006.

[1.16] T. O'Donovan, J. O'Donoghue, C. Sreenan, P. O'Reilly, D. Sammon, and K. O'Connor, "A context aware wireless body area network (BAN)," *Proc. 3rd International Conference on Pervasive Computing Technologies for Healthcare,* 2009.

[2.1] S. Chatzandroulis, D. Tsoukalas, and P.A. Neukomn, "Miniature pressure system with a capacitive sensor and a passive telemetry link for use in implantable applications," *Journal of Microelectrmmechanical Systems*, 9(1), pp. 18-23, 2000.

[2.2] C. Hierold, B. clasbrummel, D. Behrend, T. Scheiter, M. Steger, K. Oppermann, H. Kapels, E. Landgraf, D. Wenzel, and Etzrodt, "Implantable low power

integrated pressure sensor system for minimal invasive telemetric patient monitoring," *Proceedings of the IEEE Micro Mechanical Systems (MEMS)*, Heidelberg, Germany, pp. 568-573, Feb. 1998.

[2.3] A. DeHennis, and K. D. Wise, "A double-sided single-chip wireless pressure sensor," *in Proceedings of the IEE Micro Electro Mechanical Systems Conference*, Las Vegas, NV, pp. 252-255, Feb. 2002.

[2.4] Q. Huang, and M. Oberle, "0.5-mW passive telemetry IC for biomedical applications," *IEEE of Solid-State Circuits*, Vol. 33, pp937-946, 1998.

[2.5] David W. Kuhns, M., and Benton Free, "System and methods for remote sensing using inductively coupled transducers" *Patent, Pub. No.: 2008/0012579 A1*, Pub. Date: Jan.17, 2008.

[2.6] Roy Want, "Enabling ubiquitous sensing with RFID," *Computer*, 37(4), pp. 84-86, 2004.

[2.7] Olivier Chevalerias, Terence O'Donnell, Daithi Power, Neil O'Donovan, Gerald Duffy, Gary Grant, and Sean Cian O'Mathuna, "Inductive telemetry of multiple sensor modules," *IEEE Pervasive Computing*, 4(1), pp. 46-52, 2005.

[2.8] Matthai Philipose, Joshua R. Smith, Bing Jiang, Alexander Mamishev, Sumit Roy, and Kishore Sundara-Rajan, "Battery-free wireless identification and sensing," *IEEE Pervasive Computing*, 4(1), pp. 37-45, 2005.

[2.9] S. Chatzandroulis and D. Tsoukalas, "Capacitance to frequency converter suitable for sensor applications using telemetry," *Analog Integrated Circuits and Signal Processing*, Volume 27, Numbers 1-2, pp. 31-38, 2001.

[2.10] T. Roz and V. Fuentes., “Using low power transponders and tags for RFID applications,” 2004.

[2.11] Hongwei Shen, Lilan Li, and Yumei Zhou, “Fully integrated passive UHF RFID tag with temperature sensor for environment monitoring,” *ASIC, 2007. ASICON ’07*. 7th International Conference on, pp. 360-363, 2007.

[2.12] Tomohiro Yamada, Takumi Uezono, Hirotaka Sugawara, Kenichi Okada, Kazuya Masu, Akio Oki, and Yasuhiro Horiike, “Battery-less wireless communication system through human body for in-vivo healthcare chip,” *IEEE Topical Meeting on Silicon Monolithic Integrated Circuits in RF Systems*, pp. 322-325, 2004.

[2.13] William H. Moore, Daniel P. Holschneider, Tina K. Givrad, and Jean-Michel I. Maarek, “Transcutaneous RF-powered implantable minipump driven by a Class-E transmitter,” *IEEE Trans. Biomed. Eng.*, 53(8), pp. 1705–1708, 2006.

[2.14] Radislav A. Potyrailo and William G. Morris, “Multianalyte chemical identification and quantitation using a single radio frequency identification sensor,” *Analytical Chemistry*, Vol. 79, No. 1, pp. 45-51, January 1, 2007.

[2.15] M. Nowak, N. Delorme, F. Conseil, and G. Jacquemod, “A novel architecture for remote interrogation of wireless battery-free capacitive sensors,” *Electronics, Circuits and Systems, 2006. ICECS ’06. 13th IEEE International Conference on*, pp. 1236-1239, 10-13, Dec. 2006.

[2.16] Andrew D. DeHennis and Kensall D. Wise, “A fully integrated multisite pressure sensor for wireless arterial flow characterization,” *Journal of*

Microelectromechanical Systems, 15(3), pp. 678-685, June 2006.

[2.17] Alison J. Clark and Lorne A. Whitehead, "Novel resonant-frequency sensor to detect the kinetics of protein adsorption," *Review of Scientific Instruments*, 73(12), pp. 4339-4346, December 2002.

[2.18] Byunggil Lee and Howon Kim, "Ubiquitous RFID based medical application and the security architecture in smart hospitals," *International Conference on Convergence Information Technology* (ICCIT 2007), pp.2359-2362, 2007.

[2.19] Lucas Ricciardi, Inke Pitz, Said F. Al-Sarawi, Vijay Varadan, and Derek Abbott, "Investigation into the future of RFID in biomedical applications," *Bioengineered and Bioinspired Systems, Proceedings of the SPIE*, Volume 5119, pp. 199-209, 2003.

[2.20] M. Ghovanloo and K. Najafi, "A fully digital frequency shift keying demodulator chip for wireless biomedical implants," *IEEE Southwest Symposium on Mixed-Signal Design 2003*, pp.223–227, 2003.

[2.21] K. Finkenzeller, RFID handbook: fundamentals and applications in contactless smart cards and identification, Chichester, England, New York, Wiley, 2nd edition, 2003.

[2.22] 2005 IEEE standard for safety levels with respect to human exposure to radio frequency electromagnetic fields, 3 kHz to 300 GHz, IEEE Std C95.1, pp. 25, 2006.

[2.23] E. Haile and J. Lepkowski, *Oscillator circuits for RTD temperature sensors, Application note AN895*, Microchip Technology Inc., pp. 21-22, 2004.

[2.24] T. Ativanichayaphong, J. Wang, W. Huang, S. Rao, and J.-C. Chiao, "A simple wireless batteryless sensing platform for resistive and capacitive sensors," *IEEE Sensors 2007 Conference*, Atlanta, Georgia, pp. 139-142, Oct. 26-28, 2007.

[2.25] P. Troyk, and M. Schwan, "Closed-loop class E transcutaneous power and data link for microimplants," *IEEE Transactions on Biomedical Engineering*, Vol. 39(6), pp. 589-599, June 1992.

[2.26] P.R. Troyk and G.A. DeMichele, "Inductively-coupled power and data link for neural prostheses using a class-E oscillator and FSK modulation," *IEEE International Conference Engineering in Medicine and Biology Society*, Vol. 4, pp. 3376-3379, Sept. 2003.

[2.27] N. Chaimanonart, D.J. Young, "Remote RF powering system for wireless MEMS strain sensors," *IEEE Sensors Journal*, Vol. 6(2), pp. 484-489, April 2006.

[2.28] Zoubir Hamici, Roland Itti, and Jacques Champier, "A high-efficiency power and data transmission system for biomedical implanted electronic devices," *Measurement Science and Technology*, 7, pp. 192–201, 1996.

[2.29] P.R. Troyk, and M.A. Schwan, "Class E driver for transcutaneous power and data Link for implanted electric device," *Medical & Biological Engineering & Computing*, 30, pp. 69-75, January 1992.

[2.30] Zhijun Tang, Yigang He, Zhouguo Hou, Bing Li, "The effects of antenna properties on read distance in passive backscatter RFID systems," *Wireless Communications and Trusted Computing*, International Conference on Networks

Security, Vol. 1, pp.120-123, 2009.

[2.31] S.C.Q. Chen and V. Thomas, "Optimization of inductive RFID technology," *Proceedings of the 2001 IEEE International Symposium on Electronics and the Environment*, pp. 82-87, 2001.

[2.32] microID® 125 kHz RFID System Design Guide, Microchip Technology Inc., 2004.

[2.33] microID® 13.56MHz RFID System Design Guide, Microchip Technology Inc., 2004.

[2.34] P. Sorrells, "Optimizing read range in RFID systems," Electronics Design, Strategy, News (EDN), pp.173-184, Dec 7, 2000.

[2.35] David Lee Hall, Sonya A. H. McMullen, *Mathematical techniques in microsystems data fusion*, Norwood Massachusetts, Artech House Inc., 2nd edition, 2004.

[2.36] Luca Catarinucci, Mauro Cappelli, Riccardo Colella, Luciano Tarricone, "A novel low-cost icrosystems-tag for RFID applications in healthcare," *Microwave and Optical Technology Letters*, 50(11), pp. 2877 – 2880, August 2008.

[2.37] C.S. Fraser, M.R. Shortis, and G. Ganci, "Multi-sensor system self-calibration," *SPIE Videometrics IV*, Vol. 2598, pp. 2-18, 1995.

[2.38] Christopher Immer, Anthony Eckhoff, John Lane, Jose Perotti, John Randazzo, Norman Blalock, and Jeff fiees, "Multisensor arrays for greater reliability and accuracy," *NASA Tech Briefs*, July 2004.

[3.1] C.W. Oomens, O.F.J.T. Bressers, E.M.H. Bosboom, C.V.C. Bouten, and D.L. Bader, "Can loaded interface characteristics influence strain distribution in muscle adjacent to bony prominences," *Computer Methods in Biomechanics and Biomedical Eng.*, 6(3), pp. 171-180, 2003.

[3.2] C.W. Oomens, R.G. Breuls, C.V.C. Bouten, F.P.T. Baaijens, and D.L. Bader, "A hierarchical approach to study damage evolution in skeletal muscle - a contribution to pressure ulcer research," *Summer Bioengineering Conference*, pp. 299-300, 2003.

[3.3] C. Gehin, E. Brusseau, R. Meffre, P.M. Schmitt, J.F. Deprez, and A. Dittmar, "Which techniques to improve the early detection and prevention of pressure ulcers?," *Proceedings of the 28th IEEE, EMBS Annual International Conference*, pp. 6057-6060, 2006.

[3.4] M.W. Ferguson-Pell, "Seat cushion selection," *Journal of Rehab. Res. Dev., Clin. Suppl.*, pp. 49-73, 1990.

[3.5] J. Braden Barbara and Maklebust Joann, "Wound wise: preventing pressure ulcers with the braden scale," *American Journal of Nursing*, 105(6), pp. 70-72, 2005.

[3.6] J.G. Webster, Prevention of pressure sores: engineering and clinical aspects, Adam Hilger, 1991.

[3.7] Y.K. Jan and D.M. Brienza, "Technology for pressure ulcer prevention," *Topics in Spinal Cord Injury Rehabilitation*, 11(4), pp. 30-41, 2006.

[3.8] V.C. Taylor, “Force sensing array: seating solutions through pressure mapping,” *Rehab & Community Care Management*, p. 68, 1999.

[3.9] S.A. Crawford, B. Strain, B. Gregg, D.M. Walsh, and A.P. Porter-Armstrong, “An investigation of the impact of the force sensing array pressure mapping system on the clinical judgment of occupational therapists,” *Clinical Rehabilitation*, 19(2), pp. 224-231, 2005.

[3.10] G.M. Yarkony, “Pressure ulcers: A review,” *Archives of Physical Medicine and Rehabilitation*, 75, pp. 908-917, 1994.

[3.11] M.W. Ferguson-Pell, “Design criteria for measurement of pressure at body/support interfaces,” *Eng. In Medicine*, 9(4), pp. 209-214, 1980.

[3.12] J.C. Löttersy, W. Olthuis, P.H. Veltink, and P. Bergveld, “The mechanical properties of the rubber elastic polymer polydimethylsiloxane for sensor applications,” *J. Micromech. Microeng*., 7, pp. 145-147, 1997.

[3.13] S.I. Yaniger, “Force sensing resistors: A review of the technology,” *Electro. Int*., pp. 666-668, 1991.

[3.14] T. Ativanichayaphong, J. Wang, W. Huang, S. Rao, and J.-C. Chiao, “A simple wireless batteryless sensing platform for resistive and capacitive sensors,” *IEEE Sensors 2007 Conference*, pp. 139-142, 2007.

[4.1] Peter J. Kahrilas and John E. Pandolifino "The epidemiology and pathophysiology of gastroesphageal reflux disease," Managing failed anti-reflux therapy, Chapter 1, pp. 1-14, 2006.

[4.2] Kenneth R. DeVault and Donald O. Castell, "Updated guideline for the diagnosis and treatment of gastroesophageal reflux disease," *American Journal of Gastroenterology*, Vol. 100, pp. 190-200, 2005.

[4.3] D. Sifrim, R. Holloway, J. Silny, Z. Xin, J. Tack, A. Lerut, and J. Janssens, "Acid, nonacid, and gas reflux in patients with gastroesophageal reflux disease during ambulatory 24-hour pH-impedance recordings," *Gastroenterology*, 120(7), pp. 1588-1598, 2001.

[4.4] I. Mainie, R. Tutuian, S. Shay, M. Vela, X. Zhang, D. Sifrim, and D.O. Castell, "Acid and non-acid reflux in patients with persistent symptoms despite acid suppressive therapy: a multicentre study using combined ambulatory impedance-pH monitoring," *An International Journal of Gastroenterology and Hepatology*, Vol. 55, pp. 1398-1402, 2006.

[4.5] Joshua J. Ofman, “The relation between gastroesophageal reflux disease and esophageal and head and neck cancers: a critical appraisal of epidemiologic literature,” *The American Journal of Medicine*, 111(8), pp. 124-129, 2001.

[4.6] F. Vela Marcelo and Michael F. Vaezi, "The role of multichannel intraluminal impedance and pH monitoring in the diagnosis of gastroesophageal reflux disease," *US Gastroenterology Review*, Issue II, pp.75-77, October 2007.

[4.7] R. Tutuian, M. Vela, S. Shay and D. Castell, “Multichannel intraluminal impedance in esophageal function testing and gastroesophageal reflux monitoring,” *Journal of Clinical Gastroenterology*, 37(3), pp. 206-215, Sept. 2003.

[4.8] Monika Kwiatek and John Pandolfino, “Prolonged reflux monitoring: capabilities of bravo pH and impedance-pH systems,” Current GERD Reports, Vol. 1, No. 3, pp. 165-170.

[4.9] J. Pandolfino, J. Richter, T. Ours, J. Guardino, J. Chapman and P. Kahrilas, “Ambulatory esophageal pH monitoring using a wireless system,” *The American Journal of Gastroenterology*, 98(4), pp. 740-749, April 2003.

[4.10] O. Kawamura, M. Aslam, T. Rittmann, C. Hofmann and R. Shaker, “Physical and pH properties of gastroesopharyngeal refluxate: a 24-hour simultaneous ambulatory impedance and pH monitoring study,” *The American Journal of Gastroenterology*, 99(6), pp. 1000-1010, June 2004.

[4.11] D. Castell and M. Vela, “Combined multichannel intraluminal impedance and pH-metry: an evolving technique to measure type and proximal extent of gastroesophageal reflux,” *The American Journal of Medicine*, 11(8), pp. 157-159, Dec. 2001.

[4.12] J. Gonzalez-Guillaumin, D. Sadowski, K. Kaler and M. Mintchev, “Ingestible capsule for impedance and pH monitoring in the esophagus,” *IEEE Transactions on Biomedical Engineering*, 54(12), pp. 2231-2236, Dec. 2007.

[4.13] G. Scarpulla, S. Camilleri, P. Galante, M. Manganaro and M. Fox, “The impact of prolonged pH measurements on the diagnosis of gastroesophageal reflux disease: 4-day wireless pH studies,” *The American Journal of Gastroenterology*, 102(12), pp. 2642-2647, Dec. 2007.

[4.14] Y. Salvatore, S. MC. Vieira, B. Hauser, “Will esophageal impedance replace pH monitoring? Review,” *Pediatrics*, 119(1), pp. 118-22, 2007.

[4.15] Steven Shay, “Esophageal impedance monitoring: the ups and downs of a new test,” *The American Journal of Gastroenterology*, 99(6), pp. 1020-1022, June 2004.

[4.16] I. Hirano, “Modern technology in the diagnosis of gastroesophageal reflux disease: bilitec, intraluminal impedance and bravo capsule pH monitoring,” *Alimentary pharmacology & therapeutics*, 23(1), pp. 12-24, 2006.

[4.17] John E. Pandolfino, Marcelo F. Vela, “Esophageal-reflux monitoring,” *Gastrointestinal Endoscopy*, Volume 69, Issue 4, pp. 767-986, April 2009.

[4.18] Radu Tutuian and Donald O. Castell, “Gastroesophageal reflux monitoring: pH and impedance,” *GI Motility online*, 2006.

[4.19] K. Finkenzeller, RFID handbook: fundamentals and applications in contactless smart cards and identification, Chichester, England, New York, Wiley, 2003.

[4.20] E. Haile and J. Lepkowski, Oscillator circuits for RTD temperature sensors, Application note AN895, Microchip Technology Inc., pp. 21-22, 2004.

[4.21] T. Ativanichayaphong, J. Wang, W. Huang, S. Rao, and J.-C. Chiao, “A simple wireless batteryless sensing platform for resistive and capacitive sensors,” *IEEE Sensors 2007 Conference*, Atlanta, Georgia, pp. 139-142, Oct. 26-28, 2007.

[4.22] G. Kim, M. Morgan, B. K. Hahm, A. Bhunia, J. H. Mun, and A. S. Om, "Interdigitated microelectrode based impedance biosensor for detection of

salmonella enteritidis in food samples," *Journal of Physics: Conference Series*, 100, 052044, 2008.

[4.23] Alexander V. Mamishev, Kishore Sundara-Rajan, Fumin Yang, Yanqing Di, and Markus Zahn, "Interdigital sensors and transducers," *Proceedings of the IEEE*, 92(5), pp. 808-845, 2004.

[4.24] David R. Lide, CRC handbook of chemistry and physics, 86th edition, CRC Press, 2005.

[4.25] I. Hirano, Q. Zhang, J. Pandolfino, and P. Kahrilas, "Four-day Bravo pH capsule monitoring with and without proton pump inhibitor therapy," *Clinical Gastroenterology and Hepatology*, 3(11), pp. 1083-1088, 2005.

[4.26] W.-D. Huang, J. Wang, T. Ativanichayaphong, L.-C. Hsu, S. Deb, M. Chiao and J.-C. Chiao "Investigation of repeatability of sol-gel iridium oxide ph sensor on flexible substrate," *SPIE Proc.* Vol. 7269, 726916, 2008.

[4.27] 2005 IEEE standard for safety levels with respect to human exposure to radio frequency electromagnetic fields, 3 kHz to 300 GHz, *IEEE Std C95.1*, 2006.

[4.28] K. Wise, D. Anderson, J. Hetke, D. Kipke, K. Najafi, "Wireless implantable microsystems: high-density electronic interfaces to the nervous system," *Proc. IEEE*, 92(1), pp. 76-97, Jan. 2004.

[4.29] P. R. Troyk and G. A. DeMichele, "Inductively-coupled power and data link for neural prostheses using a class-E oscillator and FSK modulation," *IEEE International Conference Engineering in Medicine and Biology Society*, Vol. 4, pp. 3376-3379, Sept. 2003.

[4.30] N. Chaimanonart, D.J. Young, “Remote RF powering system for wireless MEMS strain sensors,” *IEEE Sensors Journal*, 6(2), pp. 484-489, April 2006.

[4.31] P. R. Troyk, and M. A. Schwan, “Class E driver for transcutaneous power and data link for implanted electric device,” *Medical & Biological Engineering & Computing*, 30, pp. 69-75, January 1992.

[4.32] E.A. Johannessen, L. Wang, C. Wyse, D.R.S. Cumming, and J.M. Cooper, “Biocompatibility of a lab-on-a-pill sensor in artificial gastrointestinal environments,” *IEEE Transactions on Biomedical Engineering*, 53 (11), pp. 2333-2340, 2006.

[A.1] K. Finkenzeller, RFID handbook: fundamentals and applications in contactless smart cards and identification, Chichester, England, New York, Wiley, 2nd edition, 2003.

[A.2] K. Fotopoulou and B.W. Flynn, “Wireless powering of implanted sensors using RF inductive coupling,” *5th IEEE Conference on Sensors*, pp. 765-768, Oct. 2006.

[A.3] Wen H. Ko, Sheau Pyng Liang, “RF-powered cage system for implant biotelemetry,” *IEEE Transactions on Biomedical Engineering*, Volume BME-27, Issue 8, pp. 460-467, 1980.

[A.4] Wen H. Ko, Sheau P. Liang, and Cliff D. F. Fung, “Design of radio-frequency powered coils for implant instruments,” *Medical and Biological Engineering and Computing*, 15(6), pp. 634-640, 1977.

[A.5] Zhihua Wang, Songping Mai, and Chun Zhang, "Power issues on circuit design for cochlear implants," *4th IEEE International Symposium on Electronic Design*, Test and Applications, pp.163-166, 2008.

[A.6] D.J. Young, M.A. Zurcher, W.H. Ko, M. Semaan, and C.A. Megerian, "Implantable MEMS accelerometer microphone for cochlear prosthesis," *ISCAS 2007, IEEE International Symposium on Circuits and Systems*, pp. 3119-3122, May 2007.

[A.7] H.S. Ng, M.L. Sim, C.M. Tan, and C.C. Wong, "Wireless technologies for telemedicine," *BT Technology Journal*, Volume 24, Number 2, pp. 130-137, April 2006.

[A.8] R. Bashirullah, Wentai Liu, Ying Ji, A. Kendir, M. Sivaprakasam, Guoxing Wang, and B. Pundi, "A smart bi-directional telemetry unit for retinal prosthetic device," *ISCAS '03. Proceedings of the 2003 International Symposium on Circuits and Systems*, Volume 5, pp. V-5- V-8, 2003.

[A.9] W.T. Liu, K. Vichienchom, M. Clements, S.C. DeMarco, C. Hughes, E. McGucken, M. S. Humayun, E. De Juan, J.D. Weiland, and R. Greenberg, "A neuro-stimulus chip with telemetry unit for retinal prosthetic device," *IEEE Journal of Solid-state Circuits*, 35(10), pp. 1487-1497, 2000.

[A.10] J. Holleman, D. Yeager, R. Prasad, J.R. Smith, and B. Otis, "NeuralWISP: An energy-harvesting wireless neural interface with 1-m range," *Biomedical Circuits and Systems Conference*, BioCAS 2008 IEEE, pp. 37-40, Nov. 2008.

[A.11] Mingui Sun, Gusphyl A. Justin, Paul A. Roche, Jun Zhao, Brian L. Wessel, Yingze Zhang, and Robert J. Sclabassi, "Passing data and supplying power to neural implants," *IEEE Engineering In Medicine And Biology Magazine*, Vol. 25, Issue 5, pp. 39-46, September/October, 2006.

[A.12] S.C.Q. Chen and V. Thomas, "Optimization of inductive RFID technology," *Proceedings of the 2001 IEEE International Symposium on Electronics and the Environment*, pp. 82-87, 2001.

[A.13] P. Sorrells, "Optimizing read range in RFID systems," *Electronics Design, Strategy, News (EDN)*, pp.173-184, Dec 7, 2000.

[A.14] Ma Guanying, Yan Guozheng and He Xiu, "Power transmission for gastrointestinal □icrosystems using inductive coupling," *Physiolgical Measurement*, Vol. 28, pp. N9–N18, 2007.

[A.15] Bing Jiang, J.R. Smith, M. Philipose, S. Roy, K. Sundara-Rajan, and A.V. Mamishev, "Energy scavenging for inductively coupled passive RFID systems," *IEEE Transactions on Instrumentation and Measurement*, Vol. 56, No. 1, pp. 118-125, February 2007.

[A.16] Mark D. Zimmerman, Nattapon Chaimanonart, and Darrin J. Young, "In vivo RF powering for advanced biological research," *Proceedings of the 28th IEEE, EMBS Annual International Conference*, pp. 2506-2509, Aug 30-Sept 3, 2006.

[A.17] Bing Jiang, J.R. Smith, M. Philipose, S. Roy, K. Sundara-Rajan, A.V. Mamishev, "Energy scavenging for inductively coupled passive RFID systems,"

Instrumentation and Measurement Technology Conference, 2005. IMTC 2005. Proceedings of the IEEE, pp. 984-989, May 2005.

[A.18] Thierry Roz and Vincent Fuentes, "Using low power transponders and tags for RFID applications" *EM Microelectronic Marin SA*, Switzerland.

[A.19] C.M. Zierhofer and E.S. Hochmair, "Geometric approach for coupling enhancement of magnetically coupled coils," *IEEE Transactions on Biomedical Engineering*, Volume 43, Issue 7, pp. 708-714, 1996.

[A.20] M. Hakozaki, H. Oasa, and H. Shinoda, "Telemetric robot skin," *1999 IEEE International Conference on Robotics and Automation, Proceedings of the 1999 IEEE*, Volume 2, pp. 957-961, 1999.

[A.21] Peter Scholz, Christian Reinhold, Werner John, and Ulrich Hilleringmann, "Analysis of energy transmission for inductive coupled RFID tags," *2007 IEEE International Conference on RFID*, pp.183-190 , March 26-28, 2007.

[A.22] Christian Reinhold, Peter Scholz, Werner John, Ulrich Hilleringmann, "Efficient antenna design of inductive coupled RFID-systems with high power demand," *Journal of Communications*, Vol. 2, No. 6, pp. 14-23, November 2007

[A.23] Bert Lenaerts and Robert Puers, Omnidirectional inductive powering for biomedical implants, analog circuits and signal processing, Springer, 1st edition, 2009.

[A.24] N. Chaimanonart, W.H. Ko, D.J. Young, "Remote RF powering system for MEMS strain sensors," *Proceedings of IEEE Sensors*, Vol. 3, pp. 1522- 1525, 2004.

[A.25] Mark David Zimmerman, In vivo RF powering for advanced biological research," *Master thesis*, Department of Electrical Engineering and Computer Science, Case Western Reserve University, 2008.

[A.26] K. Van Schuylenbergh, Optimization of inductive powering of small bio-telemetry implants, *Ph.D. thesis*, K.U. Leuven, Belgium, 1998.

[A.27] 2005 IEEE standard for safety levels with respect to human exposure to radio frequency electromagnetic fields, 3 kHz to 300 GHz, IEEE Std C95.1, pp. 25, 2006.

[A.28] Dan Wang, Lei Xu, Huiming Huang, Daoheng Sun, "Optimization of tag antenna for RFID system," *2009 International Conference on Information Technology and Computer Science*, Vol. 2, pp.36-39, 2009.

[A.29] P. Waldow and I. Wolff, "The skin-effect at high frequencies," *IEEE Transactions on Microwave Theory and Techniques*, 33(10), pp. 1076-1082,1985.

[A.30] Kenneth L. Kaiser, Electromagnetic compatibility handbook, CRC Press, 2005.

[A.31] Youbok Lee, Microchip Antenna Circuit Design for RFID Applications, AN710, Microchip Technology Inc, 1999.

[A.32] Marc T. Thompson, Inductance calculation technique- Part II: Approximations and handbook methods power control and intelligent motion, December 1999.

BIOGRAPHICAL INFORMATION

LUN-CHEN HSU received his BEEE degree from Feng Chia University, Taichung, Taiwan in 1998, and MS degree from Institute of Communication Engineering, Tatung University, Taipei, Taiwan in 2001. He worked at Central Research Institute, Tatung Corp for 2 years as a R&D engineer in the DSP division. He received his Ph.D. in the Department of Electrical Engineering, The University of Texas at Arlington. During his Ph.D. study, he has authored and coauthored more than 20 papers in technical journals and conferences, and obtained a pending patent. His research interests include medical devices, MEMS, sensors, wireless technologies, systematic characterization methods.